WASM: Minerals, Energy and Chemical Engineering

Integration of Borehole and Surface Seismic Monitoring Techniques in CO2 Geosequestration Projects

Sofya Popik
0000-0002-8150-2541

This thesis is presented for the Degree of
Doctor of Philosophy
of
Curtin University

September 2021

Declaration

To the best of my knowledge and belief this thesis contains no material previously published by any other person except where due acknowledgment has been made.

This thesis contains no material which has been accepted for the award of any other degree or diploma in any university.

14/12/2021

Abstract

Injection of carbon dioxide (CO_2) into rock formations is currently the most feasible way of CO_2 containment in Carbon Capture and Storage (CCS) projects. A significant number of onshore and offshore CCS projects around the world have demonstrated both the potential and limitations of the 4D borehole and surface seismic method for monitoring CO_2 injections. Seismic monitoring requires the acquisition of repeated seismic surveys over the same area with a certain time gap between the consecutive surveys. Non-invasive seismic surveys are preferable because of the environmental sustainability of the storage sites and the necessity to account for the needs of all stakeholders affected by the monitoring activities of CCS projects. Thus, seismic monitoring should be tailored to reduce the footprint of the field acquisition. Relatively high acquisition and processing cost, sparseness in time, possible delay between the acquisition and availability of the interpretable data, issues with repeatability are additional limitations of seismic methods that further encourage exploring new ways for seismic monitoring campaigns.

This thesis explores the ways of integration of borehole and surface seismic techniques to improve monitoring effectiveness in CO_2 geosequestration projects. The study is based on data acquired within the CO2CRC Otway Project. The Otway research site is one of the most well-studied areas in the world due to the large number of geophysical surveys conducted as part of the various stages of CO_2 injection experiments. The Otway Project includes three main Stages. Each Stage was dedicated to a different injection scenario with an appraisal of various monitoring approaches to detect and track the evolution of injected carbon dioxide. The main objective of this thesis is to look at the different surface and downhole seismic datasets separately and find ways to integrate the analysis of data. The primary motivation of this research is to gain extra value out of the joint data analysis to optimise future monitoring concepts and to obtain additional insights about the geological setting of the Otway site. Most findings of this study can be also applicable to other CCS projects and may be applied to improve the efficacy of seismic monitoring strategies.

In the first portion of this thesis, I process and analyse all the surface seismic data acquired during Stage 2C of the Project (this includes one baseline and five

consequent monitoring surveys acquired after the injection of 5 kt, 10 kt and 15 kt of supercritical CO_2, and two more seismic surveys acquired 1- and 2-years post-injection). The findings from this part show that the high quality of the acquired seismic data together with the developed data processing strategy allow reliable surveillance of the plume topology and evolution between the surveys. The clear time-lapse seismic response provides an excellent detectability of the changes in plume shape and its lateral spreading. Analysis of the obtained images shows the absence of unwanted migration of the plume away from the zone of primary containment. Most of the lateral changes of plume evolution occurred between the baseline survey and monitor survey acquired 1 year after the final injection, which indicates plume stabilisation. The results demonstrate that the implemented monitoring approach is an effective and robust controlling strategy for carbon dioxide storage projects.

In the second step, I use the same 4D seismic data as in the first part of the study, to investigate the trade-off between the data quality and the source effort required to obtain reliable time-lapse seismic images. This study provided important results because it showed that the number of sources can be significantly reduced, while retaining the high-quality images of the plume distribution.

In the third step, I analyse the data acquired using 3D borehole vertical seismic profile (VSP) with geophones and distributed acoustic sensors (DAS) in wells. In this study, I use all the available 3D VSP data acquired at the Otway Project, which includes 3D VSP data from each of the three Stages of the Otway Project. The main source of 3D VSP data is multi-well 3D VSP acquired with DAS during Stage 3. The study of distribution of travel times with depth and offset demonstrates that both geophone and DAS data can be a good source of information for anisotropy estimation from 3D VSP surveys. The utilisation of DAS introduces a number of benefits compared to the conventional downhole sensors due to the limited coverage of conventional geophone-based VSP. Analysis of DAS data provides estimates of anisotropy parameters for the entire extent of an instrumented well. The travel time analysis shows the significant variation of direct P-wave arrival time from the isotropy model. The undertaken analysis demonstrates the presence of both azimuthal and polar anisotropy, with the simplest model to describe the medium being an orthorhombic medium.

Finally, I develop an approach to estimate the orthorhombic anisotropic velocity model. I consider two approaches of P-wave anisotropy estimation: Local and

effective. Both approaches show consistency between the results. The opportunity to estimate anisotropy parameters in five wells allowed me to analyse the variability of the anisotropy parameters in the subsurface and to build a detailed anisotropic velocity model. Anisotropic estimates show that while vertical-plane anellipticity remains almost constant for the entire depth range, azimuthal anisotropy changes significantly with depth. It varies from negligibly small in the shallow part and significantly increases below the 600 m depth, which most probably indicates the change of a stress field at this depth. The estimated azimuth of fast direction of the P-waves is about 141^0, which is consistent with the measurements of the regional stress field of the study area. This observation suggests that azimuthal P-wave velocity anisotropy at the Otway site is likely stress-induced. While the parameters estimated in different wells are consistent with each other, there are slight lateral variations in the estimated parameters, which most probably indicates variations in velocity and anisotropy fields between the wells.

Acknowledgements

First of all I would like to acknowledge my supervisory panel. I am grateful to my main supervisor Prof. Roman Pevzner for the guidance and support provided throughout my PhD. I would like to acknowledge my co-supervisor Dr. Konstantin Tertyshnikov and associate supervisors Dr. Sinem Yavuz and Dr. Stanislav Glubokovskikh for their valuable help with technical part of my PhD and with many organisational matters.

I sincerely thank Prof. Boris Gurevich and Prof. Andrej Bona for their support and advices in my PhD, for revising my articles and proofreading some chapters of the thesis.

I wish to thank other Curtin University staff members and students who helped me during my PhD in different occasions: Prof. Milovan Urosevic, Prof. Maxim Lebedev, Robert Verstandig, Murray Hehir, Lee Ignacio, Dr. Julia Correa, Dr. Dmitry Popik, Nichole Sik, Aimee Calkin.

I am sincerely thankful to my examiners for dedicating their time to read and improve my thesis.

I would like to acknowledge CO2CRC for providing financial support towards this PhD program. Funding for CO2CRC Otway Project is provided through its industry members and research partners, the Australian Government under the CCS Flagships Programme, the Victorian State Government and the Global CCS Institute. CO2CRC received financial assistance provided through Australian National Low Emissions Coal Research and Development. ANLEC R&D is supported by Low Emission Technology Australia (LETA) and the Australian Government through the Department of Industry, Science, Energy and Resources. Stage 3 of the Project was additionally funded by BHP. Landowners and the Moyne Shire community (Victoria, Australia) are also acknowledged for the support of the Project.

This research is supported by an Australian Government Research Training Program (RTP) Scholarship.

I acknowledge the software vendors for the granted access to use the following software: SeisSpace (Halliburton), Petrel (Schlumberger).

Table of contents

List of Figures

List of Tables

Abbreviations

1D	one-dimensional
2D	two-dimensional
3C	three-component
3D	three-dimensional
4D	four-dimensional; monitoring using repetitive 3D surveys
BL	baseline survey
CCS	carbon capture and storage
CDP	common depth point
CRC	collaborative research consortium
DAS	distributed acoustic sensing / sensor
EOR	enhanced oil recovery
FDU	field data recording unit
FO	fibre optic
GR	gamma-ray logging
HTI	horizontal transverse isotropy
IL	in-line
IU	interrogator unit
M[X]	monitor survey from 1 to 5
MD	measured depth
NMO	normal moveout
NRMS	normalised root mean square
OBC	ocean bottom cable
OBN	ocean bottom node
ORT	orthorhombic isotopy
PRF	pulse repetition frequency
PSDM	pre-stack depth migration
PSTM	pre-stack time migration
P-wave	pressure wave
QI	quantitative interpretation
RMS	root mean square

RMSDIF	root mean square of a difference
S/N	signal-to-noise
SOV	surface orbital vibrator
S-wave	shear-wave
TDS	total dissolved solids
TL	time-lapse
TORT	tilted orthorhombic isotropy
TS	time shifts
TTI	tilted transverse isotropy
TWTT	two-way travel time
UTM	universal transverse Mercator
VSP	vertical seismic profile
VTI	vertical transverse isotropy
XL	cross-line

Chapter 1.
Introduction

Time-lapse (TL) borehole and surface seismic methods are widely used in Carbon Capture and Storage (CCS) projects to conduct remote monitoring of the behaviour of injected CO_2 (Lumley 2010; Johnston 2013). Onshore CO_2 geosequestration sites are often located close to populated areas. As such, a common concern with the application of 4D seismic methods is gaining access to the land to conduct seismic data acquisition due to the perceived relatively high invasiveness of the method. The fact that the monitoring program requires the acquisition of repeated seismic surveys in the same area also requires special care in choosing seismic survey parameters. Similar issues may be encountered in onshore monitoring of oil and gas production. Moreover, the relatively high cost of the 4D seismic acquisition campaign and sparseness in time of the 4D seismic surveys are additional downsides of the application of the surface seismic method to monitoring projects. Nevertheless, TL seismic is still the most reliable method to track changes caused by reservoir production or CO_2 geosequestration.

Thus, it is important to explore ways of increasing the efficiency and the effectiveness of seismic monitoring campaigns. This can be achieved through the utilisation of various approaches such as the installation of permanent surface and borehole seismic receiver arrays and permanent seismic sources, as well as optimising data acquisition patterns and integrating utilisation of acquired data in conjunction with automated data processing.

This thesis explores innovative ways to integrate borehole and surface seismic monitoring techniques in CO_2 geosequestration projects. The study is based on the data acquired within the CO2CRC Otway Project.

The CO2CRC Otway Project is the first Australian pilot CCS project (Cook 2014). The project site is located onshore, approximately 240 km South-West of Melbourne. The project site appeared as a suitable place to conduct such CCS related research activities: Suitable geological settings, convenient source of natural gas (CO_2/CH_4 80%/20% mixture) from the nearby Buttress field about 1 km away, and the

depleted Naylor gas reservoir for the first stage of the injection. There are several Stages of this project, each of which was dedicated to trials of different injection scenarios, monitoring techniques and monitoring approaches. The main goal of the Otway project is to demonstrate that carbon dioxide can be safely transported, injected and monitored after being stored in geological formations. Seismic monitoring is one of the main components of the Otway Project for the assured containment of carbon dioxide.

Stage 1 of the Otway Project included the injection of 66000 tonnes of a CO_2/CH_4 gas mixture through the CRC-1 well into the Waarre Formation at a depth of 2025 m accompanied by both surface and borehole 4D seismic monitoring to track the behaviour of injected CO_2 (Urosevic et al. 2010; Cook 2014; Jenkins et al. 2012).

Stage 2C of the Otway project included injection of the CO_2-rich gas mixture into the saline aquifer at a depth of 1500 m (Paarrate Formation) accompanied by seismic monitoring of plume behaviour using time-lapse reflection seismic monitoring with a buried receiver array (Pevzner et al. 2017; Shulakova et al. 2015). The key objective of Stage 2C was to show the detectability and monitorability of a small amount of injected CO_2 (15000 tonnes). As a null result (defined as an inability to detect the injection and track propagation of the plume using 4D seismic) was considered to be the major risk to the project, dense seismic source geometries were designed and acquired. This resulted in a high-density seismic survey design. Stage 2C seismic monitoring campaign included six 3D surveys (a baseline survey and 5 monitoring surveys). Over the duration of Stage 2C, other monitoring techniques were also trialled in preparation for the next Stage 3. Those included 4D Vertical Seismic Profiling (VSP) with geophones and Distributed Acoustic Sensing (DAS) acquired concurrently with surface seismic (Correa et al. 2018; Tertyshnikov et al. 2018), continuous acquisition of data with permanently installed seismic surface orbital vibrators (SOVs), passive seismic data acquisition.

Stage 3 of the Otway Project focuses on well-based CO_2 monitoring techniques. This Stage was created to develop a borehole monitoring concept that is capable of providing reliable and continuous observations of the plume behaviour (Jenkins et al. 2021). Stage 3 also includes automation and optimisation of time-lapse borehole data acquisition and real-time onsite processing (Isaenkov et al. 2021). The main tool used in Stage 3 is multi-well VSP monitoring with the utilisation of DAS in the wells (Yurikov et al. 2021; Pevzner et al. 2021). Five wells instrumented with DAS

were used to record 4D VSP data and data acquired with a set of permanent SOV sources (Correa et al. 2021).

At the beginning of this PhD project, Stage 2C was already in progress. Thus, in this thesis, I use all the data acquired for Stage 2C. Stage 3 commenced during the progress of this thesis, as such only the first survey that was acquired as a baseline for Stage 3 is utilised in the current study.

Both 4D VSP and 4D surface seismic are widely used in the Otway Project monitoring campaign. Over the duration of the project, more than ten 3D surface and borehole seismic surveys were acquired over the area. This makes the Otway seismic data a good basis to investigate (and find the ways of reducing) the impact of the seismic surveys on the local farming community and the environment, optimise seismic data acquisition, processing and analysis.

Stages 2C and 3 are the key phases of the CO2CRC Otway Project that are analysed in the thesis. Some part of the Stage 1 data is also included in this work. Datasets used in this research include time-lapse surface seismic and VSP data.

1.1 Research motivation

As discussed above, the CO2CRC Otway Project has accumulated a large number of seismic datasets. The aim of this research project is to find ways to optimise monitor survey designs using collaborative analysis of borehole and surface seismic data. To this end, I firstly look at what can be achieved using surface seismic and VSP separately and then investigate what can be done in order to get more value out of joint data analysis to optimise the monitoring campaign.

To achieve this goal the thesis has the following objectives:

- Processing and analysis of all the Stage 2C Otway 4D surface seismic data;
- Interpretation of processed data from surface seismic, analysis of plume evolution over time;
- Optimisation of the geometry of acquisition layout from surface seismic in order to obtain high quality results with less cost and less impact on landowners;
- Analysis of travel-time field from 3D VSP surveys;

- Development of anisotropy estimation approach from 3D VSP surveys;
- Investigation of the Otway Site geological setting from the anisotropy study.

1.2 Thesis outline

The thesis is structured as follows:

The current Chapter 1 describes the aim and motivation of the study as well as the outline of the thesis and author's contribution to the work done.

Chapter 2 provides an overview of the main technologies and methods used in my thesis. First, I introduce CCS concept. Second, I provide information about seismic monitoring and the application of the surface seismic and VSP for monitoring purposes. Third, I introduce DAS as the technology that can be utilised for VSP data acquisition. Finally, I give an overview of seismic anisotropy.

In Chapter 3, I provide an overview of the Otway Project, including the principal concept of the project and a detailed explanation of each Stage of the Otway Project. Geological settings of the study area and the nature of the plume are also provided in the chapter.

In Chapter 4, I present an in-depth analysis of the 4D surface seismic data acquired with the buried receiver array for Stage 2C of the Otway Project. I describe the seismic data processing flow, present time-lapse results and analyse the evolution of the plume in the subsurface as mapped from surface seismic data. As a part of the optimisation study, I also study the effect of reducing the number of seismic sources on the detectability of the plume by applying two approaches to imitate field geometry: random and regular distribution of seismic sources.

Chapter 5 is dedicated to the analysis of 3D VSP data. In particular, it focuses on the analysis of P-wave direct arrival times on 3D VSP gathers to study the distribution of the travel times with azimuth and depth. This study leads to an estimation of P-wave anisotropic properties at the Otway site. In this chapter, I compare geophone and DAS receives for their applicability to the study of P-wave anisotropy estimation at the Otway Site. I consider two approaches of P-wave anisotropy estimation: local and effective. All the approaches are based on the P-wave

anisotropy estimation. Finally, I provide the resulting anisotropy parameters and discuss possible causes of the anisotropy at the Otway site.

Chapter 6 summarises all the work done in the thesis. In the end, I also suggest future pathways of research based on the achieved findings.

1.3 Author's contribution

All the work presented in this thesis is done by me with guidance and support of my supervisors and other Curtin University staff members. Thus, I mostly use "I" in the thesis, and when I use "we" in the thesis it indicates myself and my supervisors and/or co-authors (in case when I reuse materials from my published papers).

This thesis is a part of the CO2CRC Otway Project. My contribution to the dissertation and to the CO2CRC Otway Project can be summarised as follows:

- I took part in the seismic acquisition campaign of one of the monitoring surveys as a general observer;
- I processed and analysed all the 4D surface seismic data using commercially available software (SeisSpace, RadExPro, Petrel);
- I performed the study of the source effort on time-lapse results of surface seismic data;
- I performed extensive study of anisotropy at Otway Site based on multi-well 3D VSP data that contributed to the building of anisotropic velocity model of the Otway Site;
- I contributed to writing of number of MATLAB codes for anisotropy estimation study and for other data analyses used in this thesis;
- I published two full papers in a peer-reviewed journals as a first author and a number of abstracts submitted to various national and international conferences. I have also co-authored a number of publications and abstracts.

I have obtained permission from the copyright owners to use any of my own published work (e.g. journal articles) in which the copyright is held by another party (e.g. publisher, co-author).

The Appendix A shows Attribution of Authorship that describes my role and the role of each co-author to the publication. I reuse those papers in the thesis.

The Appendix B indicates permissions granted to reuse materials of papers and conference abstracts in the thesis.

Chapter 2.
Background

This chapter provides a literature overview of the main technologies and principles that are relevant to the Otway Site and carbon storage. Specifically, I describe carbon capture and storage (CCS) and provide an overview of major industrial and experimental CCS projects. I then introduce seismic methods and application of surface seismic, vertical seismic profiling (VSP) and distributed acoustic sensing (DAS) for the purpose of seismic monitoring. Finally, I provide an overview of seismic P-wave velocity anisotropy.

2.1 Carbon Capture and Storage

The increase of the concentration of carbon dioxide (CO_2) in the atmosphere due to industrial development is a major cause of anthropogenic climate change. One of the solutions to prevent CO_2 from being released into the atmosphere is to store it underground (Ringrose 2020). Prof. Sally Benson stated: "Pioneering projects initiated in the 1990s demonstrated that carbon dioxide capture and storage could be safe and effective at an industrial scale" (Cook 2014, xi).

CCS consists of the following main stages:

1) Capture

   To store CO_2 underground, it needs to be first captured where it is emitted. To this end, a capturing plant attached to an emitting facility, captures CO_2 before it has been released into the atmosphere, cools it down and compresses it to be transported in a dense supercritical state.

   The main application of CO_2 capture is at stationary sources, such as power plants and large industries. These include fossil fuel power plants, fuel processing plants, industrial plants related mostly to the manufacture of steel, iron, cement and bulk chemicals. CO_2 capture is more appropriate at large point sources (those emitting more than 1 $MtCO_2$ per year) than at disperse small emission sources, even though the number of small sources

is significantly bigger, large sources contribute to about 85% of total CO_2 emissions.

2) Transport

After being captured, CO_2 is transported via pipelines or ships to the storage site.

3) Storage

Secure geological formation can be used as a potential place for CO_2 storage. In order to investigate the storing potential of the reservoir it is required to carefully study the geological setting of the area, properties of storing reservoir rocks and seals. Effective storage reservoir has a good porosity and permeability, is located in a stable geological environment, and is located at a depth below 800 m so that the stored CO_2 remains in a dense supercritical state (Figure 2-1). The most typical geological storage options are at depleted oil and gas reservoirs and at deep saline aquifers. CO_2 can be used as a replacement gas for enhanced oil recovery (EOR) or it can be injected for a dedicated geological storage. Geologically stored CO_2 imitates scenario of naturally stored hydrocarbons.

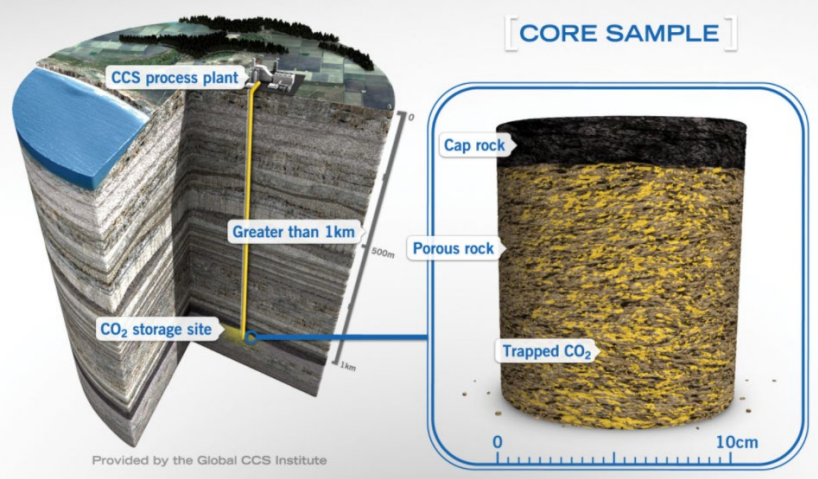

Figure 2-1 Geological storage of CO_2. Reproduced from Global CCS Institute (2020).

2.1.1 Worldwide CCS Projects

According to the Global CCS Institute's 2020 Annual report (Global CCS Institute 2020), there are 65 commercial CCS facilities (Figure 2-2): 26 in operation, 3 under construction, 13 in development and 21 in early development stages, 2 were

suspended. There are another 34 operating/developing pilot and demonstration-scale CCS facilities all over the globe.

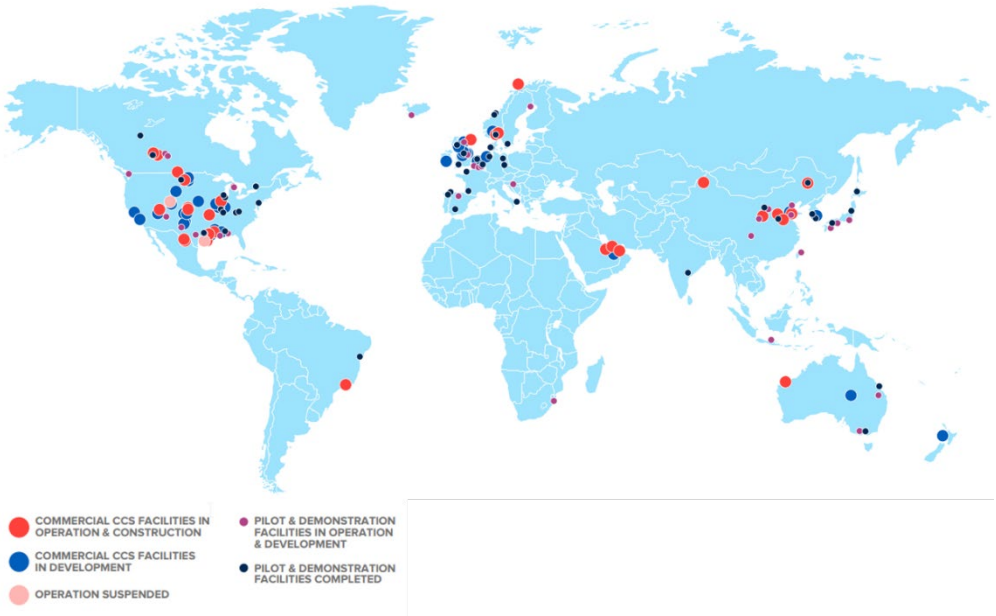

Figure 2-2 World map of CCS facilities at various stages of development according to the 2020 annual report of Global CCS Institute. Reproduced from Global CCS Institute (2020).

CCS operations are classified as large-scale when injecting over 800 kt per year of captured CO_2 from coal-based power plants, or when injecting over 400 kt per year from other intensive industry activities, such as gas power plants, fertilisers, and chemicals industry. Small-scale CCS projects involve smaller injections and are created for the purpose of testing of the design and application of certain techniques of capturing, storing and monitoring of CO_2. The findings from small-scale CCS projects are then applied to the large industry-scale projects (Jenkins, Chadwick, and Hovorka 2015).

Dedicated geological storage is conducted in such industrial-scale projects as Sleipner (Ringrose 2018), Snøhvit (Hansen et al. 2013), In Salah (Ringrose et al. 2013; Eiken et al. 2011), Quest (Rock et al. 2017), Gorgon (Flett et al. 2009) among others; in demonstration and pilot-scale research projects Decatur (Finley 2014), Aquistore (Worth et al. 2014), Frio (Hovorka et al. 2006), Nagaoka (Kikuta et al. 2005), Otway (Cook 2014; Jenkins et al. 2017; Pevzner et al. 2017) and Ketzin (Martens et al. 2012) among others.

EOR CCS projects at industrial scale include Weyburn (Hitchon 2012), Petrobras Santos Basin Pre-Salt Oil Field (Godoi and dos Santos Matai 2021), Boundary Dam (Worth et al. 2014) and Cranfield (Hovorka, Meckel, and Treviño 2013) among others.

2.2 Seismic monitoring

All CCS projects require a reliable strategy to monitor evolution of the injection and verify stabilisation of the injected CO_2 into a deep subsurface. Active surface seismic monitoring is a well-established tool for remote seismic monitoring in oil and gas industry and also very promising in CCS industry due to its ability to track fluid saturation and pressure changes in space and time (Jenkins, Chadwick, and Hovorka 2015). Time-lapse 3D seismic has good temporal and spatial resolution and ability to cover extended areas. With optimal survey parameters, multi-trace 3D coverage provides significant signal-to-noise (S/N) ratio and make this method suitable for tracking volumetric changes in the reservoir.

2.2.1 Seismic monitoring concept

Seismic monitoring (or time-lapse seismic) consists of a seismic survey acquired before the start of CO_2 injection (baseline (BL)) followed by one or more repeat seismic surveys (monitor (M)) taken in the same geographic location at different time after the start of the CO_2 injection. In the case of repeat 3D seismic surveys, the method is also known as the 4D seismic monitoring method. The fourth dimension (4D) represents the time (Landro and Bjørlykke 2010; Johnston 2013; Lumley 2001).

Time-lapse seismic method evaluates changes in the subsurface occurring in the target reservoir. These changes can be associated with the production of the oil and gas field or with the injection of the CO_2 and its storage in the subsurface. The concept of 4D seismic is shown on Figure 2-3 on the example of a swept reservoir. Amplitudes and travel-time variations caused by the change in the reservoir properties are detected between the surveys.

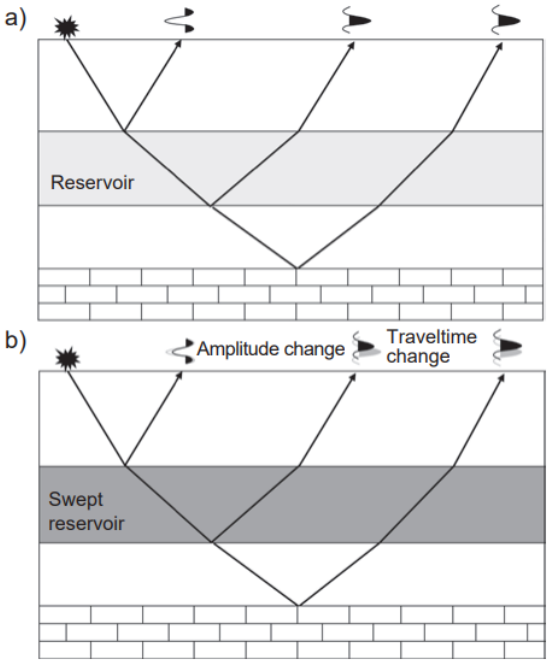

Figure 2-3 A simple concept of 4D surface seismic. a - baseline survey. b - monitor survey acquired after a change at a reservoir level. Reproduced from Johnston (2013).

Quality of the time-lapse seismic can be quantified by its *repeatability* – a measure of similarity between two surveys acquired at a different time over the unchanged subsurface. Repeatability is usually assessed by comparing seismic data sets over geologic intervals away from changes expected from injection. In an ideal situation, changes between the monitor and a baseline surveys should occur only due to a production or injection at a reservoir level. However, there are number of factors that can degrade seismic repeatability: seismic acquisition geometry, differences in the processing workflows, changes in near-surface conditions, and noise. In most cases, the changes of the seismic section caused by injection are relatively small. Hence, every effort must be undertaken to minimise the effect of all these factors in a 4D campaign at the data acquisition and processing stages.

Another important time-lapse seismic aspect is *detectability* which is the measure of the changes in the physical properties that can be detected using seismic methods. High level of both repeatability and detectability leads to a high chance of the 4D project success with respect to accurate monitoring and accounting of injected CO_2.

The main methods used for seismic monitoring are surface seismic and Vertical Seismic Profiling (VSP). A number of onshore and offshore CCS projects around the

world have used the time-lapse seismic methods for monitoring CO_2 injections. In particular, the Ketzin onshore project in Germany (Ivanova et al. 2012; Ivandic et al. 2015; Huang et al. 2018; Lüth et al. 2011) has demonstrated successful detection of the injected CO_2 gas and evolution of the plume through repeated surveys using 4D seismic monitoring. The Sleipner CCS project (Chadwick et al. 2009) in the Central North Sea offshore Norway has revealed a great potential of 3D and 4D seismic methods for CO_2 detection, monitoring and accounting. The Sleipner project has greatly contributed to providing the guidelines for future large CCS projects. It has shown that every sequestration case is unique and a monitoring strategy should be case-specific and risk-based as well as flexible, especially considering the long-term nature of CCS projects (Furre et al. 2017). The Snøhvit offshore CCS project in the Barents Sea of Norway has also successfully implemented time-lapse 3D seismic for the purpose of monitoring of the CO_2 plume distribution (Jenkins, Chadwick, and Hovorka 2015). The comprehensive seismic monitoring campaign has been utilised in the Weyburn EOR CCS project including 4D seismic with multicomponent receivers (White 2011). The Frio Pilot USA project successfully used time-lapse VSP and crosswell seismic to detect and image as small amount as 1.6 kt of injected CO_2 (Daley et al. 2008). The Australian Pilot Otway Project has successfully used 4D surface seismic with permanently installed buried receiver array and 4D VSP monitoring techniques to detect and monitor evolution of a small plume (5-15 kt) (Pevzner et al. 2017; Popik, Pevzner, Tertyshnikov, et al. 2020; Correa et al. 2018).

Next two subsections provide information about surface seismic and VSP methods, respectively, giving overview of the main advantages and limitations for subsurface monitoring.

2.2.2 Surface seismic

Surface seismic can be used in both land and marine environment. The following information is mostly focusing on land surface seismic method because the data used in this thesis was acquired onshore.

In the land surface seismic method, both sources and receivers are located on the earth surface. Seismic source generates seismic signal that propagates through the earth, gets reflected from different boundaries created by the difference in acoustic impedance, and is then detected using seismic receivers. Different waves are generated

and recorded during seismic acquisition campaign including direct wave, reflected waves (P-waves and S-waves), converted waves, refracted waves, surface waves, etc. Reflected waves are the most valuable signal in oil and gas and CCS industries. In surface seismic, these waves have two-way ray path (Figure 2-4).

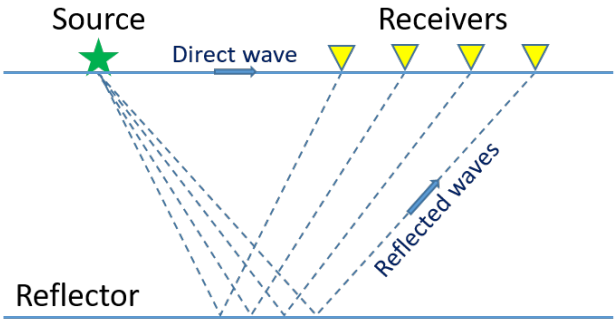

Figure 2-4 Schematic of the surface seismic principle.

The most feasible for oil and gas and CCS industries seismic source for land application is vibroseis due to its ability to emit strong signals that reach significant depths and due to its relatively mild impact on the environment compared to explosive sources. In land seismic acquisition, most commonly used receivers are geophones.

Marine seismic data are usually acquired utilising vessel equipped with towed air guns as sources and towed sets of hydrophones forming streamer cables as receivers. Alternatively, marine seismic receivers can be located on the sea bottom (ocean bottom cables (OBC) or ocean bottom nodes (OBN)) and include both geophones and hydrophones.

Seismic acquisition can be 2D or 3D. In 2D acquisition, the seismic sources and receivers are located along the same straight line, and the result of this survey is a vertical cross-section of the subsurface beneath that line. Typically, 2D seismic surveys are used primarily in unexplored areas for regional mapping and for initial exploration to gain a basic understanding of the geology of the study area. Often, several parallel 2D seismic lines are acquired for these purposes. The main limitation of 2D seismic is its inability to correctly image steeply dipping structures that are not in the vertical plane beneath the 2D line. To solve the problem of interpretation of off-line objects, the 3D seismic survey is required (Onajite 2014).

3D seismic surveys are used for more detailed characterisation of the area. In 3D acquisition, seismic receivers are spread out over an area. Seismic source is moved from one location to another location on the surface. 3D surface seismic provides a

larger area of coverage and also improves data density compare to 2D. The main result of a 3D survey is a 3D seismic reflection or attribute data cube which represents positions and reflectivities of various geologic structures. 3D seismic data provide detail and correct information about fault distribution (unlike 2D, which assumes vertical rays which is inaccurate for real 3D structures). Acquisition of 3D seismic surveys is often much more expensive and time-consuming than 2D and thus such surveys are often acquired after initial 2D acquisition.

2.2.3 Vertical seismic profiling (VSP)

The vertical seismic profile (VSP) method is different from surface seismic in that receivers are located in a borehole, while seismic sources are still located on the surface (Galperin 1985). Figure 2-5 shows schematic of a VSP data acquisition. VSP surveys can use the same sources as used in surface acquisition. Conventional VSP surveys are acquired with 3-component (3C) geophone receivers.

Typical VSP geometries include offset VSP, walkaway VSP and 3D VSP surveys. Offset VSP survey is a type of the survey that includes only one shot position on the surface. It may be very close to (zero-offset), near (near-offset) and far from the wellhead (far-offset). Zero-offset VSP is normally used for well-tie in order to tie well information to the surface seismic information. A walkaway VSP survey is analogous to a 2D surface seismic survey: sources are located along a horizontal 2D line (normally passing close to the wellhead) and provide a 2D section of the subsurface. 3D VSP data acquisition provides characterisation of a 3D subsurface volume near the well path. Acquisition of a 3D surface seismic survey and a 3D VSP seismic survey can be combined by recording the same source excitations with receivers installed simultaneously at surface and in the wells. This can significantly optimise seismic data acquisition process.

A typical VSP survey includes a VSP tool containing one or several receivers (with adjustable 3C geophone vertical spacing of 5 to 20 m) installed in a well. The VSP tool typically does not cover the whole well section with measurements because it is operationally challenging due to significant weight of the tool and also due to high cost of such installations. Most of the tools contain up to 24 geophones. However, there are VSP tools that can have even 120 levels (Valishin 2018) and thus cover significant portion of the well. Alternative approach to obtain the whole well coverage

with geophone tool containing only a few levels is to relocate the tool to another depth levels and repeat source excitations. The necessity to reinstall and reshoot VSP surveys with a downhole geophone array tool make this method expensive for walkaway and 3D VSP surveys. However, for zero-offset and offset VSPs the practice of acquiring data over the length of the well is quite common (Galperin 1985). Utilising distributed acoustic sensing (DAS) in wells allows to overcome the issue of acquiring 3D and walkaway VSP surveys compare to geophones due to ability to cover the whole well with DAS receivers with one source excitation. Detailed information about DAS and its use in VSP data acquisition is described in the Section 2.3.

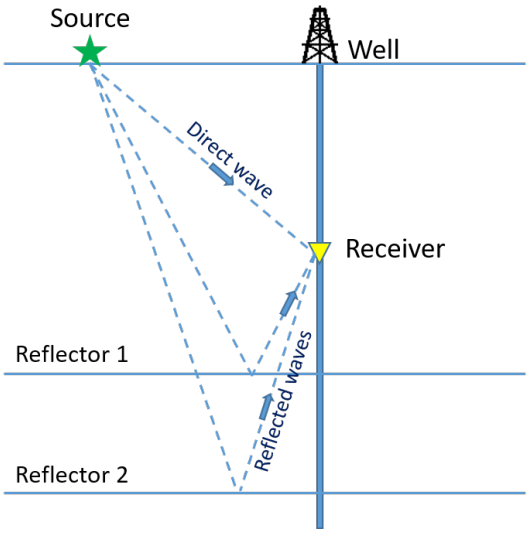

Figure 2-5 Schematic of the VSP principle.

Compared to surface seismic, VSP illuminates only a relatively small near-well area and thus has a limited illumination zone. Despite this, VSP has a number of advantages. First of all, VSP data has better S/N ratio due to lack of the surface related noise and lower levels of ambient noise. In addition, in VSP geometry, the waves propagate only once though the near-surface area, and thus are less distorted compared to two-way propagation is the surface seismic geometry. Also, shorter ray paths of reflected waves lead to smaller attenuation of high-frequency components. Thus, VSP data have a broader spectrum than surface seismic data and, thus may provide better resolution (O'Brien, Kilbride, and Lim 2004). Finally, VSP method provides an exact relationship between time and depth dimensions because the depth position of each receiver in the well is known precisely. However, compared to surface seismic surveys, walkaway and 3D VSP suffer from limited areal coverage in the vicinity of the well location, and low and uneven seismic fold.

2.3 Distributed Acoustic Sensing

Distributed acoustic sensing (DAS) is an emerging technology used increasingly in seismic data acquisition (Parker, Shatalin, and Farhadiroushan 2014). The seismic application of fibre-optic (FO) cables in wells began in the early 2000s when fibre point sensors were used to record the response of seismic excitations in the well (Bostick 2000). Mestayer et al. (2012) demonstrated the first application of DAS for the VSP data acquisition. Since then DAS technology has been significantly advanced and improved for the purpose of seismic data acquisition in a variety of field situations.

DAS uses a FO cable connected on one end to the interrogator unit (IU). Interrogator sends a series of laser pulses through the fibre and then detects the backscattered signal (Figure 2-6). Detected signal results from Rayleigh back-scattering which originates from the imperfections that naturally occur in any optical fibre during manufacture process. As the velocity of light in the fibre glass is constant (~$2x10^8$ m/s), knowing the time of the back-scattered signal, we can identify the position of the backscatter points along the fibre-optic cable.

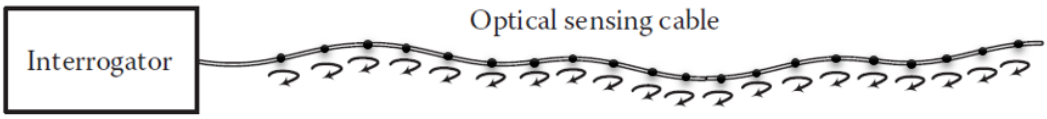

Figure 2-6 Schematic of a DAS system. Reproduced from Hartog (2017). Black dots schematically represent the position of the internal DAS backscattering points (they can be regular or random depending on the type of cable used for DAS acquisition).

The three main DAS acquisition parameters that contribute to the signal-to-noise (S/N) ratio and resolution of the signal are:

1) Pulse length – duration of the emitted light (typically ~ 1 m) which controls the vertical resolution;
2) gauge length – distance between two points of the fibre used for computation of phase difference (typical ranges are between 7 and 35 m – smaller than the typical seismic wavelength). This parameter mainly contributes to the S/N ratio (Dean, Cuny, and Hartog 2017) – larger values provide higher S/N seismic data but can also distort high frequency content and affect spatial resolution;

3) pulse repetition frequency (PRF) – this parameter depends on the length of the fibre, so only one pulse should be emitted for the duration of its travelling along the fibre in order to be able to separate backscattered events. Thus, the frequency content of resulting data depends on the optical path length (which is related to the cable length). For a 1 km long optical fibre, PRF can be close to 100 kHz, for a 10 km fibre – to 10 kHz.

Most of the DAS systems are based on phase measurements. Phase-based systems detect differences in phase between backscattering centres. The acoustic signal originated from the seismic source stretches or compresses the fibre and causes a corresponding change of backscattered light. Such change results in a change in the phase difference between two backscattering points over which the signal is measured. This change over time corresponds to the difference of a strain rate of the fibre. Strain rate data can be converted into a particle velocity and thus carry information equivalent to the conventional geophone seismic data (Bakku 2015; Bona et al. 2017).

Recent development in the design of fibre-optic cables and interrogators has brought more opportunities to the DAS application for seismic applications. In particular, recently developed engineered fibre produces much better S/N ratio and control over the amplitude and phase of the data compared to standard fibre. The location of scattering points (fibre imperfections) in standard fibre is randomly spread along the cable, which leads to distortions in amplitude and phase of the backscattered signal and consequently to reduced S/N ratio (Glubokovskikh et al. 2021). The engineered fibre is manufactured with purposely created regular bright scatter centres along its length to produce and capture more of the backscattered light back to the interrogator (Naldrett 2021; Richter et al. 2019).

DAS has proved to be promising for various applications in seismic industry including, but not limited to, downhole seismic surveys (VSP), active surface seismic, as well as earthquake and micro-earthquake detection. However, DAS has one strong limitation: since it measures strain rate along the fibre, its sensitivity decreases strongly with increasing angle between the fibre and wave polarisation and is zero for P-waves propagating perpendicular to the fibre. Thus, using DAS in surface seismic surveys is challenging as it is relatively insensitive to deep reflections, which tend to arrive at the surface in near-vertical directions (due to low near-surface velocities). Conversely, DAS is particularly useful for downhole measurements due to its strong sensitivity to the waves polarised along the cable.

Acquisition of DAS VSP has a number of advantages compared to conventional geophone VSP. DAS can be installed in the well permanently and the fibre optic (FO) cable can cover the entire length of the well. Figure 2-7 demonstrates schematic of the utilisation of DAS in the well and compares it to the geophone tool for the VSP acquisition and shows basic principles of DAS acquisition. The entire well coverage and the ability to permanently install FO cable in the well are particularly attractive for seismic time-lapse monitoring – cables can be utilised as required at any time by simply connecting them to the interrogator unit (IU). Another advantage of DAS is spatial sampling because of the distributed nature of the receiver: Data can be acquired along FO with spacing as small as 25 cm (Naldrett, Cerrahoglu, and Mahue 2018). Also, the frequency bandwidth of DAS receivers is usually much wider than the normal geophone seismic range.

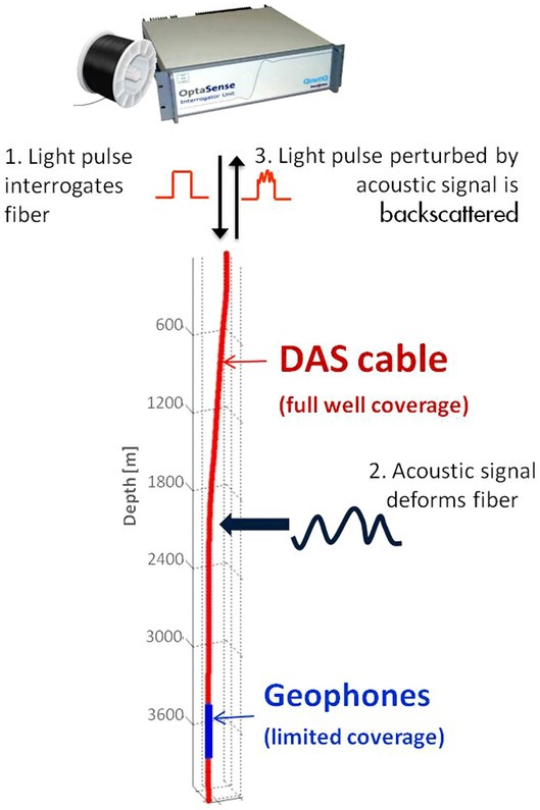

Figure 2-7 Schematic of the utilisation of DAS in the well. Reproduced from Mateeva et al. (2014).

There are a few limitations of DAS that reduces its S/N ratio compared to a traditional geophone instrumented VSP. In particular, the ability to acquire 3C VSP data with geophones makes geophones superior in recording the full wavefield. As DAS measures strain along the cable, the DAS cable is a 1-component receiver. In

addition, DAS directivity pattern is different from that of a vertical geophone. DAS sensitivity to plane P-waves decays as the squared cosine of the incidence angle between the directions of the fibre and wave propagation (Kuvshinov 2016) while the sensitivity of a vertical geophone decays as a cosine of the incidence angle.

There are different approaches to installation of a fibre-optic cable in a well. FO cables can be installed inside the tubing, outside the tubing or cemented behind the casing of the well. The latter option produces the best S/N ratio, however, it cannot be implemented in every well due to the well design and other limitations.

The most critical part in DAS design is installation of the FO cables in wells, which may require more complicated well design. However, a DAS cable can cover the entire length of the well, unlike a geophone string, which can typically cover 100-200 m only. This has several advantages. First, DAS VSP surveys can take far less time than with geophones, as the entire zero-offset or single-offset DAS VSP can be done with one shot, whereas for geophones, each location of the geophone string requires a separate shot. Even greater advantages are with walk-away and 3D VSP, where use of DAS gives much better coverage than a corresponding survey with a geophone string. Second, if a DAS cable is installed behind the casing, it is fixed for many years, and is ideal for time-lapse monitoring. Third, FO cable is significantly cheaper than the geophone tool. Fourth, there are cases where geophones cannot be installed in the wells (in case of risk of well intervention, prohibitively high cost of geophone data acquisition, risk to lose the geophone tool in the wells, deviated well data acquisition, etc.); in those cases, DAS VSP often becomes the only feasible and non-intrusive option for permanent monitoring.

As discussed above, the main utilisation of DAS is for VSP seismic data acquisition. VSP seismic monitoring is used for the monitoring of oil recovery and in CCS industry to monitor changes in the subsurface caused by the injection of carbon dioxide. Examples of successful utilisation of DAS with various VSP geometries for monitoring projects was demonstrated in Mateeva et al. (2017), Daley et al. (2013); Cox et al. (2012), and Hance et al. (2016) among others.

2.4 Seismic anisotropy

Variation of seismic velocities with respect to the wave propagation direction is known as seismic velocity anisotropy. Since travel times of seismic waves that propagate through an anisotropic medium can vary significantly from those that travel through isotropic media (Tsvankin 2012; Thomsen 2002; Helbig 1994), it is important accurately determine velocity anisotropy and incorporate it in data processing to avoid mispositioning of reflectors and distortion of amplitudes (Castagna and Backus 1993). This is especially crucial for seismic data acquired over wide offset and azimuth ranges. In addition, measurement of the effects of velocity anisotropy in seismic data can provide useful information about subsurface properties such as depositional and stress history (Sayers 2010), as anisotropy is influenced by these factors.

In real geological settings, anisotropy can be very varied and complex. In general, it can be represented as polar or azimuthal, or a combination of both types. Polar anisotropy, where the velocities change with the polar angle (angle between the propagation direction and the vertical axis), is ubiquitous in the sedimentary crust and is usually caused by the anisotropic rock microstructure (most commonly in shales) or thin layering, which are, in turn, related to the fact that deposition is controlled by the vertical gravity field (Johnston and Christensen 1995; Leaney 2008; Sayers 2005). Media with pure polar anisotropy have a vertical symmetry axis, are isotropic in the horizontal plane and thus are known as vertically transversely isotropic (VTI) media (Figure 2-8a). Azimuthal anisotropy represents directional dependence of velocities in the horizontal plane and is usually caused by aligned fractures and/or azimuthal anisotropy of the stress field (Sayers 2002; Mavko, Mukerji, and Godfrey 1995; Gavin and Lumley 2016; Bakulin, Grechka, and Tsvankin 2000; Gurevich, Pervukhina, and Makarynska 2011). The simplest medium with azimuthal anisotropy has a horizontal symmetry axis and is known as horizontally transversely isotropic (HTI). Furthermore, the simplest medium with both polar and azimuthal anisotropy is an orthorhombic (ORT) medium (Figure 2-8c) (Tsvankin 1997). In some geological cases the medium has an axis of symmetry but it is neither horizontal nor vertical, in such a case it is called "tilted". An example of tilted transversely isotropic medium (TTI) is shown in Figure 2-8b, an example of tilted orthorhombic medium (TORT) is shown in Figure 2-8d.

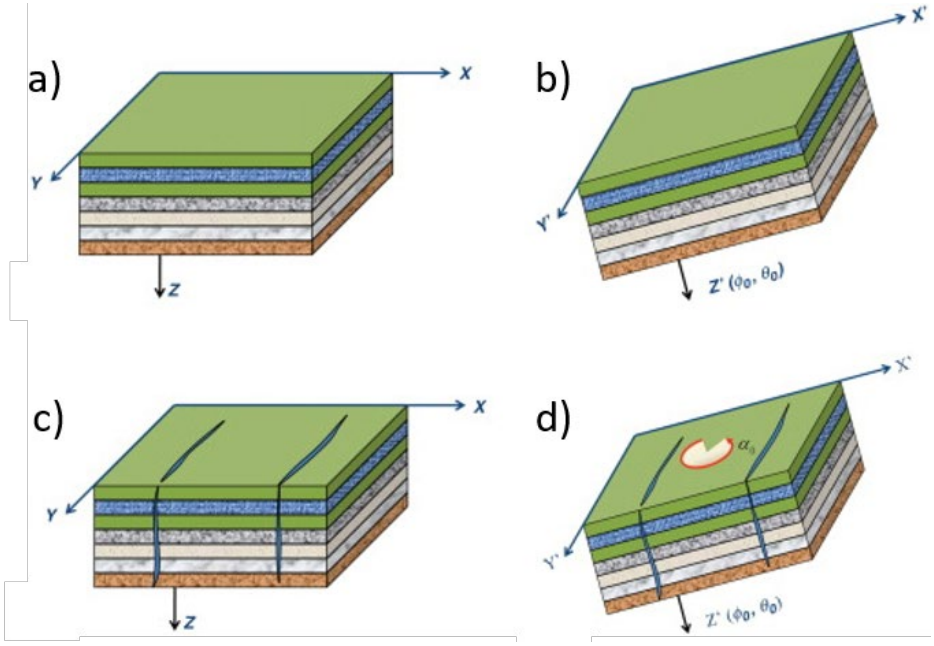

Figure 2-8 Geological models for typical types of anisotropy. a – VTI media; b – TTI media; c – orthorhombic media (ORT); d – tilted orthorhombic media (TORT). Reproduced from Zhang (2015).

The Einstein convention (Einstein 1916) is the most common convention used to write equations in elasticity theory. It states that every index variable that is repeated once in a single term implies a summation of that term over all the index variables ranging from 1 to n in n-dimensional problem.

The properties of anisotropic linearly elastic materials, are described by a generalised Hooke's law, which is a linear relationship between each component of stress and each component of strain:

$$\sigma_{ij} = C_{ijkl}\varepsilon_{kl} \qquad i,j,k,l = 1,2,3 \qquad (1)$$

where σ_{ij} is the stress tensor, ε_{kl} the strain tensor, and C_{ijkl} the stiffness (or elasticity) tensor.

Although the general fourth-order tensor has 81 independent components, the stiffness tensor C_{ijkl} possesses several symmetries that reduce the number of independent elements. The symmetries of the stress and strain tensors allow to interchange the indices *i* with *j*, and *k* with *l*:

$$C_{ijkl} = C_{jikl} = C_{ijlk} \qquad i,j,k,l = 1,2,3\,. \qquad (2)$$

Also, due to thermodynamic considerations (Aki and Richards 2002; Helbig 1994):

$$C_{ijkl} = C_{klij} \qquad i,j,k,l = 1,2,3\,. \qquad (3)$$

Due to the symmetry of the stiffness tensor (equations 2 and 3), the medium with the lowest possible symmetry is defined using total 21 independent stiffness coefficients. Thus, the general stiffness tensor has the following 6x6 matrix form:

$$\{C_{ijkl}\} = \begin{pmatrix} C_{1111} & C_{1122} & C_{1133} & C_{1123} & C_{1113} & C_{1112} \\ C_{1122} & C_{2222} & C_{2233} & C_{2223} & C_{2213} & C_{2212} \\ C_{1133} & C_{2233} & C_{3333} & C_{3323} & C_{3313} & C_{3312} \\ C_{1123} & C_{2223} & C_{3323} & C_{2323} & C_{2313} & C_{2312} \\ C_{1113} & C_{2213} & C_{3313} & C_{2313} & C_{2323} & C_{1312} \\ C_{1112} & C_{2212} & C_{3312} & C_{2312} & C_{1312} & C_{1212} \end{pmatrix}. \quad (4)$$

By implementing Voigt's notation using the following law (Helbig 1994) the stiffness tensor can be further simplified:

ij => α; kl => β:

11 => 1; 22 => 2; 33 => 3; 23 = 32 => 4; 13 = 31 => 5; 12 = 21 => 6.

Thus, the stiffness tensor $\{C_{ijkl}\}$ can be represented as the following stiffness matrix $\{C_{\alpha\beta}\}$:

$$\{C_{\alpha\beta}\} = \begin{pmatrix} C_{11} & C_{12} & C_{13} & C_{14} & C_{15} & C_{16} \\ C_{12} & C_{22} & C_{23} & C_{24} & C_{25} & C_{26} \\ C_{13} & C_{23} & C_{33} & C_{34} & C_{35} & C_{36} \\ C_{14} & C_{24} & C_{34} & C_{44} & C_{45} & C_{46} \\ C_{15} & C_{25} & C_{35} & C_{45} & C_{55} & C_{56} \\ C_{16} & C_{26} & C_{36} & C_{46} & C_{56} & C_{66} \end{pmatrix}. \quad (5)$$

The structure of the stiffness matrix depends on the class of symmetry of the media. In media with no symmetry plane (triclinic media) the stiffness matrix has 21 independent constants (equation 5). Additional symmetry planes simplify the stiffness matrix. For isotropic media, the stiffness matrix contains only two independent parameters. In the simplest transverly isotropic case (VTI or HTI) the stiffness matrix contains five independent constants.

The VTI stiffness matrix is given by

$$\{C_{\alpha\beta}\} = \begin{pmatrix} C_{11} & C_{11}-2C_{66} & C_{13} & 0 & 0 & 0 \\ C_{11}-2C_{66} & C_{11} & C_{13} & 0 & 0 & 0 \\ C_{13} & C_{13} & C_{33} & 0 & 0 & 0 \\ 0 & 0 & 0 & C_{55} & 0 & 0 \\ 0 & 0 & 0 & 0 & C_{55} & 0 \\ 0 & 0 & 0 & 0 & 0 & C_{66} \end{pmatrix}. \quad (6)$$

The stiffness matrix of orthorhombic media consists of nine independent coefficients and is given by

$$\{C_{\alpha\beta}\} = \begin{pmatrix} C_{11} & C_{12} & C_{13} & 0 & 0 & 0 \\ C_{12} & C_{22} & C_{23} & 0 & 0 & 0 \\ C_{13} & C_{23} & C_{33} & 0 & 0 & 0 \\ 0 & 0 & 0 & C_{44} & 0 & 0 \\ 0 & 0 & 0 & 0 & C_{55} & 0 \\ 0 & 0 & 0 & 0 & 0 & C_{66} \end{pmatrix}. \quad (7)$$

Stiffness coefficients are not convenient for seismic processing and inversion. Thomsen (1986) introduced an alternative notation for transverse isotropic (TI) media. He suggested describing such a media by the symmetry-directional velocities of P- and S-waves (V_{P_0} and V_{S_0}, respectively) and three dimensionless parameters (ε, δ and γ) describing the magnitude of anisotropy (Tsvankin et al. 2010). Such notation captures the combinations of stiffness coefficients constrained by seismic signatures, which makes it more suitable for use in seismic processing and imaging. Parameter ε defines so-called "P-wave anisotropy" and represents difference between the P-wave velocities in the horizontal and vertical directions. Likewise, parameter γ represents "SH-wave anisotropy". Parameter δ determines the second derivative of the P-wave phase-velocity with respect to the polar angle at vertical incidence, it is responsible for the angular dependence of P-wave in the vicinity of the vertical symmetry direction and also influences the SV-wave velocity (Tsvankin et al. 2010).

Thomsen parameters are related to the stiffness coefficients as follows:

$$V_{P_0} = \sqrt{\frac{C_{33}}{\rho}} \quad (8)$$

$$V_{S_0} = \sqrt{\frac{C_{55}}{\rho}} \quad (9)$$

$$\varepsilon = \frac{C_{11} - C_{33}}{2C_{33}} \quad (10)$$

$$\delta = \frac{(C_{13} + C_{55})^2 - (C_{33} - C_{55})^2}{2C_{33}(C_{33} - C_{55})} \quad (11)$$

$$\gamma = \frac{C_{66} - C_{55}}{2C_{55}} \quad (12)$$

Tsvankin (2012) extended Thomsen's notation to orthorhombic media. In ORT media there are two orthogonal horizontal symmetry axes, namely x_1 and x_2, and a vertical symmetry axis x_3. The set of equations 13-21 represents these ORT anisotropy parameters. The superscript shows the plane normal to the symmetry axis (i.e. the superscript (1) refers to x_1 axis, which is orthogonal to the $[x_2, x_3]$ plane):

$$V_{P_0} = \sqrt{\frac{C_{33}}{\rho}} \tag{13}$$

$$V_{S_0} = \sqrt{\frac{C_{55}}{\rho}} \tag{14}$$

$$\varepsilon^{(1)} = \frac{C_{22} - C_{33}}{2C_{33}} \tag{15}$$

$$\delta^{(1)} = \frac{(C_{23} + C_{44})^2 - (C_{33} - C_{44})^2}{2C_{33}(C_{33} - C_{44})} \tag{16}$$

$$\gamma^{(1)} = \frac{C_{66} - C_{55}}{2C_{55}} \tag{17}$$

$$\varepsilon^{(2)} = \frac{C_{11} - C_{33}}{2C_{33}} \tag{18}$$

$$\delta^{(2)} = \frac{(C_{13} + C_{55})^2 - (C_{33} - C_{55})^2}{2C_{33}(C_{33} - C_{55})} \tag{19}$$

$$\gamma^{(2)} = \frac{C_{66} - C_{44}}{2C_{44}} \tag{20}$$

$$\delta^{(3)} = \frac{(C_{12} + C_{66})^2 - (C_{11} - C_{66})^2}{2C_{11}(C_{11} - C_{66})} \tag{21}$$

where V_{P_0} is the vertical P-wave velocity; V_{S_0} is the velocity of the S-wave polarised in the x_1 direction; $\varepsilon^{(1)}$ and $\varepsilon^{(2)}$ are the VTI parameters ε in the [x_2, x_3]-plane and [x_1, x_3]-plane, respectively; $\delta^{(1)}$ and $\delta^{(2)}$ are the VTI parameters δ in the [x_2, x_3]-plane and [x_1, x_3]-plane, respectively; $\gamma^{(1)}$ and $\gamma^{(2)}$ are the VTI parameters γ in the [x_2, x_3]-plane and [x_1, x_3]-plane, respectively; $\delta^{(3)}$ is the VTI parameter δ in the [x_1, x_2]-plane. Thus, P-wave anisotropy depends on the V_{P_0} and five anisotropy coefficients ($\varepsilon^{(1)}$, $\delta^{(1)}$, $\varepsilon^{(2)}, \delta^{(2)},$ and $\delta^{(3)}$). The parameters $V_{S_0}, \gamma^{(1)}$ and $\gamma^{(2)}$ are responsible for S-wave kinematics.

There are several ways to estimate the anisotropy parameters from seismic data (Tsvankin et al. 2010). The choice of an anisotropy estimation approach depends on a number of factors, such as symmetry, degree of anisotropy (approximation of the medium), availability of certain seismic data for anisotropy estimation and the intended use of the estimated anisotropy parameters.

Anisotropy parameters can be separated in two general groups: Effective and local. Effective anisotropy parameters are obtained by fitting of the multiple parameters (number of parameters depends on the type of symmetry) into the travel-time curves. Resulting parameters are called “effective” as they represent the whole

area of the ray path). For reflection seismic data, the most common approach for effective P-wave anisotropy parameters estimation is nonhyperbolic velocity analysis. Tsvankin and Thomsen (1994), Alkhalifah and Tsvankin (1995), Grechka and Tsvankin (1998) and many others provide the application of the nonhyperbolic P-wave velocity analysis for TI media. Grechka et al. (2001) describe a similar method for TTI media. Grechka and Tsvankin (1999) extend this approach to ORT media. There are other methods of effective anisotropy parameter estimation. Some of these methods include analysis of both P- and S-waves. For example, Grechka et al. (2002); Grechka, Theophanis, and Tsvankin (1999), Van der Baan and Kendall (2002) developed joint analysis of P-wave and converted PS-wave data for anisotropy parameter estimation.

Local anisotropy parameters correspond to a local piece of the medium. These parameters represent local conditions and consequently can be later extrapolated into interval parameters. Estimation of local anisotropy is usually only possible in the vicinity of sources or receivers, and hence is mostly applicable to VSP data with receivers located at these fixed depth locations. Local anisotropy parameters have been estimated using different methods by several authors. In general, all methods can be divided into slowness and slowness-polarisation methods, each of the method can utilise P-waves only or also S-waves. Assuming horizontally layered earth, P-wave slowness surfaces $p^{(P)}$ can be estimated by differentiating of the P-wave traveltimes ($t^{(P)}$) of the VSP first arrivals with respect to the coordinates of the source locations and the location of the receiver in the borehole:

$$p_i^{(P)} = \frac{\partial t^{(P)}}{\partial x_i} \; (i = 1,2,3) \; . \qquad (22)$$

Vertical slowness $p_3^{(P)}$ corresponds to the depth location of the receiver, while two components of the horizontal slownesses $p_1^{(P)}$ and $p_2^{(P)}$ correspond to the source positions at the earth surface. If we assume lateral homogeneity of the media, the horizontal components of the slowness vector can be relocated to the position of the receiver according to the Snell's law and the complete slowness vector can be constructed (Gaiser 1990). Miller and Spencer (1994), Zheng and Pšenčík (2002), Jílek, Hornby, and Ray (2003), Grechka, Jorgensen, and Lopez (2006) demonstrate various approaches to local anisotropy estimation by finding the values of the parameters that produce the best fit between the modelled and observed slowness surfaces.

A combination of slowness and polarisation vectors for local anisotropy estimation can provide more stable parameter estimation in locally homogeneous media where the effect of interference of the direct waves with reflected and converted arrivals on the measured polarisations is negligible. The polarisation vector of P-wave can be obtained from 3C VSP data. Horne and Leaney (2000), Dewangan and Grechka (2003), Grechka and Mateeva (2007), Abedi, Rashidi Fard, and Riahi (2019) studies demonstrate application of slowness-polarisation methods for local anisotropy estimation.

Analysis of P-waves only is not enough to obtain all the stiffness coefficients and joint analysis of P- and S-wave is required. In VSP geometry it is possible to obtain 3-component data with 3C geophones in order to detect S-waves.

In this Chapter I presented only a general overview of the local and effective methods, without showing particular approximations and equations. For more detailed information the reader can refer to the above cited publications. The approaches used in my PhD thesis for both local and effective parameter estimation are described in detail in Chapter 5.

Chapter 3.
CO2CRC Otway Project

This chapter describes the main Stages of the CO2CRC Otway Project. In my PhD, I use datasets acquired in each of the Stages of the Project. My main research focus is on Stage 2C and Stage 3. However, 3D VSP data acquired previously during Stage 1 also added information to this PhD project. First, I provide general overview of the Otway Project. Second, I describe geology of the study area and nature of the injected gas mixture. Finally, I provide detailed information about each Stage of the Otway Project. This chapter includes information from Popik, Pevzner, Tertyshnikov, et al. (2020).

3.1 Otway Project overview

The CO2CRC Otway Project is a multi-stage onshore Australian pilot CCS initiative aiming to demonstrate the environmental and community safety of CO_2 geosequestration. Over the years, the project acquired distinct capabilities and features to become one of the leading-edge research CCS facilities.

The Otway basin was a suitable place to conduct pilot CCS project: there was natural source of CO_2-rich gas and depleted Naylor gas reservoir suitable for CO_2 geosequestration.

The Otway Site is located in the Australian State of Victoria, approximately 240 km West of the State Capital Melbourne (Figure 3-1) in an extensive cattle farming area. The fact that this area belongs to a number of different landowners and farmers significantly affected the design of the project. Every effort was exerted to acquire data with minimal disturbance to the local environmental and farming activities while maintaining the maximum possible efficiency and quality. Seismic surveys should cause as little invasion and disturbance as possible, and are completed in the shortest possible time.

The main component of the project is seismic monitoring of the carbon dioxide geosequestration. CO2CRC Project includes three main Stages. To date, Stages 1 and 2 of the Otway Project are completed, Stage 3 is currently in progress. Different Stages

are focusing on different approaches of seismic monitoring including active 4D surface seismic, 4D VSP, time-lapse offset VSPs, remote monitoring with DAS receivers in the wells and SOVs, multi-well 4D VSP, passive VSP.

Figure 3-1 Location of CO2CRC Otway Project. Reproduced from CO2CRC .

3.2 Geology of the Otway Basin

3.2.1 Tectonics, stress field, stratigraphy, etc.

The Otway Basin is located both onshore (20%) and offshore (80%) of the southern Australian passive margin. The basin was formed by multi-stage rift-sag and inversion phases that led to the formation of numerous spline sealing faults in the area (Krassay, Cathro, and Ryan 2004). The Otway CO2CRC Project site is in the onshore part of the Otway Basin.

Figure 3-2 shows the north-south section with stratigraphy of the study area indicating main formations, faults, and wells with gamma-ray (GR) logging. The shallow part of the section consists of Heyesbury supersequence, which includes limestones (Port Campbell Formation), marls (Gellibrand Formation) and a relatively tiny layer of sandstones (Clifton Formation) that produces a strong reflection on seismic gathers. Underlying Nirranda supersequence consists of marls (Narrawartuk

Formation), sandstone and shale shallow marine sediments (Mepunga Formation). Wangerrip supersequence consists of interlayering of mudstones and sandstones. It includes Dilwyn Formation sandstones, Pember Formation mudstones and Pebble Point Formation sandstones. Underlying Sherbrook supersequence consists of frequent mudstone and massive sandstone units. It includes Massacre Formation shales with good sealing capacity, Timboon Formation sandstones, Paaratte Formation sandstones and Skull Greek mudstones. Paaratte Formation was the target interval during Stage 2C of the Otway Project. Underlying Shipwreck supersequence consists of Belfast Formation mudstones and Waarre Formation sandstones. Waarre Formation is a high-porosity reservoir sandstone, which contains CO_2 and methane in variable proportions. At the Otway site, the gas mixture was dominated by methane, which was commercially produced during 1990s through the Naylor 1 well. This depleted gas reservoir was later used as the target interval in Stage 1 of the Otway project. It sits on top of the Otway Unconformity which marks period of compression, folding, uplift and erosion (Krassay, Cathro, and Ryan 2004).

Sherbrook and Shipwreck Formations are affected by number of faults with similar strike direction

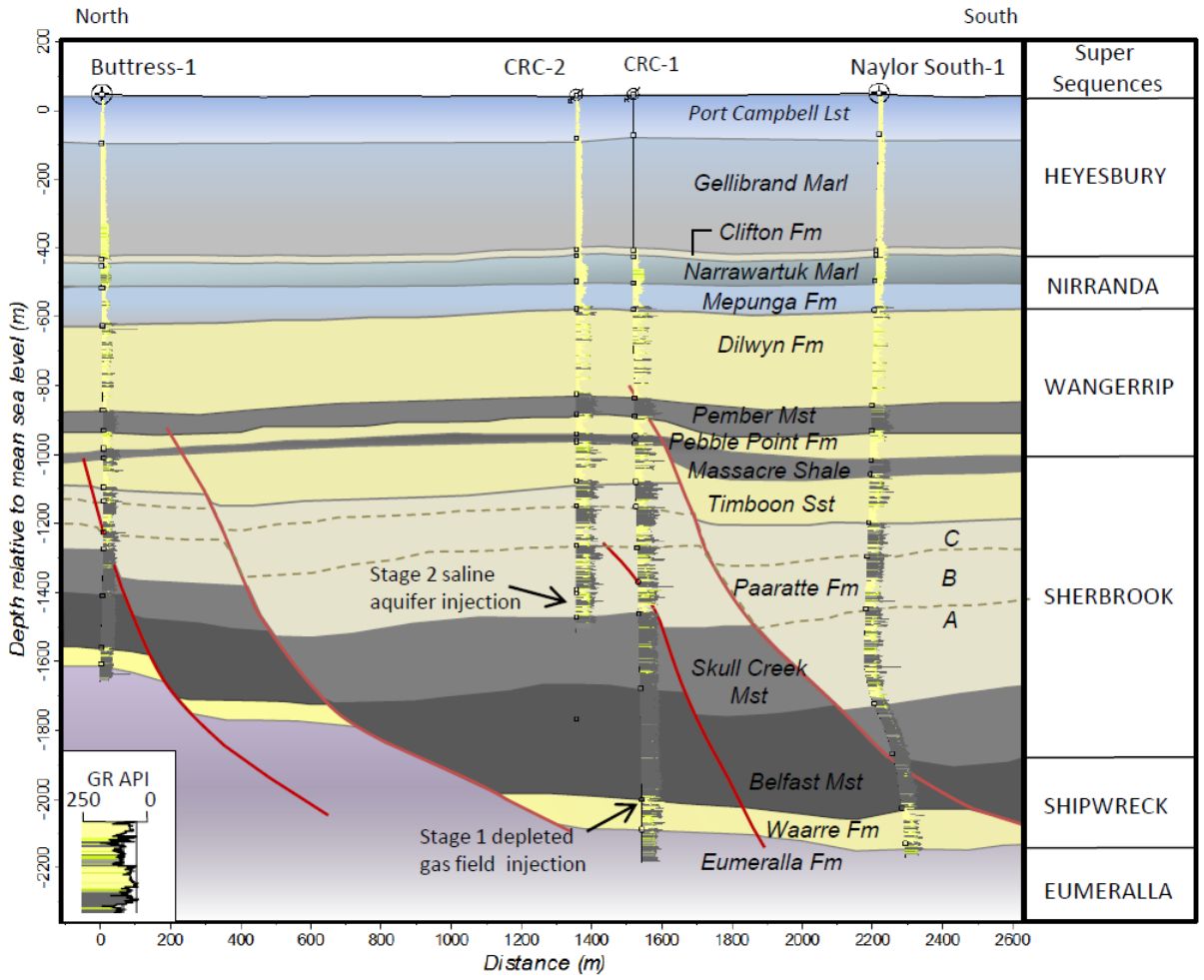

Figure 3-2 North-South section with stratigraphy, faults and wells. The gamma ray (GR) logs are displayed for all the wells. The GR scale represents how the values from 0 to 250 of American Petroleum Units (API) correspond to color scale. Reproduced from Glubokovskikh et al. (2016).

3.2.2 Nature of reservoir and plume

The natural source of the CO_2-rich gas mixture that was captured and injected underground during Stages 1 and 2C of the Otway Project is the Waarre Formation (Turonian age). The gas mixture was produced from the Buttress-1 well from the Waarre Formation at a depth of ~1.6 km. Buttress-1 is located ~2 km north of the Otway facility. At the location, the gas in the Waarre formation consists of 80% carbon dioxide (CO_2) and 20% methane (CH_4). This gas mixture (here and below called Buttress Gas, or simply CO_2) was dried, compressed and transported to the injection site ~2 kilometres by a stainless steel underground pipeline (Dance, Spencer, and Xu 2009). Location of Buttress and Naylor fields is shown in Figure 3-3.

The Buttress gas was injected in the supercritical state into the Waarre Formation through the CRC-1 well (at a depth of ~2 km) during Stage 1 (Figure 3-4) and into the Paaratte Formation through the CRC-2 well (at a depth of 1.5 km) during Stage 2C. After injection, the CO_2-rich mixture remains in supercritical state in the subsurface.

The Waarre Formation (Turonian in age) consists of three units, namely A, B and C. The upper Unit C consists of finely to coarse grained quartz sands and occasional gravels. Unit Waarre-C was the main gas producing reservoir in the area before the commencement of the Stage 1 of the Project. This depleted gas reservoir (Waarre-C) was selected for CO_2 injection in the Stage 1. Waarre-C is overlain and sealed by the Belfast Formation mudstones.

The Paaratte Formation (Campanian to Maastrichtian in age) formed in a regressive marine environment. Within the study area, this formation is up to 400 m thick, and is a quartz-dominated saline aquifer and consists of units of sandstones interbedded with mudstones and siltstones. Individual sandstone packages have variable (1 m to 15 m) thicknesses, high porosities (25–30%) and variable permeabilities in a range of 0–250 mD (Sharma et al. 2011; Cook 2014; Kirste et al. 2014). The total dissolved solids (TDS) of the reservoir (Paaratte Formation) pre-injection brine were in the order of 800 to 2000 mg/L (Dance and Paterson 2016).

The high permeability of some sandstone packages together with the relatively high porosity of the saline aquifer and the presence of seals overlying the target interval demonstrate good potential for CO_2 storage. Paaratte Formation sandstones and

overlying Timboon sandstones are overlain by the Wangerrip Group, consisting of the Massacre Shales and the Pember Mudstones, each with good sealing potential. Moreover, the sealing capacity of splay faults in the area provides additional opportunity to hold injected CO_2 volume within the Paaratte Formation. All these features provide a good storage capacity of the Paaratte Formation for the Stage 2C of the Otway Project.

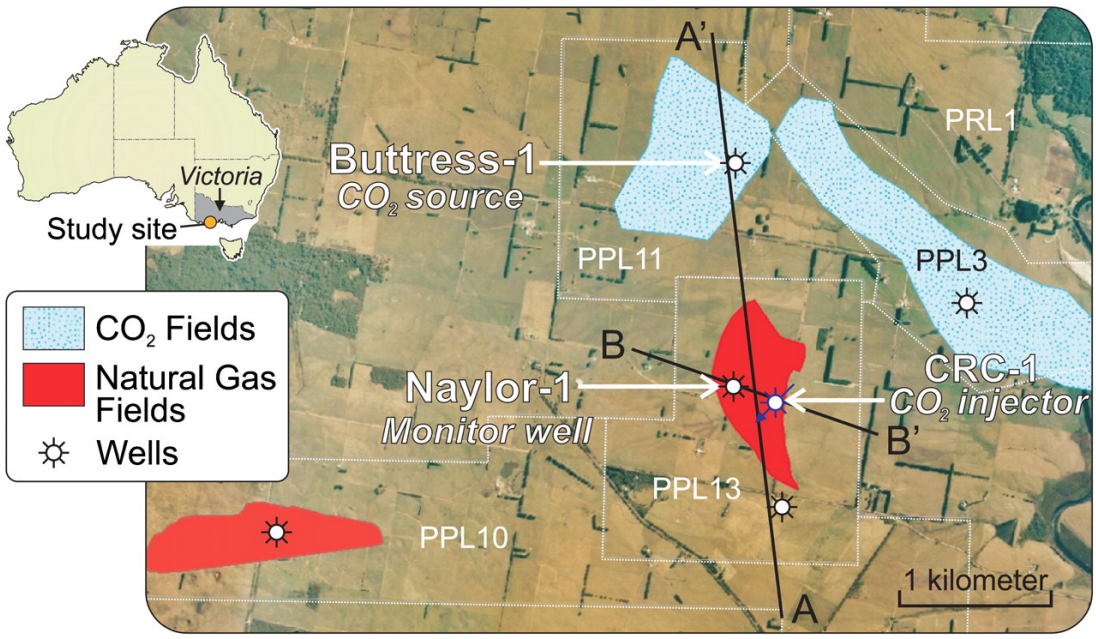

Figure 3-3 Location of Naylor and Buttress gas fields. Reproduced after Jenkins et al. (2012).

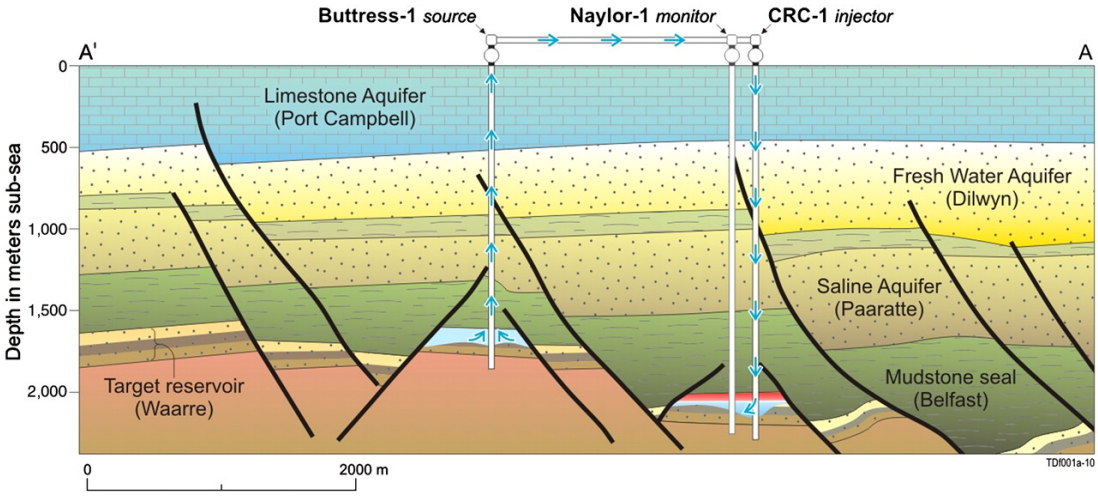

Figure 3-4 Cross-section along the line A'A shown in the Figure 3-3 showing process of Stage 1 injection. CO_2 rich gas from Waarre formation was injected through the CRC-1 well into Waarre-C formation. Reproduced after Jenkins et al. (2012).

3.3 Seismic monitoring in Otway Project

3.3.1 Stage 1: Depleted gas reservoir at 2 km depth

Stage 1 of the Otway project (2007-2010) included the injection of 66,000 tonnes of a supercritical CO_2/CH_4 (80%/20%) gas mixture through the CRC-1 well into Waarre Formation (depleted Naylor gas reservoir) at a depth of ~2025 m (Jenkins et al. 2012; Cook 2014).

Time-lapse (TL) seismic methods such as 4D surface seismic, 4D VSP and TL offset VSPs were used to monitor the injection (Urosevic et al. 2010). 4D seismic was employed using a surface geophone array (~900 receivers) and IVI minivib vibroseis source. 4D VSP was acquired in the CRC-1 well with 8-level 3C geophone string covering the depth level from 1500 m to 1605 m with 15 meter spacing (position of geophone receivers in the CRC-1 well is shown in Figure 5-1). 4D VSP and surface seismic were acquired concurrently. Naylor-1 was used as a monitoring well where walkaway and offset VSP surveys were recorded.

Prior to the beginning of injection, a baseline 3D survey was acquired. Two monitoring surveys were acquired after 35000 and 65445 tonnes of CO_2-rich gas had been injected, respectively. Figure 3-5 shows acquisition geometry for the Stage 1.

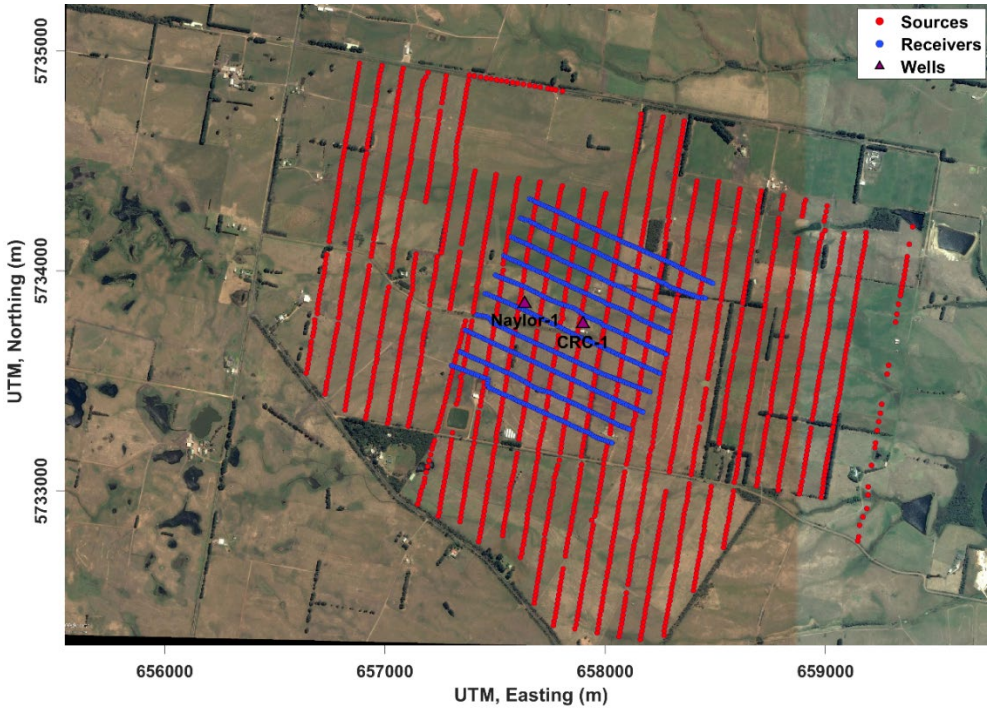

Figure 3-5 Stage 1 seismic acquisition geometry. CRC-1 – well-injector and monitoring well; Naylor-1 – monitoring well.

The presence of residual gas in the depleted Waarre-C reservoir did not cause significant changes in reflectivity after CO_2 injection and led to very small changes in elastic properties of rocks before and after injection. Together with relatively poor repeatability of surface onshore seismic, injection of CO_2-rich mixture did not cause significant time-lapse signal.

3.3.2 Stage 2: Saline formation at 1.5 km, surface and borehole seismic

Stage 2 of the Otway Project consists of three sub Stages namely 2A, 2B and 2C. Stage 2A involved drilling of the CRC-2 well to be used for CO_2 injection into Paaratte Formation. Stage 2B was aimed to determine the residual saturation caused by injection of a small amount (150 t) of pure carbon dioxide into the Waarre reservoir (Cook 2014).

Stage 2C addressed the challenges of monitoring injection of CO_2-rich gas in supercritical state into a saline aquifer (Paaratte Formation) at a depth of 1500 m. The injected amount of CO_2 (15 kt) was small compared with industrial-scale CCS projects around the world, and intended to simulate the scenario of leakage detection from a storage reservoir.

The key component of Stage 2C of the CO2CRC Otway Project was a comprehensive 4D seismic monitoring program using a permanently deployed buried geophone array accompanied by time-lapse 4D VSP and offset VSP surveys. 4D VSP and 4D surface seismic surveys were acquired concurrently to assess the feasibility of both approaches and study how to combine them in an optimal way.

The permanent seismic buried receiver array was installed in order to reduce the impact of the geophysical activity on the farming community and to increase the repeatability of time-lapse seismic data (Pevzner et al. 2015). The buried array reduced the duration of each acquisition survey and remove most of the recording infrastructure (such as cables, geophones, etc.) from the surface.

Figure 3-6 represents the schematic timeline of key parts of the Otway Stage 2C, including installation of the permanent seismic buried receiver array, acquisition of BL seismic survey, injection of 15 kt of a CO_2/CH_4 supercritical gas mixture, and continuous seismic monitoring of the injected fluid during the injection process and after its completion. Over the three years, six 3D surface seismic vintages were acquired: BL and five monitor (M1–M5) surveys (Figure 3-6). The M1, M2 and M3

seismic datasets were recorded after injection of 5 kt, 10 kt, and 15 kt (end of injection), respectively. Injection was paused for the acquisition of the M1 and M2 surveys. M4 was acquired nine months and M5 23 months after the end of injection.

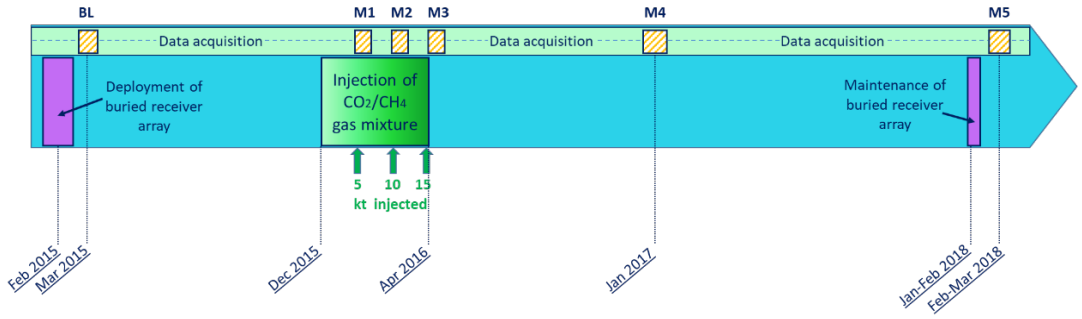

Figure 3-6 Schematic timeline of the Stage 2C of the CO2CRC Otway Project.

Multiple tests conducted prior to Stage 2C showed that repeatability of 4D seismic data in the target area significantly depends on changes in the near-surface conditions, mainly caused by variations in water saturation (Pevzner et al. 2011; Al-Jabri and Urosevic 2010). In order to minimise the effects of such variations on seismic data, all the seismic surveys were acquired in the dry season of the year (between December and April), when variations in near-surface conditions are relatively small and soils are less damaged by vibroseis trucks.

The geophones were deployed in four-metre bores with 15 m intervals. All communication cables and field digitising units (FDU) were buried in 0.8 m trenches. The cross-line distance between receiver lines is about 100 m. Only enclosure boxes, which house crossline units, were installed on the surface along the backbone line responsible for power distribution and data communication from the central recording unit is housed in a "seismic hut". The geophone array consists of 908 vertical-component, high-sensitivity geophones forming 11 receiver lines (Figure 3-7). Along with the benefits in improved data quality and acquisition duration, the permanent installation also decreased the processing time span from the field data to a time-lapse image of the plume to between three to four days.

The extensive seismic monitoring program included other surface and borehole techniques. A fibre-optic array was deployed in the same trenches along with the buried receiver cables to record surface seismic data as a distributed acoustic sensor (DAS) (Yavuz et al. 2016; Correa et al. 2017). Concurrently, a set of downhole seismic time-lapse measurements were conducted using various receivers: 3D VSP surveys in the CRC-1 well with a three-component 10-level VSP tool (located at 760-895 m MD

interval) (Tertyshnikov et al. 2018; AlNasser et al. 2017), and datasets with DAS-cables deployed in the tubing of the CRC-2 well (Correa et al. 2018). In addition, zero-offset and offset VSP surveys were acquired (Tertyshnikov et al. 2017).

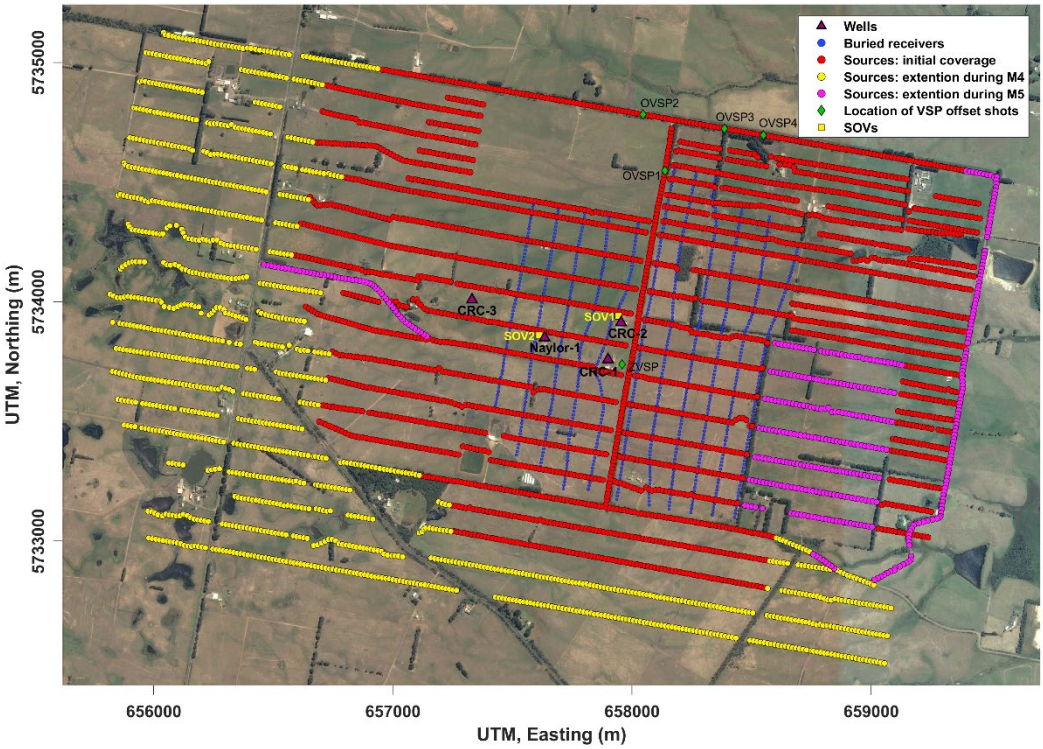

Figure 3-7 Stage 2C seismic acquisition geometry. CRC-2 – well-injector.

The energy sources for all seismic surveys in Stage 2C were 26,000 lbs (11,793 kg) vibroseis trucks. Two trucks were used to speed up data acquisition. The data was acquired with a single 24 s linear sweep per shot point with a 6–150 Hz frequency range, 0.5 s cosine tapers, 5 s listening time and 70% peak force. The source line spacing varied from 50 to 100 m and the distance between the source points was 15 m (Figure 3-7).

The total number of source points was 3003 for the BL, M1, M2 and M3. During M4 survey, the source coverage was substantially expanded to the west and south from the BL and the total number of sources became 4299 (Figure 3-7). The reason for the extension was to significantly increase the illumination zone of 3D VSP and surface seismic data near the CRC-3 well area (drilled in 2017 for the Stage 3 of the Otway Project). By the beginning of the M5 data acquisition, some land access issues had been resolved and the southeastern part of the survey area, which was previously inaccessible, was covered with shot points (Figure 3-7). This extension was highly significant as it increased the seismic fold in the area of the plume location.

Furthermore, during the M5 survey, additional data was obtained with shot points located along the roads. The total number of source points for the M5 survey was 4726.

3.3.3 Stage 3: Saline formation at 1.5 km depth, multi-well downhole seismic with DAS

The seismic monitoring within the Stage 2C of the Otway Project demonstrated that TL surface and borehole seismic monitoring can reliably detect and track a plume containing as little as several thousand tonnes of supercritical CO_2 within a saline aquifer. These results show that surface and borehole seismic method is a viable technology for monitoring and verification of containment of injected CO_2, capable of detecting leaks into overlaying strata.

However, the standard 4D seismic technology faces a number of challenges, such as:

- Relatively high cost compared to other geophysical or remote sensing techniques;
- significant time delay between the data acquisition and the availability of the interpreted results;
- sparseness in sampling of the temporal changes in the subsurface;
- relatively high level of invasiveness and, as a result, difficulties with access to sensitive areas to conduct frequent 4D surveys (this is almost always the case on land and quite often in marine environments as well);
- relatively low sensitivity due to relatively poor repeatability of land 4D seismic surveys (or high level of TL noise) caused by both seasonal variations in the near surface conditions and higher ambient noise level (which includes natural, such as the wind, and human-related, such as operating machinery and traffic, noise sources).

These challenges can potentially be mitigated using borehole-based seismic monitoring. The findings of the seismic program within Stage 2C have demonstrated that borehole seismic methods, such as TL multi-offset, walkaway and especially 4D VSP have sensitivity similar or superior to surface seismic, and have much smaller surface footprint and cost. Testing this strategy became the key objectives of the Stage 3 monitoring strategy.

Thus, Stage 3 aims to develop borehole monitoring concept that is capable to provide reliable and continuous observations of the plume behaviour. Stage 3 also includes automation and optimisation of time-lapse borehole data acquisition and real-time onsite processing (Pevzner et al. 2021; Isaenkov et al. 2021). This is achieved through the utilisation of permanently installed fibre-optic cables in the wells used for DAS VSP, and surface orbital vibrators (SOV) permanently installed at the site (Jenkins et al. 2021). 3D VSP with vibroseis sources and DAS is also utilised as a more reliable monitoring method that provides better spatial illumination and coverage than offset VSP.

In addition to the existing wells at Otway site, prior to the beginning of the Stage 3, four new monitoring wells were drilled in 2020, namely CRC-4, CRC-5, CRC-6 and CRC-7. All the new wells are deviated. BL Stage 3 survey was acquired in March, 2020. Figure 3-8 shows acquisition map of this survey. Five wells fully covered with fibre-optic cables were utilised for SOV and vibroseis VSP surveys. Nine SOVs are deployed on site. In this thesis I utilise multi-well 3D VSP data acquired with vibrosources.

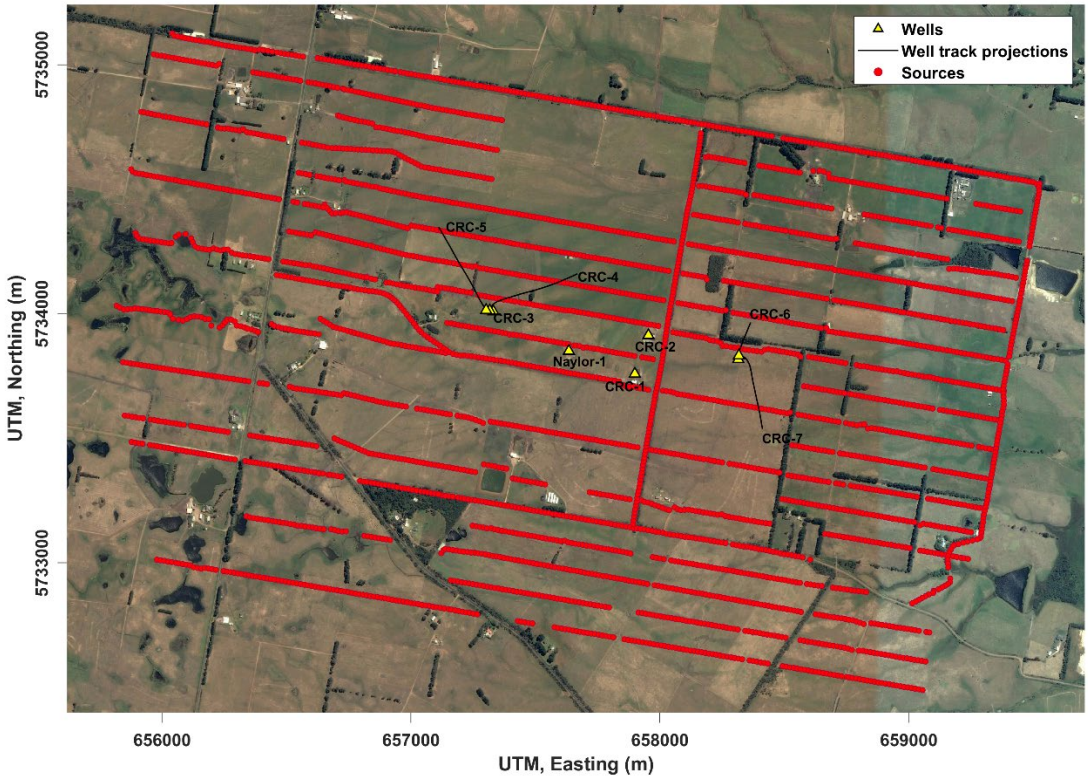

Figure 3-8 Baseline Stage 3 seismic acquisition geometry. CRC-3, CRC-4, CRC-5, CRC-6, CRC-7 – monitoring wells instrumented with DAS receivers.

Chapter 4.
Stage 2C of the project: Surface seismic monitoring of CO_2 injection using buried geophone array

In this chapter I present an in-depth analysis of the 4D surface seismic data acquired with the buried receiver array for Stage 2C of the Otway Project. I describe seismic data processing flow, present time-lapse results after the processing of baseline survey (BL) and five monitor surveys, and analyse evolution of the plume in the subsurface as mapped from surface seismic data. I also study the effect of reducing the number of seismic sources on the detectability of the plume by applying two approaches to imitate field geometry: random and regular distribution of seismic sources. This analysis is useful for optimising seismic acquisition campaigns and especially important for areas with limited access to seismic sources.

Most of the information presented in this Chapter has been published in Popik, Pevzner, Tertyshnikov, et al. (2020) and Popik, Popik, and Pevzner (2019).

4.1 Seismic data processing

The data were processed with two approaches that differed mainly in seismic migration. The first approach, so-called "express processing", produced plume images in a very short time. This is done using 3D explicit finite-difference FXY post-stack time migration (the data is transformed from time and space (X,Y) to frequency (F) and space (X,Y), a time slice is converted to a frequency slice). This approach gave adequate preliminary results for every vintage, which is essential for monitoring projects because such images refer to the current plume position (rather than after a few months from data acquisition). On average, the turnaround time between the completion of the acquisition and production of the preliminary images was three to four days.

However, a more accurate estimation of the plume extension can be achieved through the application of pre-stack time migration (Popik et al. 2018). This second approach is more time-consuming but ensures much more detailed characterisation of plume's lateral and vertical extension, and significantly improves seismic images in the vicinity of faults. Figure 4-1 compares BL seismic sections after "express processing" approach (a) and more time-consuming pre-stack migration approach (b). Pre-stack migration provides better accuracy and resolution in seismic section, especially in the area close to the faults.

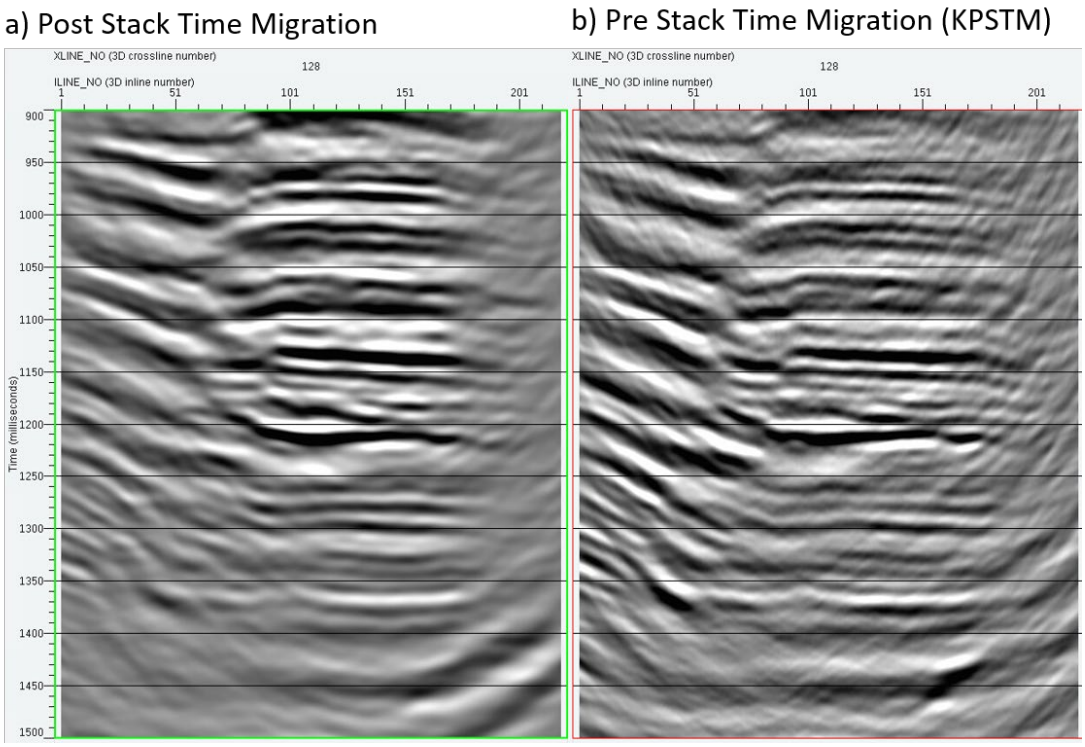

Figure 4-1 Comparison of processed BL data using different migration algorithms: a – post-stack time migration; b – pre-stack Kirchhoff time migration.

In order to obtain changes caused only by the presence of the plume, all vintages were processed using an identical workflow, shown in Table 4-1. The velocity model that was obtained for the BL survey was used to migrate all seismic survey vintages. The detailed data processing workflows of "express processing" and pre-stack migration approaches are summarised in the Appendix C.

Table 4-1 Data processing workflow. Different migration approaches were used to process the data: post-stack migration was used for "express processing" approach and pre-stack migration algorithm utilised to obtain more reliable results. Appendix C provides more details on the processing workflows and the parameters used.

Processing stages	**Procedures**
Data Input and geometry assignment	SEG-D data input; Correlation with sweep signal; Geometry assignment; Binning; Trace editing
Velocity analysis and statics	Velocity analysis; Elevation statics
Noise attenuation	Time-frequency domain noise attenuation; Ground roll removal
Deconvolution	Surface-consistent spiking deconvolution
Residual static corrections	Surface-consistent MaxPower autostatics
Migration	Pre-stack Kirchhoff Time Migration (KPSTM) or CDP stacking and Post-stack migration: 3D explicit finite-difference FXY post-stack time migration
Post-migration processing	FK-filtering (frequency-wave filter applied after two-dimensional Fourier Transform); Stacking (in case of KPSTM); FK-filtering; FXY-deconvolution

All geophones had identical positions throughout all six surveys, and thus the receiver geometry remains exactly the same. Additionally, the initial high signal-to-noise ratio of data obtained using the buried geophones helped avoid some noise-attenuation procedures and allowed reliable detection of as little as 5 kt of the injected CO_2.

Processed results were cross-equalised using estimated time shifts between each monitor survey and the baseline survey. Time shifts were calculated based on the cross-correlation computed in a 400 - 1170 ms window (above the plume position) and applied to match all monitor surveys to the BL survey. The time-shift maps are shown in Figure 4-2; the histogram represents the distribution of values in milliseconds. The

maximum absolute value of time shifts within every vintage is indicated above the histogram. Time shifts carry information about changes between surveys, which are most probably caused by variations in near-surface conditions. Thus time shifts can be considered as one of the measures of repeatability between any of the two surveys.

Generally, values of time shifts are between -0.5 ms and 0.5 ms within the zone of interest (around the CRC-2 injector well). Among all the surveys, the M3 seismic data appear to be the closest to the BL data (Figure 4-2c), while the M2 data show the least repeatability (Figure 4-2b).

4.2 Plume images

Evolution of a CO_2 plume can be investigated by tracking the time-lapse seismic anomaly. This also helps to verify that there is no leakage of injected gas and plume is safely stored in a subsurface. Thus, after the parallel processing of all the vintages, resulting differences between each monitor surveys and BL survey were analysed across the difference cubes. Here I show a few slices crossing the plume after full Kirchhoff PSTM data processing approach. Figure 4-3 shows a map of Stage 2C acquisition geometry with the position of control lines: IL110, XL124 and one arbitrary line. CRC-2 was an injection well during the Stage 2C, so all the selected lines are crossing the plume. Figure 4-4 and Figure 4-5 show the results of data processing for IL110 and XL124, respectively. The first panel represents the BL stack data and the following panels show the differences, or time-lapse anomalies, between each monitor survey and the BL. All differences indicate clear time-lapse anomalies caused by the presence of injected CO_2 at around 1210 ms level, which corresponds to the injection depth of 1.5 km in the CRC-2 well.

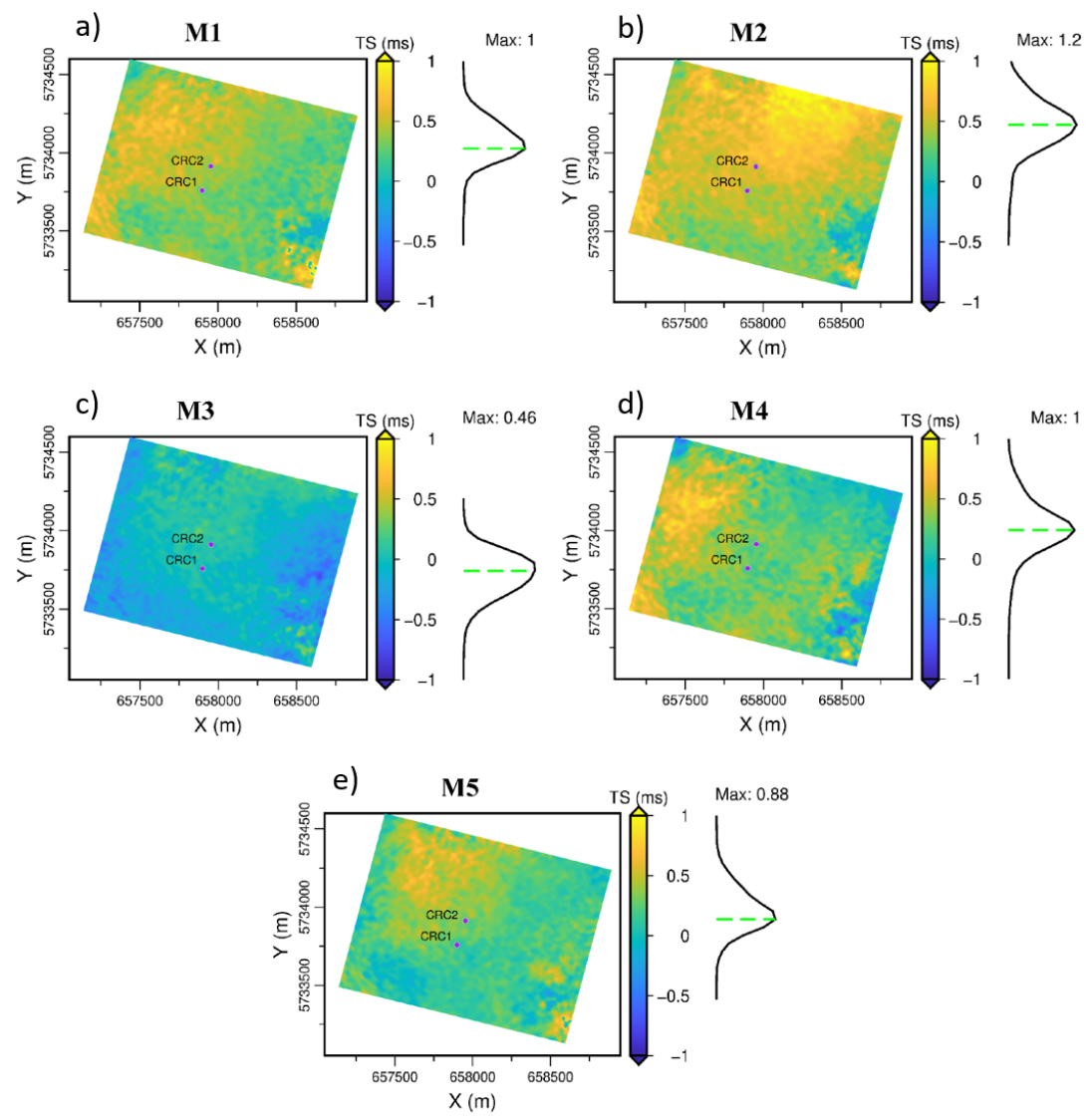

Figure 4-2 Maps of time-shifts calculated in 400-1170 ms window between: a – M1 and baseline; b – M2 and baseline; c – M3 and baseline; d – M4 and baseline; e – M5 and baseline.

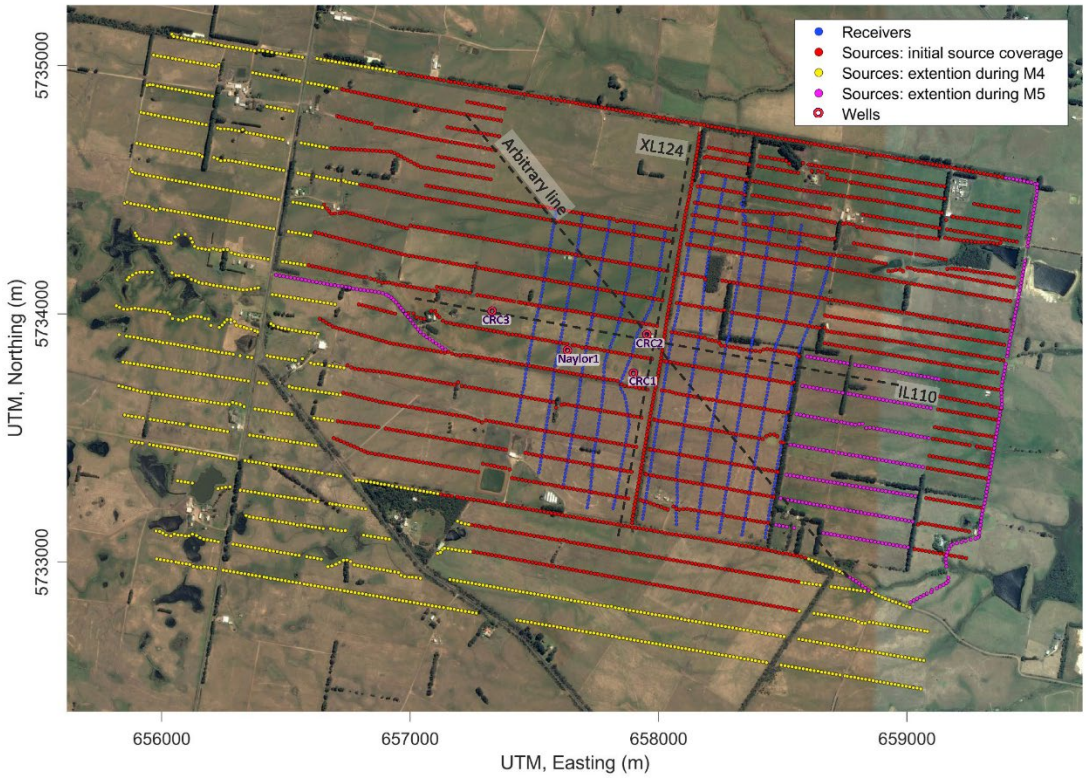

Figure 4-3 Surface seismic acquisition geometry. Dashed black lines show location of the seismic sections represented on Figure 4-4, Figure 4-5 and Figure 4-8.

Comparison of different seismic sections shows that the surface seismic can robustly track the time-lapse signal throughout the monitoring surveys. The plume anomaly has significantly higher amplitudes compared with surrounding random events on difference sections.

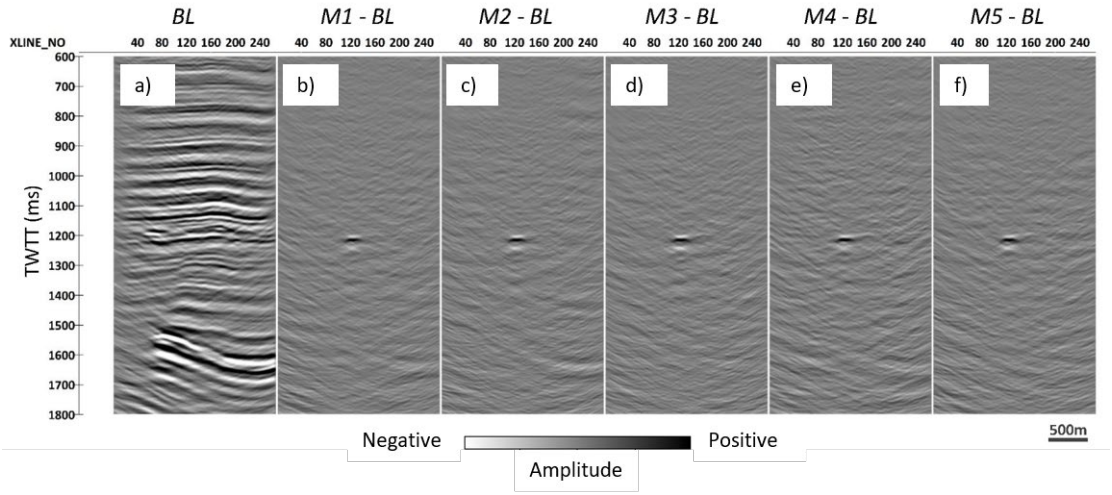

Figure 4-4 IL110 (crossing injector well CRC-2). BL stack (a) and time-lapse signals after each monitor survey: b – M1; c – M2; d – M3; e – M4; f – M5.

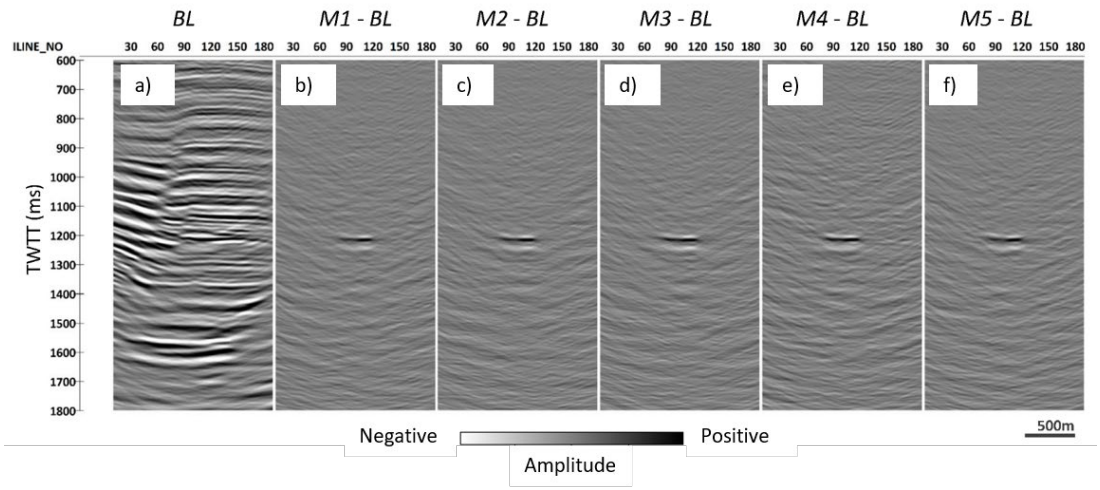

Figure 4-5 XL124 (crossing injector well CRC-2). BL stack (a) and time-lapse signals after each monitor survey: b – M1; c – M2; d – M3; e – M4; f – M5.

In order to investigate the lateral distribution of the plume and its evolution over time the root mean square (RMS) amplitudes of the time-lapse signal for each monitor were calculated. Figure 4-6 shows RMS amplitudes of the difference sections estimated in 24 ms window centred at the injection level (1210 ms). All the RMS images are normalised by the same value, namely the average noise level.

One can observe how the plume's behaviour is changing over time. Injection of 5 kt of CO_2 produced a small and roughly circular anomaly around the CRC-2 injector. With the continued progress of the injection, the plume spreads in a south-eastern direction, which is clearly traced by the M2 and M3 surveys. Post-injection surveys show that the plume continued to extend further towards the south-east. Between M4 and M5 there is almost no difference in the lateral distribution of the plume (Figure 4-6).

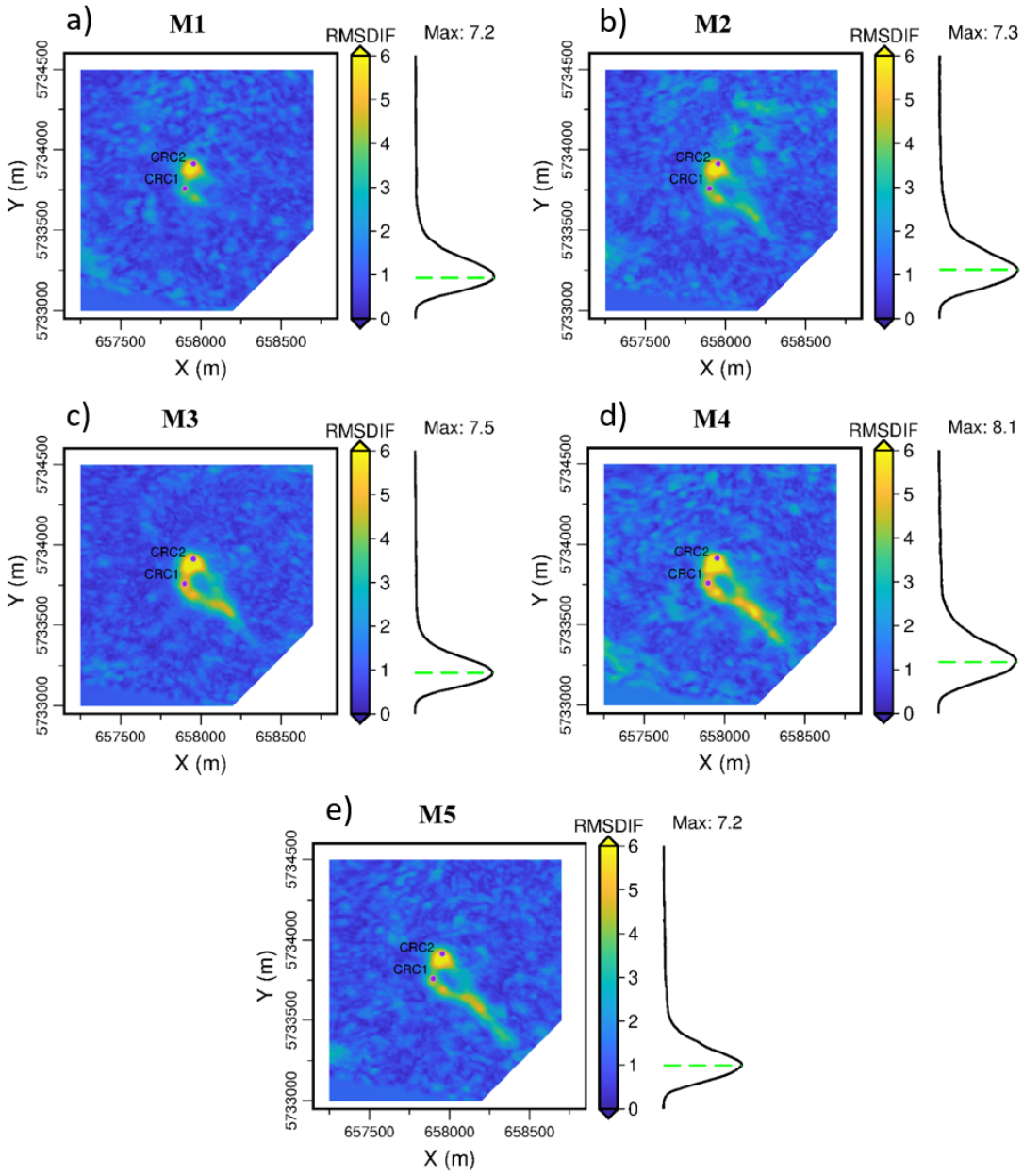

Figure 4-6 Maps of the RMS amplitudes of the time-lapse signal obtained in 24 ms time window centred at 1210 ms (corresponding to the injection interval) for: a – M1; b – M2; c – M3; d – M4; e – M5. The histograms show the distribution of the ambient noise presented on each map. The value "Max" is the maximum amplitude of the time-lapse signal (after normalisation) for each monitor.

4.3 Interpretation of plume development

It is important to verify that the injected CO_2 is stored safely underground and no leakage of injected CO_2 into overlying strata occurs. The first few percent of the substitution of the initial pore filling fluid (brine) by the CO_2 cause a significant effect on the rock's stiffness and hence on P-wave propagation (Caspari et al. 2015). Thus, even slight changes in CO_2 saturation caused by leakage would already cause a detectable seismic time-lapse signature. A thorough analysis of difference cubes (Figure 4-4 and Figure 4-5) of all monitor surveys demonstrates the strong time-lapse anomaly at the injection level and absence of time-lapse signal in the overburden. This means that at this monitoring resolution, the plume does not migrate upwards. The capabilities and limitations of the time-lapse seismic characterisation of a small CO_2 leakage based on the Otway data are discussed in more detail in Glubokovskikh et al. (2019).

The plume observed in the M5 survey looks very similar to the one observed in the M4 survey, but has a slightly larger lateral extent (Figure 4-6). To understand the evolution of the lateral extent of the plume, it is useful to define the boundary of the 4D anomaly for every vintage. A straightforward way to do this is by defining threshold values for every vintage. I chose as the threshold the level of RMS amplitudes where a time-lapse signal is uniquely distinguished from the surrounding noise level. The threshold was estimated along RMS time slice calculated in 24-ms window centred at 1198 ms (an upper part of the layer with injected CO_2). As each vintage has its own noise level, the threshold value is different for each monitor survey. Thus, data from the M1, M3 and M5 surveys with higher repeatability gave lower threshold values (between 1.6 and 1.7) while the noisier data of the M2 and M4 surveys gave higher threshold values (1.9 and 2, respectively).

Figure 4-7 shows the plume anomaly defined by the threshold values. The M1 plume anomaly is localised near the CRC-2 injection well. In the following vintages, the preferential trend of the plume migration is in a south-eastern direction.

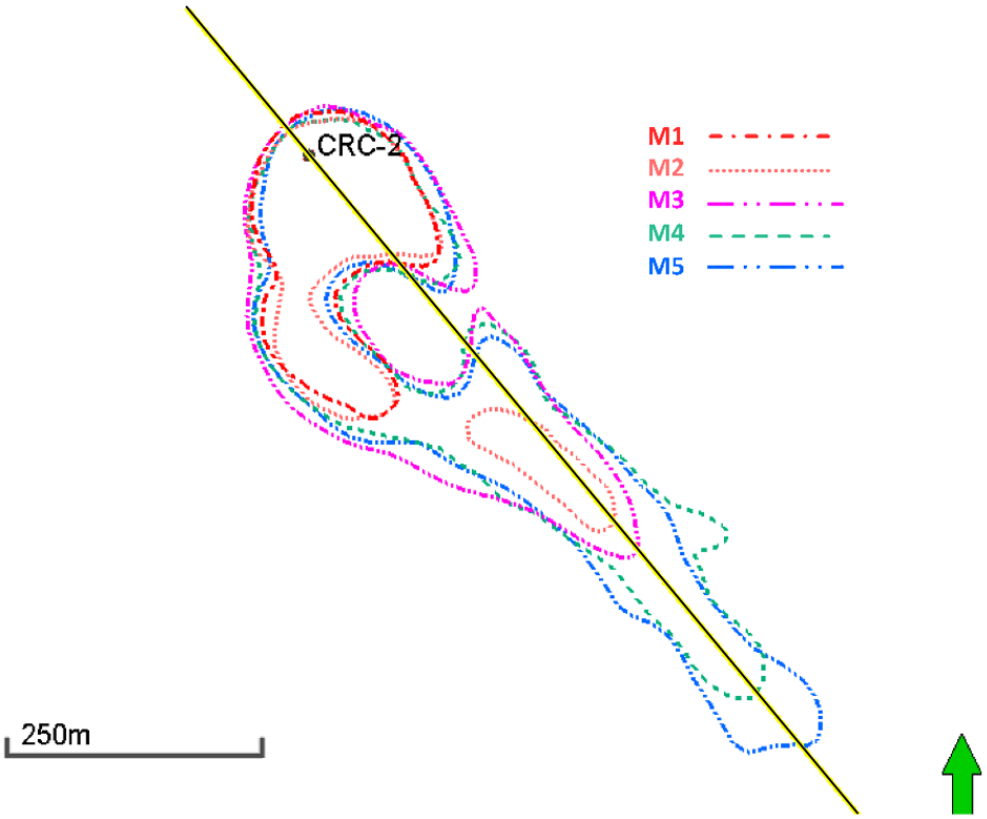

Figure 4-7 Evolution of the plume shape defined by threshold values. Yellow/black line is the arbitrary line crossing the injection well CRC-2 and going through the main direction of the plume migration.

Note that the higher level of noise in the M2 and M4 surveys has created false anomalies with a signal strength close to that within the plume. This means that the boundaries of the plume in these surveys are defined with significant uncertainty, while the M1, M3 and M5 plume areas are estimated more accurately. Table 4-2 shows the changes of the plume area for all the monitor surveys. It also shows changes in the length of the plume along the axis passing through the main direction of plume migration (shown as a yellow/black line on Figure 4-7). The plume area increased mostly between the M1 and M3 surveys and expanded only by about 13 % between the M3 and M5 surveys.

Table 4-2 Changes of the plume shape between all monitor surveys.

	M1	M2	M3	M4	M5
Plume Area, m^2	32400	35500	70100	75150	79200
Length along the NW-SE axis, m	150	500	530	740	780

Following the end of injection (M3 monitor), the plume migrated ~250 metres in a south-eastern direction and the total extent of the plume along the line in the M5 survey became ~780 meters. As can be observed from Figure 4-7, most of this plume spreading took place before the M4 survey; plume extension after that has been insignificant.

Figure 4-8 shows a time-lapse signal along an arbitrary line passing through the main axis of the plume spreading and crossing the injector CRC-2 well (see slice position in the lower left corner of the figure). The plume occupies almost one half of the arbitrary line and its extension on the M5 vintage almost approaches the edge of the survey area. Thus, it is important to increase the seismic fold in this area. This was achieved during the M5 data acquisition by adding source lines in the southeastern part of the survey (Figure 4-3). Analysis of the extended survey demonstrated that no anomalous migration of the plume was detected.

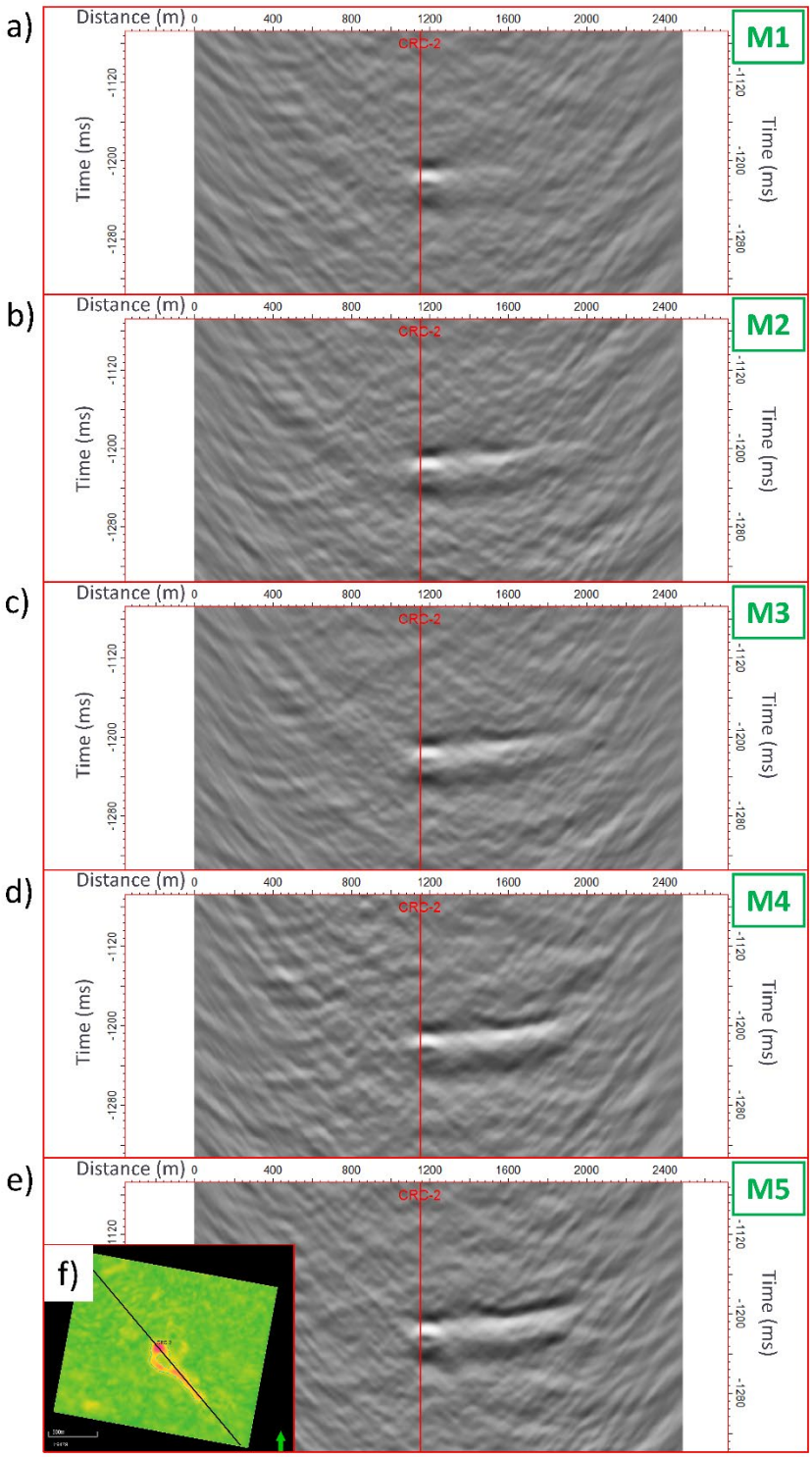

Figure 4-8 Evolution of a time-lapse signal (a – M1; b – M2; c – M3; d – M4; e – M5) along the arbitrary line crossing the well-injector CRC-2 and the plume's main axis (black line on the time-slice (f) of RMS amplitudes for M5 survey (same as arbitrary line from Figure 4-3 and the NW-SE striking line from Figure 4-7).

4.4 Analysis of source effort effect on the detectability of plume

Compared to surface geophones, the use of permanently buried geophone arrays for reservoir monitoring provides a number of advantages, such as higher SNR and reduced acquisition time. However, such installations are costly, and hence the number of seismic receivers is relatively small. This effect can be mitigated by increasing the density of seismic sources, which increases the data quality but also the cost and environmental footprint of the survey. The latter is especially important for cases where 4D seismic is deployed in sensitive land areas. Thus, it is important to understand the trade-off between the data quality and the source effort. In this study I use the 4D seismic data acquired in Stage 2C of the CO2CRC Otway Project to investigate how the source effort can be optimised (Popik, Popik, and Pevzner 2019).

To study the effect of source effort on TL images I use data obtained during BL and one of the monitor surveys (M3) corresponding to the end of 15 kt injection. I have considered two approaches of source reduction: Regular and random. For every source point selection, I utilise a complete set of seismic receivers. Selected data were subjected to the processing steps of "express-processing" workflow described in section 4.1.

Figure 4-9 Seismic acquisition map for Stage 2C of the Otway project (BL source coverage).

The first approach suggests reduction of the source effort based on a regular source selection (Figure 4-10). According to the results of the fluid flow modelling used for the design of the experiment, the plume was expected to migrate in the North-East direction from the injector (CRC-2). This explains the doubled source density in the NE quadrant of the survey (Figure 4-9). First, I excluded this additional source lines in the NE part of the survey (selection 1), which corresponds to reduction of the total number of sources by approximately 20% (Figure 4-10a). Then, in addition to the previous selection, every second source in each source line was excluded (Figure 4-10b) and only 40% of the original trace count are used for imaging (selection 2). This selection increased the in-line source spacing from 15 m to 30 m. Finally, from the remaining data, I discarded every 2nd source line (Figure 4-10c), thus limiting the source effort to ~20% of the original (selection 3).

Another data reduction approach is random source selection (Figure 4-11). Selection 4 randomly excludes 25% of sources (Figure 4-11a), selection 5 – 50% of initial sources (Figure 4-11b) and in selection 6 – 75% of data were excluded (Figure 4-11c).

Figure 4-12 and Figure 4-13 illustrate inline and crossline seismic sections crossing the plume. All these images are obtained after post-stack migration. Section a shows BL migrated stack obtained with initial number of sources. Section b shows the difference between monitor and BL surveys (TL signal) obtained with the full initial acquisition geometry. Sections c – e show TL signals obtained after regular selection approach and represent selections 1, 2 and 3, respectively. Sections f – h show TL signals after random exclusion of 25 % (f), 50% (g) and 75% (h) of the initial number of shots.

Figure 4-14 shows maps with RMS-amplitudes of TL signals for initial number of shots (Section a), for regular source selections 1, 2 and 3 (Sections b – d) and for random source selections 4, 5, 6 (Sections e – g). RMS-amplitudes were computed in rectangular 24-ms window that corresponds to the level of injection.

The seismic sections and RMS-amplitude maps show that all considered source decimation approaches allow reliable detection of the plume. Even 20-25% of the initial number of sources (selections 3 and 6) are sufficient to detect the plume. However, this might not be sufficient to study the behaviour of plume in detail.

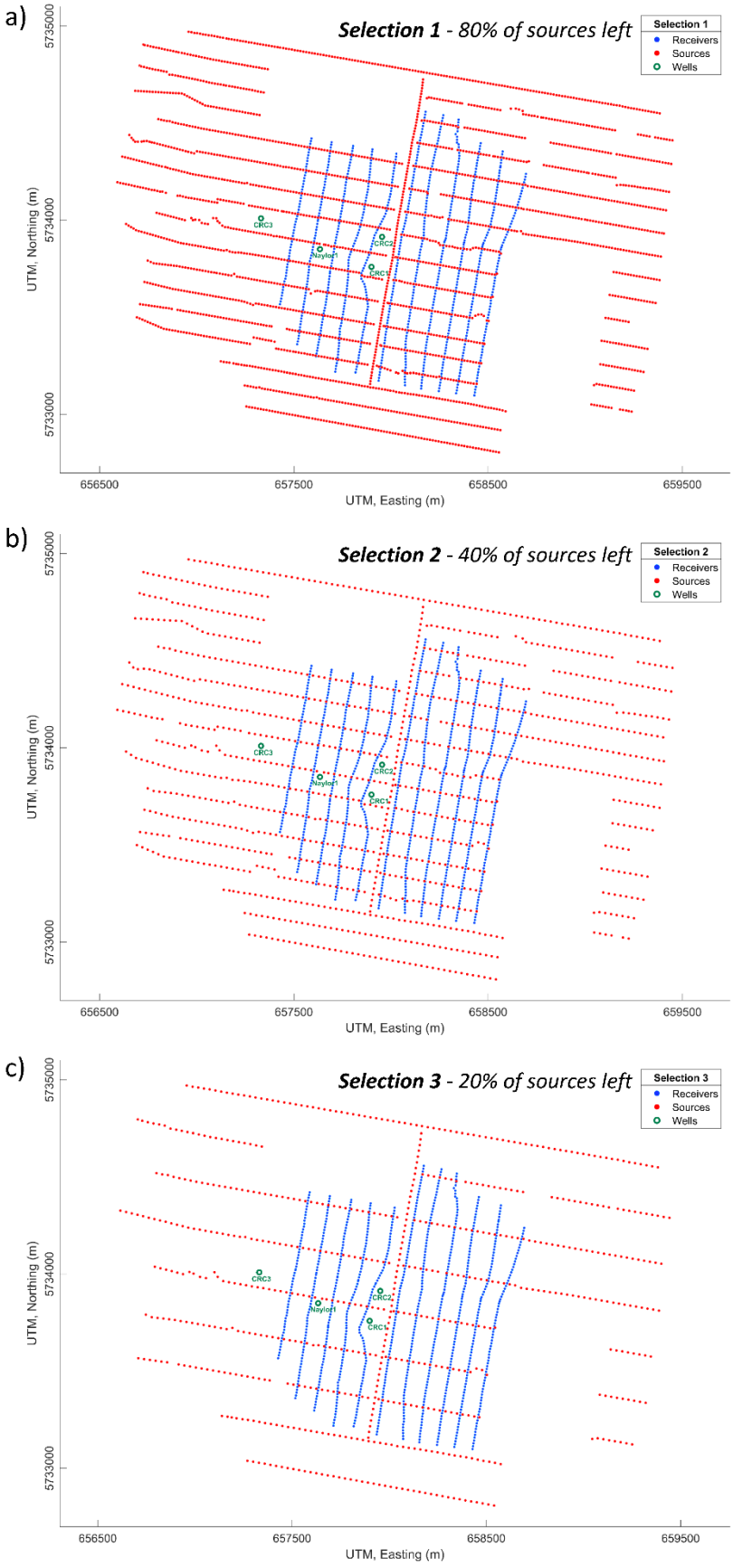

Figure 4-10 Seismic acquisition map after regular source reductions: a – selection 1; b – selection 2; c – selection 3.

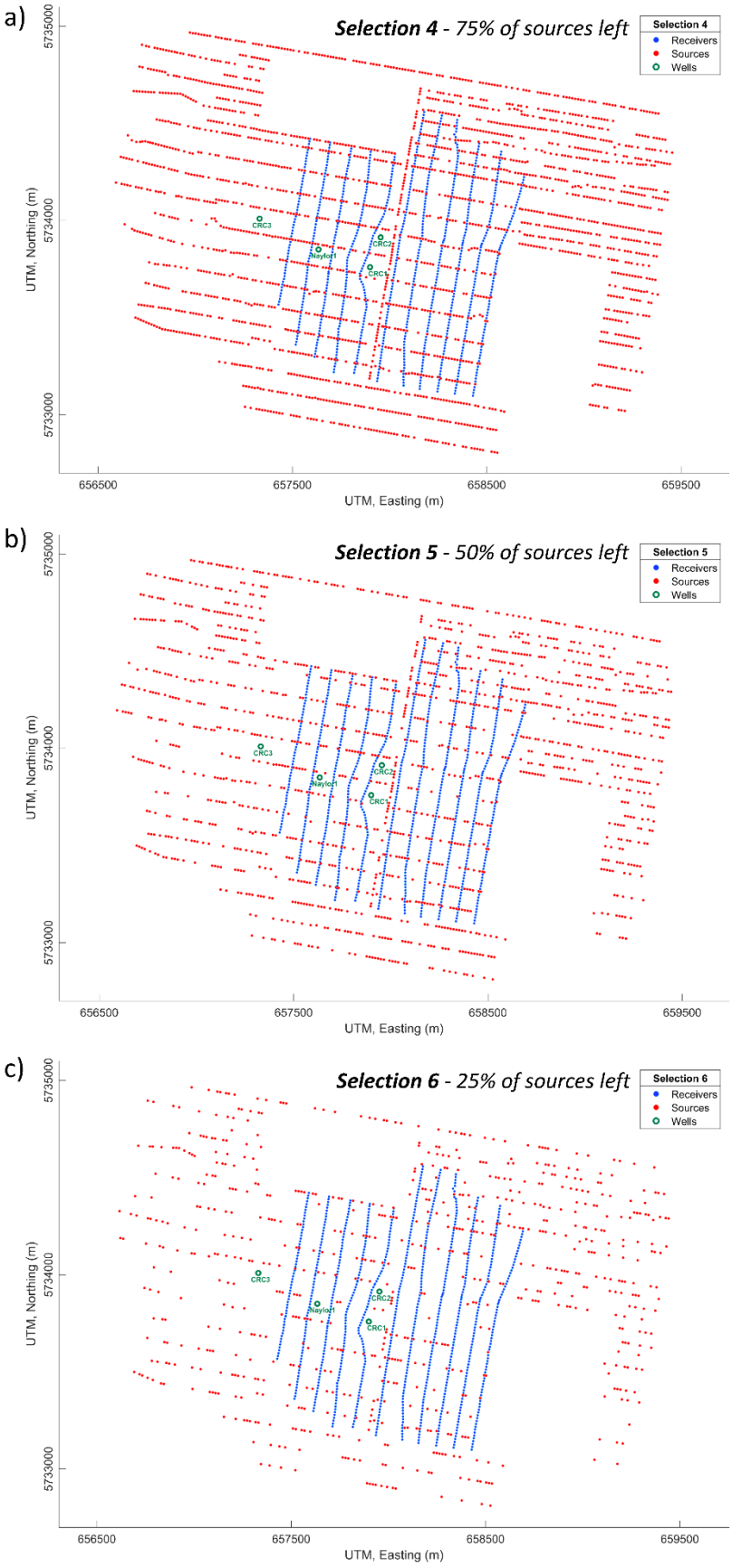

Figure 4-11 Seismic acquisition map after random source reductions: a – selection 4; b – selection 5; c – selection 6.

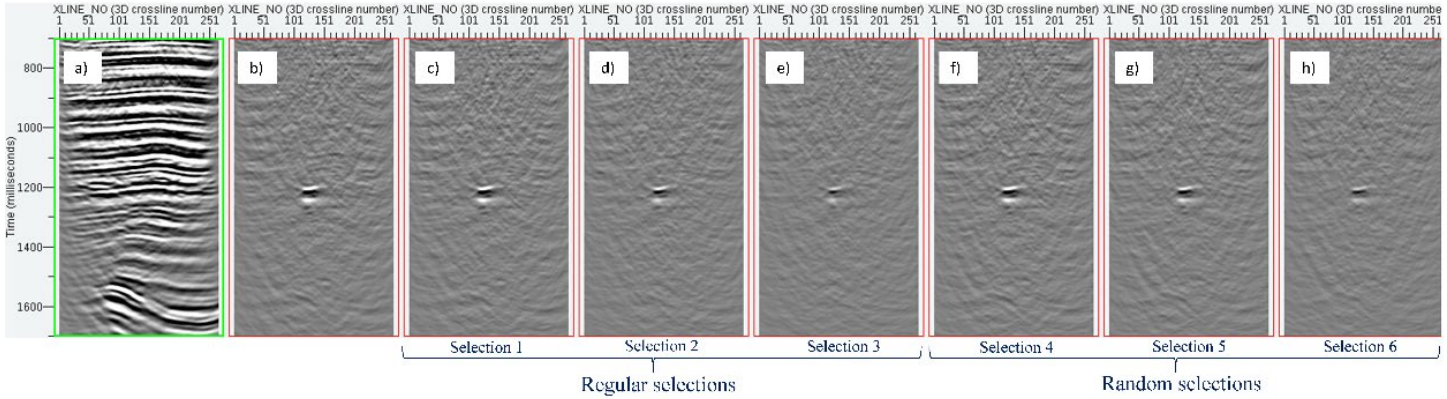
XLINE_NO (3D crossline number)
Time (milliseconds)
800
1000
1200
1400
1600
a)
b)
c)
d)
e)
f)
g)
h)
Selection 1
Selection 2
Selection 3
Selection 4
Selection 5
Selection 6
Regular selections
Random selections

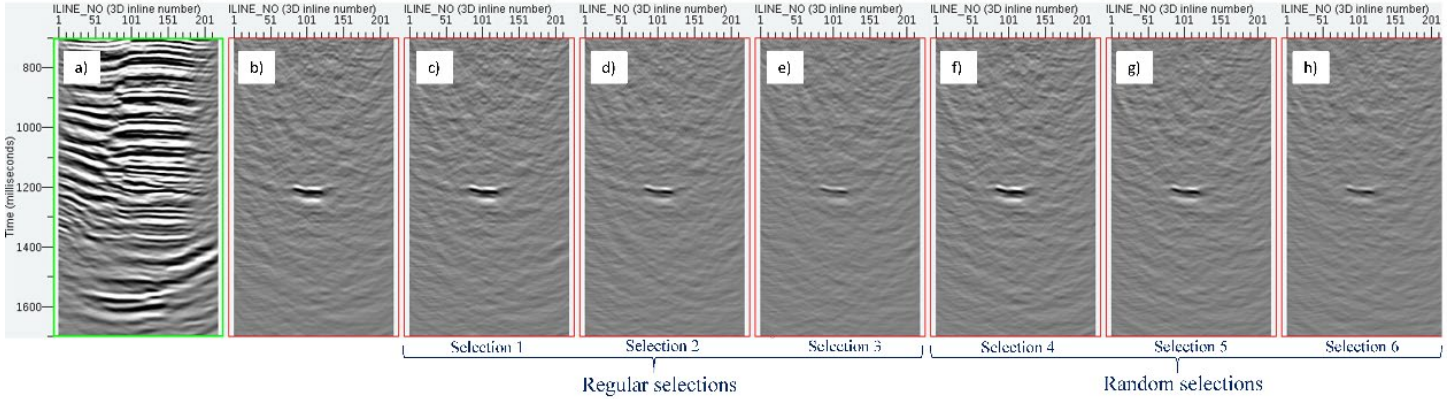
ILINE_NO (3D inline number)
Time (milliseconds)
800
1000
1200
1400
1600
a)
b)
c)
d)
e)
f)
g)
h)
Selection 1
Selection 2
Selection 3
Selection 4
Selection 5
Selection 6
Regular selections
Random selections

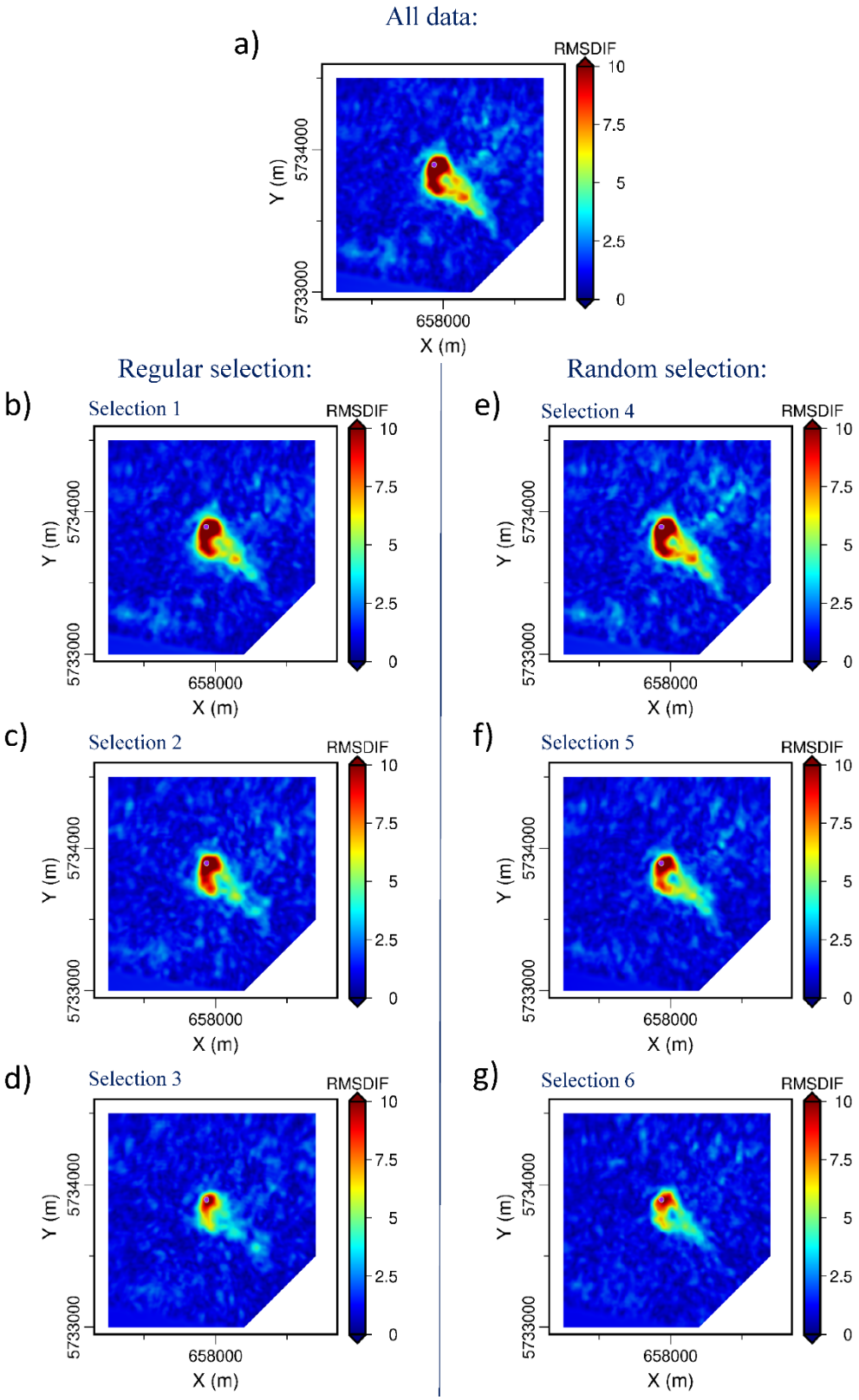

Figure 4-14 Maps of RMS-amplitudes of differences between monitoring and baseline surveys (TL signal). a – Initial number of sources; b, c, d – regular selections 1, 2 and 3, respectively; e, f, g – random selections 4, 5, 6, respectively. Purple circle on the maps – location of injection well CRC-2.

4.5 Conclusions

The high quality of the acquired reflection seismic data together with the data processing strategy we developed allow reliable surveillance of the plume evolution. The time-lapse seismic response provides excellent detectability of the changes in plume shape and lateral spreading. Analysis of the obtained post-stack seismic data cubes shows the absence of the unwanted migration of the plume away from the primary injection unit. In summary, the results show that the implemented monitoring approach is an effective and robust controlling strategy for carbon dioxide storage projects.

I have also investigated the relations between the source density and quality of the TL image obtained in Stage 2C of the CO2CRC Otway Project. Understanding the optimal source effort required to image TL changes in the subsurface is important to minimise time, cost and environmental footprint of the 4D seismic campaign.

My results demonstrate that eliminating approximately 20-25% of the source positions has a minimal effect on the final seismic section image quality. Even using a quarter or one fifth of the original sources, while retaining the spatial source coverage and spatially uniform distribution of the remaining source positions, is sufficient to detect the injection, but the image quality would be compromised. Random source reduction provides slightly better processing results compared to the regular decimation (every second source followed by every second source line), although these results could be site specific. Reliable prediction of the acceptable reduction of the source effort requires similar analysis of at least BL data and possibly one monitor survey.

Chapter 5.
Optimisation of velocity model from 3D VSP surveys

The presence of significant P- and S-wave velocity anisotropy at the Otway site has been reported previously based on the analysis and interpretation of Stage 1 data. Pevzner, Gurevich, and Urosevic (2011) and Pevzner et al. (2010) compared anisotropy estimates at the Otway site from zero-offset and 3D VSP data, and the effect of shear-wave splitting. Asgharzadeh et al. (2013) estimated horizontal polar anisotropy from P-wave 3C walkaway Otway VSP data and analysed the reliability of slowness and slowness-polarisation methods for the site.

The main purpose of this study was to find a suitable anisotropic approximation of the travel-time field that can be implemented in a Kirchhoff time migration of 3D surface seismic and 3D VSP data. A wide range of available offsets and azimuths acquired at Stages 2C and 3 at Otway site provides a unique opportunity for anisotropy estimation from 3D VSP data. Utilisation of DAS in multi-well 3D VSP surveys provides additional benefit to acquired data due to possibility to obtain data for the whole depth range of the well. Moreover, multi-well VSP gives opportunity to track anisotropic parameters laterally.

By analysing P-wave direct arrival times on 3D VSP gathers it is possible to study distribution of the travel times with azimuth and depth and also to attempt to estimate P-wave anisotropic properties of the study area. In this chapter I provide P-wave travel-time analysis of all 3D VSP datasets at the Otway site. To this end, I compare geophone and DAS receives for their applicability to the study of P-wave anisotropy estimation at the Otway Site. I consider two approaches of P-wave anisotropy estimation: local and effective. All the approaches are based on the P-wave anisotropy estimation. Finally, I provide the resulting anisotropy parameters and discuss possible causes of the anisotropy at the Otway site.

Significant amount of information presented in this Chapter has been published in Popik et al. (2021), Popik, Pevzner, and Bona (2020); Popik, Pevzner, Bona, et al. (2020).

5.1 3D VSP data used for anisotropy estimation

Study of the propagation of P-waves carries information of P-wave velocity anisotropy (as discussed in Chapter 2). In this section I analyse P-wave travel-time behaviour of direct waves recorded in VSP, which will enable me to estimate P-wave anisotropy, as discussed in the following sections. For the P-wave travel-time analysis, I utilise the first arrival times (direct P-wave arrival) of the 3D VSP data acquired during Stages 1, 2C and 3 of the Otway Project. While surface seismic direct waves propagate in sub-horizontal direction and give us information about "near-surface layer", direct waves recoded along the boreholes carry information about waves that propagate through the media up to the depth of the boreholes. One feature of the direct waves, compared to all the other waves on a VSP gather, is an almost full absence of interference with other types of waves, which allows one to study behaviour of such waves with less uncertainty.

In this study I use both geophone and DAS receiver data. Figure 5-1 shows spatial arrangement of all seismic receivers utilised for the VSP data acquisition at Otway Site. Green dots represent position of geophone receivers. Geophone data from the bottom section of the CRC-1 well was acquired in Stage 1 with source geometry represented on Figure 3-5. All the other geophone receivers were deployed during Stage 2C, including single geophone in the CRC-3 well and geophone array installed in the middle section of the CRC-1well with source coverage shown in Figure 3-7. DAS data in the CRC-3 well was also acquired during Stage 2C. The schematic Figure 5-2a shows Stage 2C VSP receivers in wells CRC-1 and CRC-3 used for the monitoring during M5 survey. Two standard fibres (SF) were connected to two different DAS interrogators throughout the 3D VSP data acquisition. One of the cables (covering the entire length of the well) was connected to a Silixa v2 (https://silixa.com/) interrogator. Another cable (covering a depth range up to 1430 MD) was connected to a Fotech Helios (https://www.fotech.com/) interrogator. The purpose of utilising two different interrogators was to test the acquisition systems and the different configurations of each interrogator. However, for the purpose of this

study, the differences in data from these two interrogators is not significant. Engineered fibre (depicted as CF – Silixa's Constellation fibre) was not connected during Stage 2C data acquisition, it was only used for testing purposes at that stage. Purple lines on Figure 5-1 indicate the position of DAS cables installed in the wells that were utilised during Stage 3 for 3D VSP baseline data acquisition with the Figure 3-8 source coverage. All the 3D DAS VSP Stage 3 data was acquired utilising engineered fibre (CF) with the Silixa interrogator (Figure 5-2b). The Stages 2C and 3 DAS survey acquisition parameters are specified in Table 5-1. Utilisation of engineered fibre provided much better S/N ratio of the data compare to Stage 2C standard fibre data.

Figure 5-3 shows the geophone (a) and DAS (b and c) raw common receiver gathers from CRC-3 VSP (775 m depth) from one shot line. The DAS gather in the section (b) represents Stage 2C data, where a standard single-mode fibre (SF) was used for data recording with Fotech interrogator, the section (c) represents Stage 3 data obtained with engineered fibre (CF) and Silixa interrogator. Overall, the geophone data has much better signal-to-noise ratio and makes tracking the first arrivals much easier. However, there is significant improvement in the DAS data quality when using engineering fibre compare to standard fibre. DAS spectra is significantly different in the Stages 2C and 3 due to different interrogators utilised during data acquisition (while Fotech interrogator measures strain, Silixa interrogator measures strain rate). This difference mostly contributes to the low-frequency part of the spectra.

The main issue with DAS is that even after noise removal from the data, it is still impossible to detect P-wave arrivals at far offsets. This is due to DAS being mostly sensitive to seismic waves polarised and propagating along the cable, since DAS measures strain along the fibre. DAS sensitivity to plane P-waves decays as squared cosine of the incidence angle between the directions of the fibre and wave propagation (Kuvshinov 2016). This directional sensitivity is the main limitation of DAS. However, the main advantage of DAS is that we can have 3D VSP data for the entire depth of the well, which I utilise in this study.

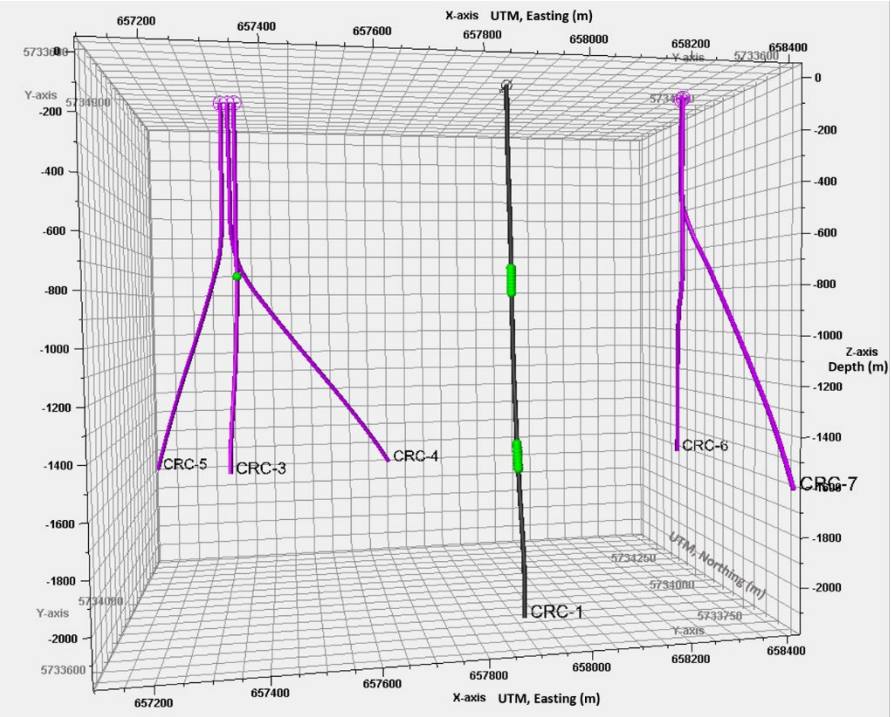

Figure 5-1 Position of wells instrumented for 3D VSP measurements. Purple lines indicate DAS cables covering five wells in Stage 3. Green dots – position of geophones in the CRC-1 and CRC-3 wells of 3D VSP surveys acquired during Stages 1 and 2C at Otway site. View from south-west.

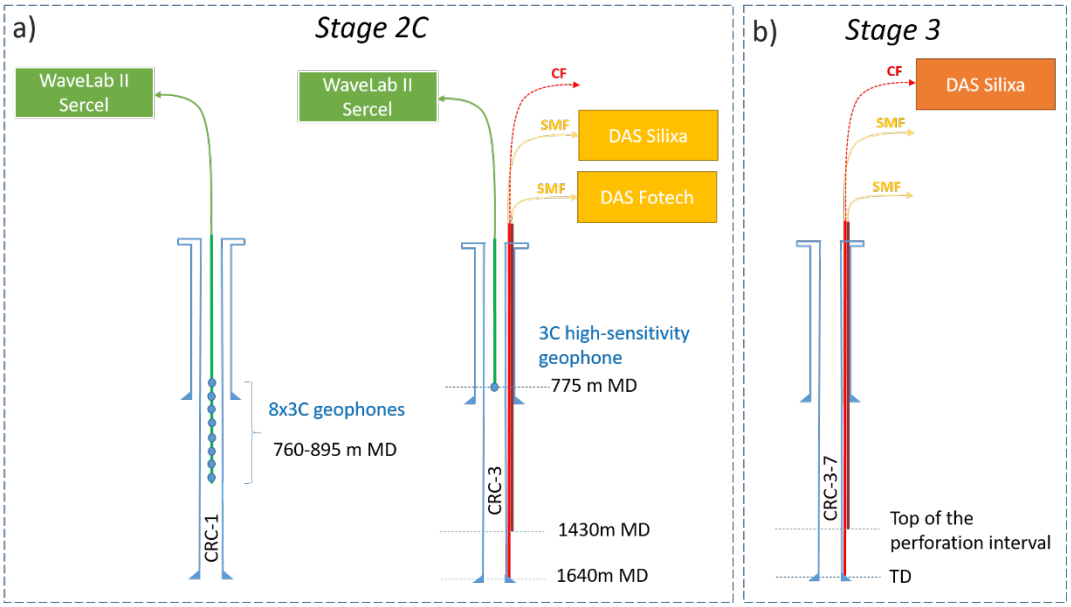

Figure 5-2 Schematic of the VSP receivers in the observation wells CRC-1 and CRC-3 for the M5 3D VSP survey acquired for Stage 2C (a); VSP DAS receiver configuration in the CRC-3, CRC-4, CRC-5, CRC-6 and CRC-7 wells for the BL 3D VSP survey acquired during Stage 3 (b).

Table 5-1 Stage 2C and Stage 3 DAS acquisition parameters.

Survey	**Stage 2C M5**	**Stage 3 BL**
Date	Feb-18 - Mar-18	Mar-20 - Apr-20
Wells	CRC-3	CRC-3, CRC-4, CRC-5, CRC-6, CRC-7
Type of fibre	Single-mode	Constellation
DAS interrogator	iDAS v2, Fotech Helios Theta	3 x iDAS v3
Source line spacing	~50-100 m	~100 m
Source step	15 m	
Number of source positions	4738	4084
Survey area (source distribution, km^2)	7.3	7.3

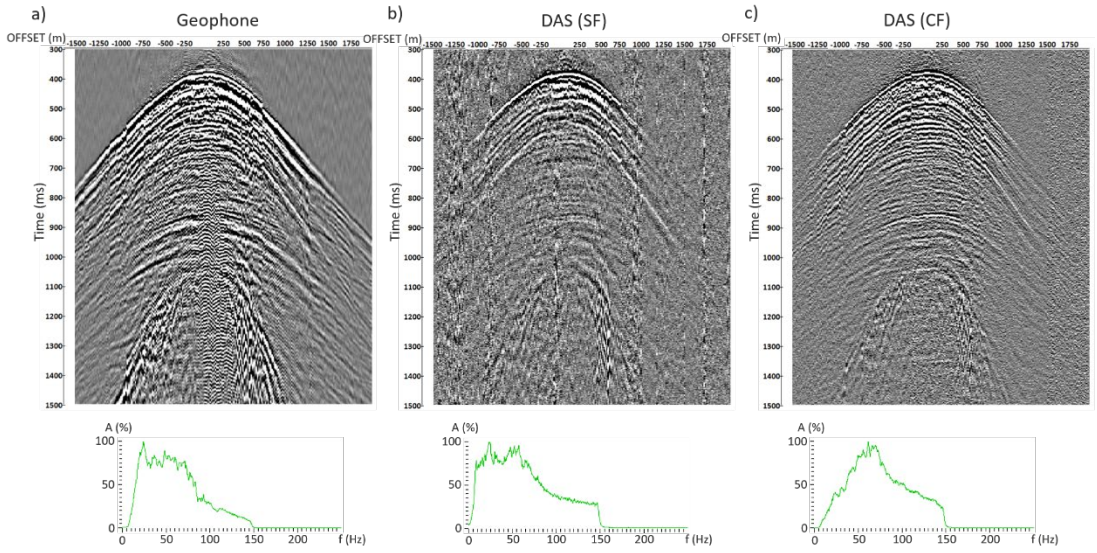

Figure 5-3 Comparison of geophone and DAS VSP common receiver gather. The CRC-3 well at a 775 m depth. a – geophone data; b – standard fibre data utilised in the Stage 2C; c – engineered fibre utilised in the Stage 3. Bottom graphs represent amplitude spectra taken from presented seismic gathers (time window between 300 and 1500 ms).

5.2 Travel-time analysis of P-wave direct arrival

In order to investigate the degree of elastic anisotropy, I computed time difference between observed (picked) P-wave travel times and those theoretically calculated using ray tracing for isotropic 1D media.

The interval velocities for estimation of the theoretical direct wave arrival times were taken from zero-offset VSP surveys covering the entire depth of the CRC-1 and CRC-3 wells. CRC-1 zero-offset VSP data were acquired with a geophone string while CRC-3 was covered with DAS. Interval velocities were estimated between the positions of adjacent receivers (15 m receiver spacing in case of geophones and 5 m binning step in case of DAS). The obtained velocity function was smoothed in a 3- and 5-sample window for DAS and geophones, respectively, in order to eliminate first-break picking and random noise errors.

The original acquisition sampling interval of both DAS and geophone VSP data was 1 ms. Prior to picking the first arrivals, 3D data were resampled from 1 ms to 0.1 ms in order to obtain a more precise timestamp of the first wiggle peak. Data were picked in auto-fill mode and visual quality control was implemented afterwards with manual corrections. Using this approach, the error is expected to be below 0.5 ms.

The maximum variation in the surface elevation of different sources in the 3D survey is about 43 m. In order to eliminate the effect of the elevation variation on the travel-time curves, I took into account source elevation statics by bringing first-arrival times to the flat datum 30 m above the sea level with replacement velocity taken from surface seismic data and equal to 1800 m/s. In the following sections we will show how the picked travel times differ from the theoretical ones based on raytracing for both geophones and DAS data.

5.2.1 Geophone data

The time-difference map computed from the geophone data (vertical component) in the CRC-1 well at a depth of 760 m is shown in Figure 5-4a. Please note that the travel-time misfit values are plotted at the location of each source position with no interpolation implemented. For a laterally homogeneous isotropic medium with correct interval velocity there should not be any difference in travel times. In a laterally homogeneous VTI medium, the travel-time pattern should be circular. Yet the map shows strong ellipticity of the travel times, and hence significant deviation of the

observed data from azimuthally isotropic model – the data shows strong azimuthal anisotropy. In order to start characterisation of such anisotropy, I have extracted two symmetry axes from this map: one of the axes represents the slow direction of wave propagation (the time difference is higher), while the other axis coincides with the fast direction. A similar pattern is observed for other geophone receivers in CRC-1 (from 760 m to 895 m MD) and in CRC-3 (at 775 m MD) (Figure 5-5a). This behaviour of the travel times could be related to the local stress field, which coincides with the fast direction of the wave propagation. Moreover, on a more local scale, this azimuthal dependence is well correlated to the local fault direction, as indicated by Figure 5-4b that shows the RMS amplitude of the time-lapse surface seismic signal between the BL survey and M5, acquired two years after injection of the supercritical CO_2. The RMS amplitude was computed within a 24 ms rectangular window centred at the injection level. The plume appears to be spreading from the CRC-2 injector well along the fast direction, which suggests that the seismic anisotropy may be stress-induced.

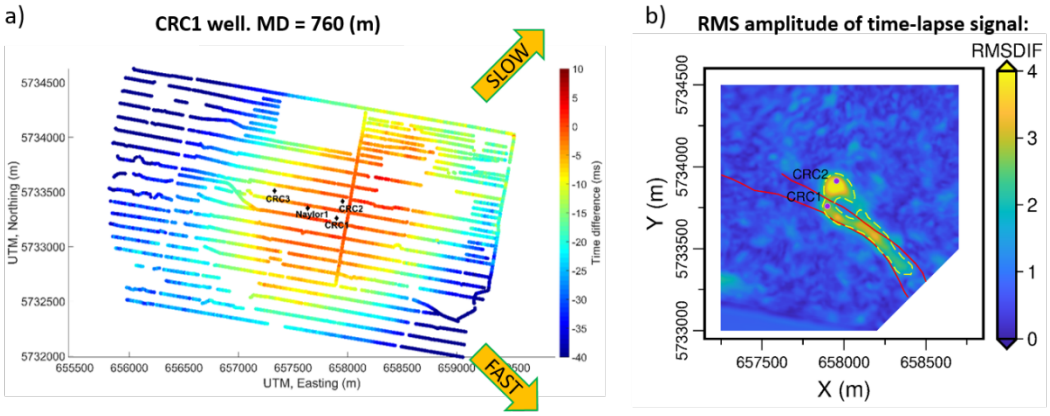

Figure 5-4 a – map of the differences between observed travel times and those estimated from an isotropic model for geophone CRC-1 data at a depth 760 m. b – plume evolution caused by the injection of CO_2-rich gas after the 5th monitor survey (M5) shown as an RMS amplitude of time-lapse signal (computed in a 24 ms time window centred at injection level). Red solid lines show the locations of the faults. Yellow dashed line contours the M5 plume (the same contour as shown in Figure 4-7).

5.2.2 DAS data

In addition to geophone travel times in CRC-1 and CRC-3, I also analysed travel-time misfit maps obtained from the DAS data for the entire length of the CRC-3 well. As noted above and observed from Figure 5-3, DAS does not allow travel times

to be obtained for far offsets. Figure 5-5 shows travel-time misfit maps for geophone (a) and DAS (b) data at the same depth (775 m) in the CRC-3 well. Grey points on the DAS map represent the far offset area that cannot be picked due to DAS insensitivity in detecting arrivals coming under large incidence angles. However, arrivals at 1 km offset at a depth of 775 m are still strong enough to track the elliptic misfit trend.

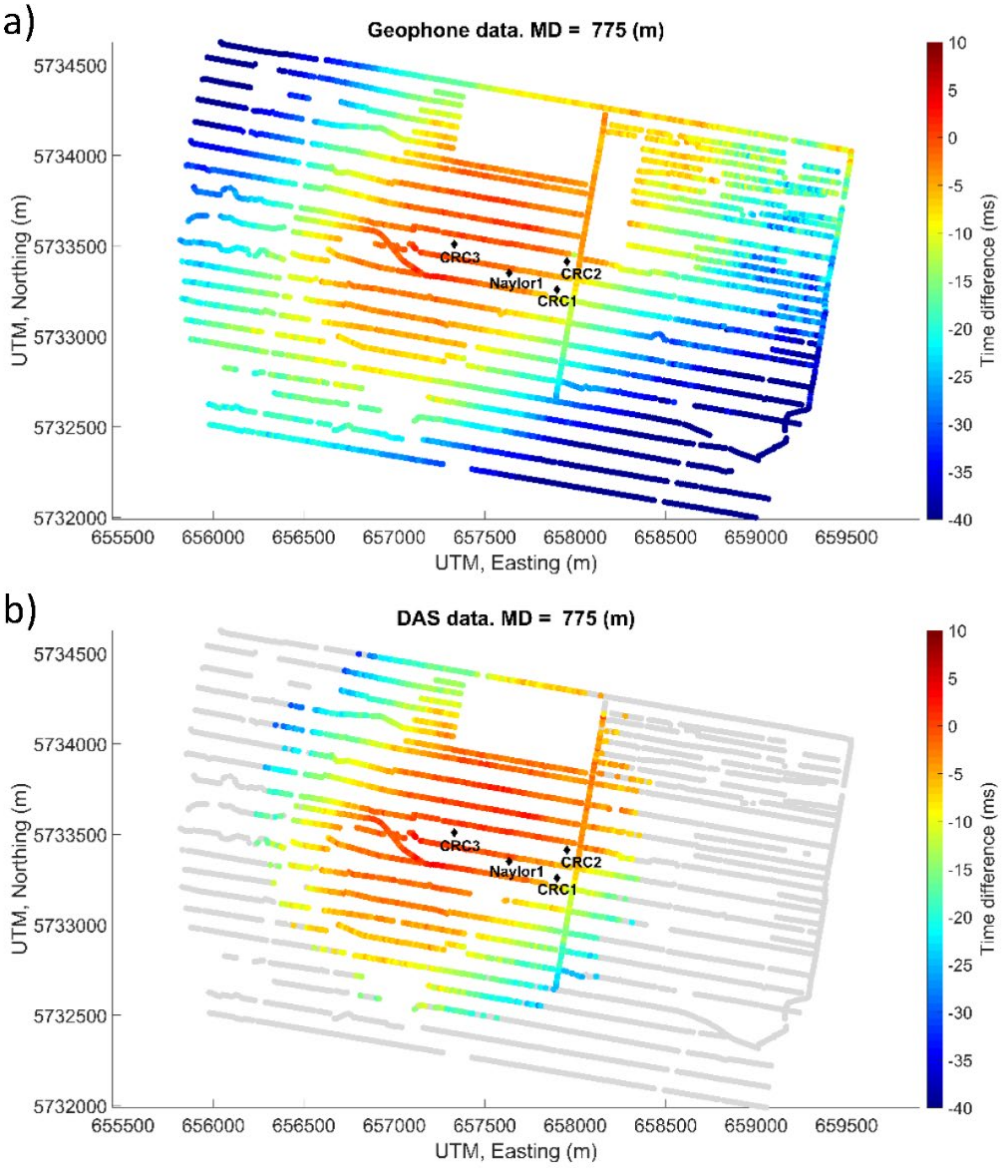

Figure 5-5 Maps of the differences between observed travel times and those estimated from an isotropic model for geophone data (a) and DAS data (b) in the CRC-3 well at a depth of 775 m.

Analysis of the misfit maps for other depths using DAS data demonstrates that the anisotropy characteristic changes with depth. Figure 5-6a shows such a map at a depth of 295 m. No azimuthal variations can be observed at this depth level. However,

the misfit map at a depth level of 1435 m (Figure 5-6b) shows a strong azimuthal variation of travel times. Analysis of such maps for the entire length of the CRC-3 well with 5 m spacing shows that below the depth ~600 m the azimuthal anisotropy increases sharply, showing an elliptic trend of the P-wave direct arrivals with the fast azimuth direction of ~140º.

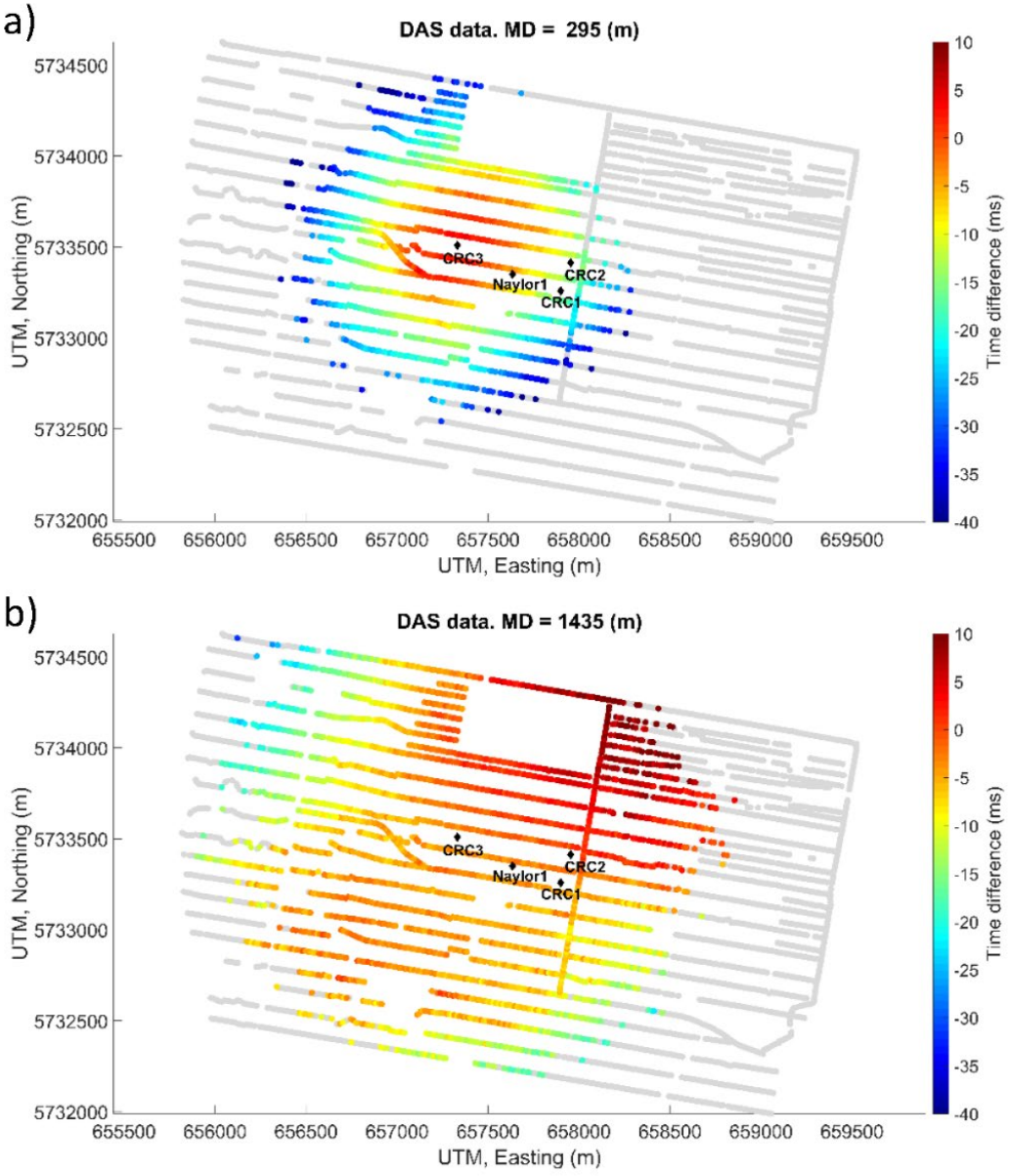

Figure 5-6 Map of the difference between observed travel times and those estimated from an isotropic model for DAS data in the CRC-3 well at a depth of 295 m (a) and at a depth of 1435 m (b).

Further analysis of Stage 3 multi-well 3D DAS VSP data shows a similar pattern obtained at other well locations (Figure 5-7). This confirms that the anisotropic

behaviour is similar at different locations and that the misfit travel-time distribution is not related to the lateral variation of the velocity field.

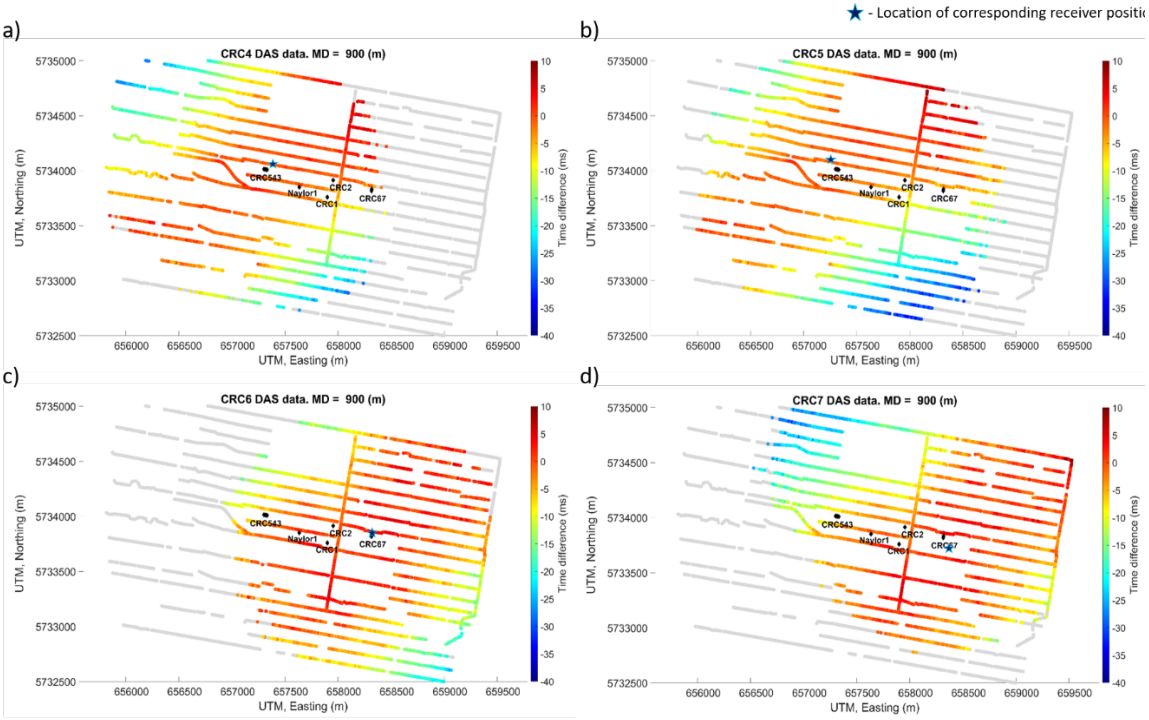

Figure 5-7 Maps of the difference between observed travel times and those estimated from an isotropic model for DAS data in the CRC-4 well (a), CRC-5 well (b), CRC-6 well (c) and CRC-7 well (d) at a depth of 900 m.

5.3 Local anisotropy parameters estimation using slowness method

In addition to azimuthal anisotropy, the Otway site is known to exhibit polar anisotropy (Pevzner et al. 2010; 2011; Asgharzadeh et al. 2013), and hence the medium can be considered as at least orthorhombic. Such anisotropy can be described along the symmetry axes by parameters analogous to VTI media (Tsvankin 2001). In this part, I utilise two approaches for anisotropy estimation. In the first approach I select two orthogonal anisotropic planes along the fast and slow directions and compute VTI parameters in each of the planes. Another approach include estimation of P-wave anisotropy as single orthorhombic media.

Both approaches utilise the slowness method discussed in Chapter 2.4. The reason behind choosing this method is because DAS measurements do not include

polarisations. Both methods are based of fitting of P-wave travel-time equations into a number of observed P-wave travel times.

5.3.1 Approximation of an orthorhombic medium by two VTI media

To test applicability of this approach, I only utilise geophone data in the CRC-1 well at a depth level 760 m. The reason to test the method on geophone data is because these data provide the most spatial coverage and best quality travel-time picks.

Figure 5-4 - Figure 5-7 demonstrated significant azimuthal variations of travel-time field. In order to see the difference in the variations between certain azimuthal ranges, we binned the data into a 30-degree azimuthal ranges (centred at the min and max travel-time differences) and plotted the same values of travel-time misfit as a function of offset. Figure 5-8 shows the distribution of the difference between the observed VSP direct arrival times and the times calculated with an assumption that the media is isotropic as a function of offset using two approaches: a – isotropic NMO travel-time equation, b – isotropic ray-tracing. Different colours represent different azimuth range binned with 30-degree spacing. As expected, ray-tracing approach using interval velocities provides much better approximation for the far offsets compared to travel times calculated from NMO-velocities (Figure 5-8).

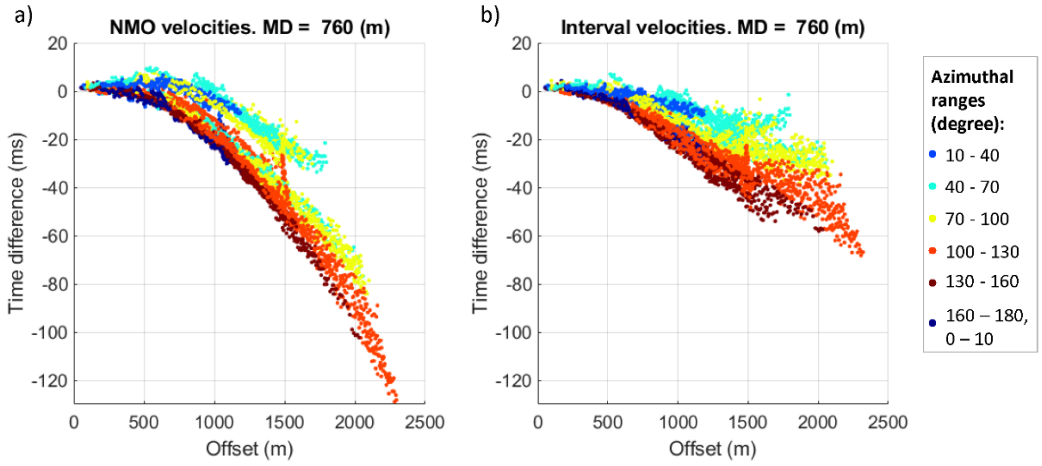

Figure 5-8 Difference between observed and estimated travel times using isotropic layered velocity model for the CRC-1 well calculated using: a – NMO-velocities and b – interval velocities (ray-tracing approach). Different colors on plots correspond to different azimuthal ranges.

Two perpendicular azimuthal directions with significantly different anisotropy values can be extracted from these plots: slow direction ~40 – 70 degrees and fast direction ~130 – 160 degrees, which matches to the previously reported results and observed directions of the horizontal stresses (Pevzner et al. 2010). Anisotropy properties in slow direction are much weaker compared to the fast direction.

Two directions that would correspond to the symmetry axes are the fast and slow directions. To compute the slownesses for these directions I binned the first breaks into 30-degree-wide azimuth sectors cantered at 55 degrees and 145 degrees (slow direction 40 – 70 degrees; fast direction 130 – 160 degrees). The first breaks from each of the two azimuth sectors were approximated by a VTI model with individual set of parameters. Equation for the slowness method proposed by Miller and Spencer (1994) for VTI anisotropy was used for estimation of the VTI anisotropy parameters. The reason of choosing this equation was that Asgharzadeh et al. (2013) deemed it least prone to errors among the VTI estimation methods they examined previously at the Otway site. The equation includes horizontal (p) and vertical (q) slownesses and four density-normalised components of the stiffness tensor (a_{11}, a_{13}, a_{13}, a_{55}):

$$a_{11}a_{55}p^4 + (-a_{11} - a_{55} + Aq^2)p^2 + a_{33}(a_{55}q^4 - q^2) + 1 - a_{55}q^2 = 0 \quad (23)$$

where

$$A = a_{11}a_{33} + a_{55}^2 - (a_{13} + a_{55})^2 \quad (24)$$

The slownesses that are needed in equations (23) and (24) were estimated from the direct-wave arrival times and are shown in Figure 5-9 for slow and fast directions as red circles. Four density-normalised moduli (a_{ij}) were determined by solving the inverse problem using initial parameters ($a0_{ij}$) and measured phase slownesses (p and q). The slownesses were computed from numerical derivatives of the travel time with respect to the source-receiver locations. The use of the horizontal slowness computed this way assumes that the horizontal slowness (ray parameter) does not change along the ray. This assumption is justifiable by the horizontally homogeneous nature of the local geology (Figure 5-7). Initial parameters for inversion were calculated for isotropic approximation of our media from V_p and V_s values taken from zero-offset VSP data for a receiver depth MD 760 m.

The density-normalised moduli provide a best fit for a set of measured slownesses (blue dots in Figure 5-9). Considerable similarity between the observed and modelled slownesses suggests reliability of the obtained anisotropy moduli. Figure 5-9 also shows inverted density-normalised moduli for slow and fast directions and the VTI parameters ε and δ calculated from these moduli.

Proposed approach of approximation of the media by two VTI planes provided good results. However, this approach has not been implemented as it utilises only the travel times along the main symmetry axes. In order to get better statistics and fit for all azimuths, we decided to implement an algorithm that uses all data and is discussed in the next section. This is also the reason we used only the geophone data, unlike the method in the next section that was used also on DAS data. The next step was to find and examine a P-wave anisotropic orthorhombic equation that utilise fitting of all the values into the whole range of the observed travel times.

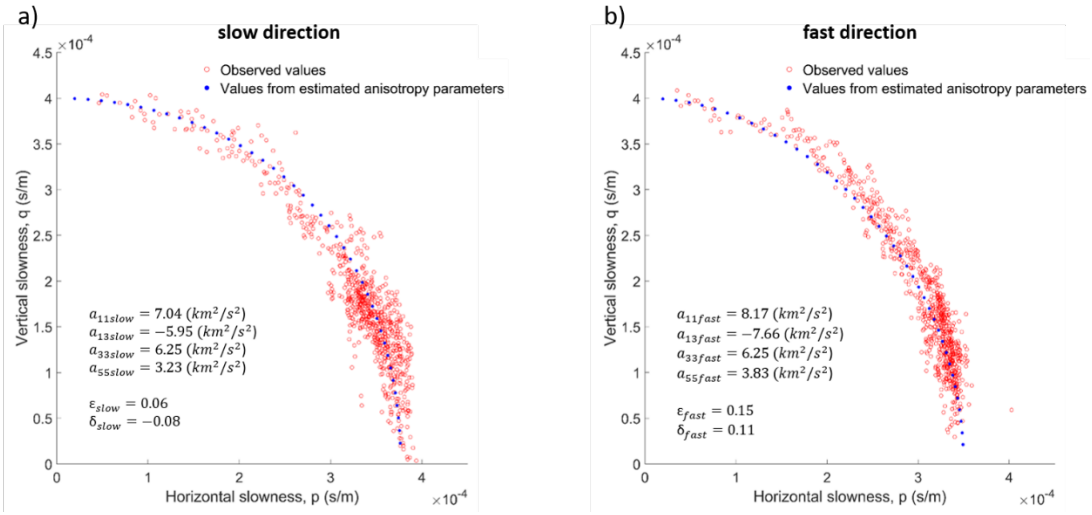

Figure 5-9 Red circles – vertical slowness component plotted against horizontal slowness component for P-waves from 3D VSP data for slow (a) and fast (b) directions at well CRC-1 for MD 760 m. Estimated anisotropy moduli for both cases are depicted. Blue dots - result of the inverse problem solution with obtained density-normalised parameters.

5.3.2 Orthorhombic media approximation

There are a few equations and approaches to describe orthorhombic anisotropy. Among all the methods, it was decided to parametrise the media as orthorhombic using the approach proposed by Alkhalifah (2003). The choice of this particular equation was because it utilises slownesses method and requires only P-waves for parameter

estimation. In this section I utilise Stage 2C 3D VSP data: CRC-3 with DAS and CRC-1 with a downhole geophone string.

The Alkhalifah (2003) equation (25) describes analytical dispersion relation between slowness vector $p = p(x,y,z)$ and anisotropy parameters:

$$p_z^2 = \frac{1 - p_y^2 V_2^2 - p_x^2 V_1^2 (1 + p_y^2(\gamma^2 v_1^2 - v_2^2 + 2\gamma^2 v_1^2 \eta_1 - 2v_2^2 \eta_2))}{v_v^2 (1 - 2p_y^2 v_2^2 \eta_2 - p_x^2 v_1^2 (2\eta_1 + p_y^2(\gamma^2 v_1^2 (1 + 4\eta_1) - 2\gamma \frac{V_1}{v_1} v_2 + v_2^2 (1 - 4\eta_1 \eta_1))))} \quad (25)$$

where the horizontal velocity in x_1 direction is

$$V_1 = v_1 \sqrt{1 + 2\eta_1}, \quad (26)$$

the horizontal velocity in x_2 direction is

$$V_2 = v_2 \sqrt{1 + 2\eta_2}, \quad (27)$$

and

$$\gamma = \sqrt{1 + 2\delta}. \quad (28)$$

where v_v is P-wave vertical velocity, v_1 and v_2 are NMO P-wave velocity for horizontal reflectors in the [x_1, x_3] and [x_2, x_3] planes, respectively, η_1 and η_2 are anellipticity in the [x_1, x_3] and [x_2, x_3] planes, respectively, δ is Thomsen's parameter in the [x_1, x_2] plane. x_1, x_2 and x_3 planes are related to the symmetry axes that correspond to the fast and slow directions of the velocities and tilt of the polar axis, respectively.

The algorithm of inverting for anisotropy parameters is analogous to the VTI approach described in the previous section: all the parameters were obtained by non-linear fitting of unknown anisotropy parameters into observed slowness vector using orthorhombic equation (25).

The resulted inverted parameters obtained from DAS CRC-3 data are shown on Figure 5-10. Analysis of DAS results demonstrates significant changes (up to 600 m/s) in horizontal velocities between slow and fast directions observed for the depth range between 600 – 1100 m (Figure 5-10b). However, horizontal velocities do not split much for the shallow part of the section which indicates the absence of orthorhombic anisotropy in this section.

Figure 5-11 shows the comparison of CRC-3 DAS results and CRC-1 geophone results. Inverted parameters estimated from the DAS data in the CRC-3 well and from the geophone data in the CRC-1 well matches perfectly for the fast direction.

Slow direction gives slightly different results, which would indicate a lateral change of the anisotropy.

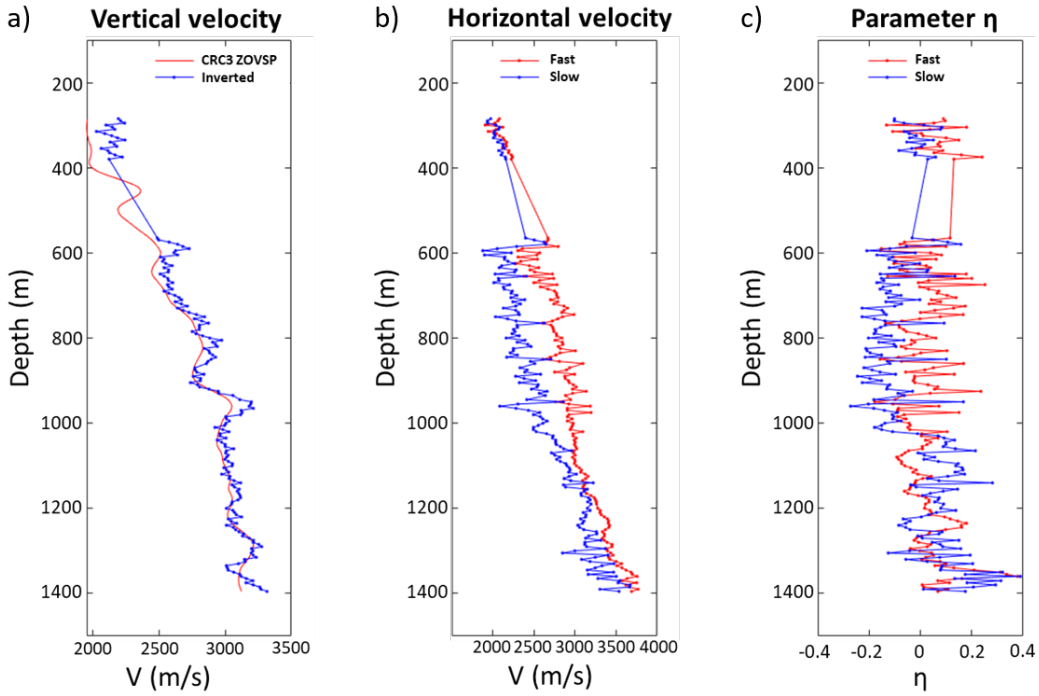

Figure 5-10 Inverted parameters from Stage 2C DAS data in the CRC-3 well. a – vertical velocity estimated from zero-offset VSP and inverted vertical velocity; b – horizontal velocity in fast and slow directions; c – anellipticity in fast and slow directions.

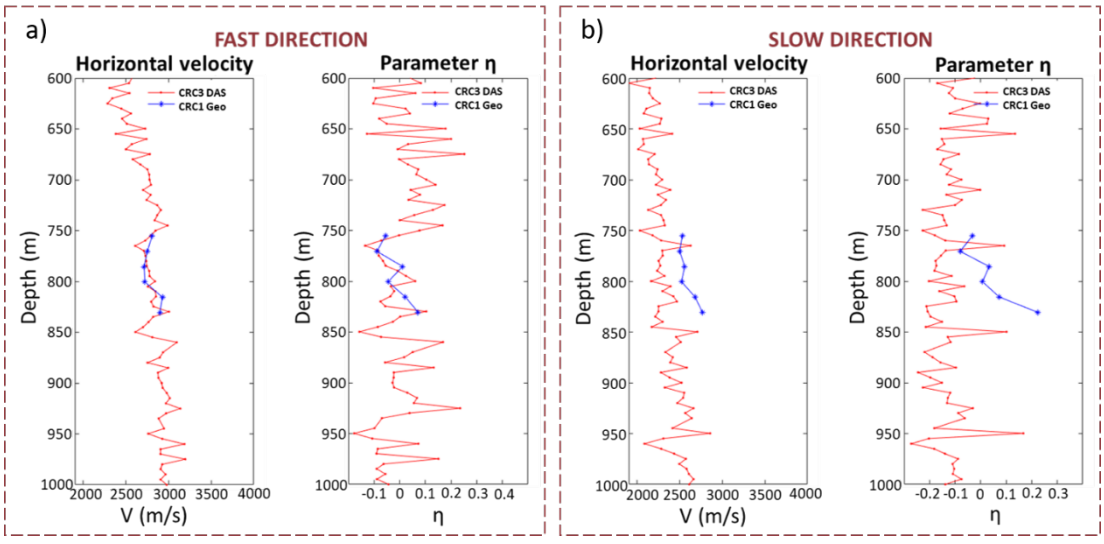

Figure 5-11 Comparison between CRC-1 (geophone) and CRC-3 (DAS) inverted results for fast (a) and slow (b) directions.

Inverted anisotropic parameters were substituted into the equation (25) in order to estimate slowness vector and compare it to observed slowness vector. This process show reliability of the obtained anisotropic values. Figure 5-12 shows the result of the fit of the estimated values to the field data at one depth location for geophone data in the CRC-1 well. A good match is observed and the approach for estimation of anisotropy seems to be reliable.

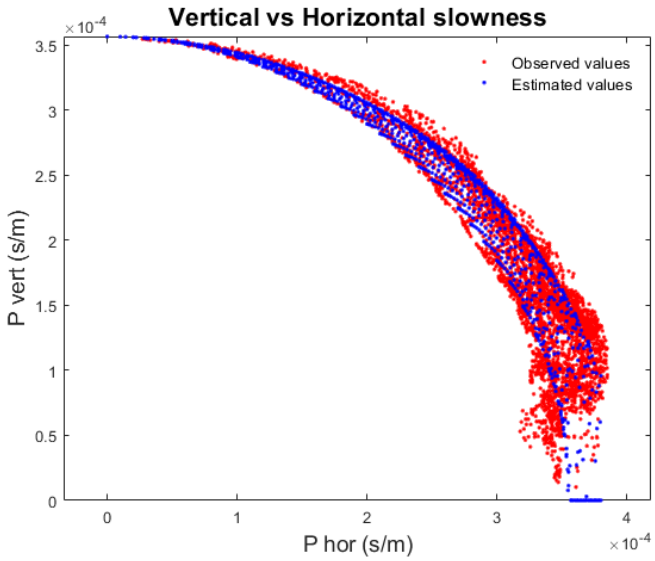

Figure 5-12 Quality control of the fit of the estimated slownesses from inverted results to the observed slownesses.

The approach to estimate local anisotropy parameters from orthorhombic equation provided stable and geologically meaningful results. However, it is still not obvious how to implement this equation into imaging using commercially available software that normally deals only with VTI media.

5.4 Effective anisotropic orthorhombic NMO-velocity approximation

We conducted a several attempts to represent the media as a set of local anisotropy parameters. These approaches provided good estimates. However, the local nature of the parameters makes it not straightforward to be utilised in imaging. The next step was to find effective anisotropic orthorhombic NMO-velocity approximation that would give us a good parametrisation of the travel-time field.

This section describes approach to represent effective anisotropic media. In this part I analyse all existing 3D VSP datasets, including Stage 3 multi-well 3D DAS VSP.

5.4.1 Approximation of travel times and inversion process

As was described in above sections, the observed velocities change with dip and azimuth. To describe travel times in such a medium, I combine the elliptical approximation proposed by Corrigan et al. (1996) to describe azimuthal anisotropy

$$t^2\,(r,\varphi) = t_0^2 + \frac{r^2}{V_{nmo}^2}[1 - \sigma cos2(\varphi - \omega)] \tag{29}$$

with Alkhalifah and Tsvankin (1995) approximation for VTI media to describe polar anisotropy

$$t^2(r) = t_0^2 + \frac{r^2}{V_{nmo}^2} - \frac{2\eta r^4}{V_{nmo}^2[t_0^2 V_{nmo}^2 + (1+2\eta)r^2]} \tag{30}$$

where t_0 is zero-offset P-wave travel time, r is source-receiver offset, V_{nmo} is NMO velocity, σ is azimuthal velocity ellipticity, φ is shot-receiver azimuth, ω is fast velocity azimuth, and η is polar anellipticity, which can be written utilising Thomsen's anisotropy parameters as

$$\eta = \frac{\varepsilon - \delta}{1 + 2\delta}. \tag{31}$$

The combined travel-time approximation for azimuthally and polarly anisotropic media is given by the following expression:

$$t^2(r,\varphi) = t_0^2 + K(\varphi)\frac{r^2}{V_{nmo}^2} - \frac{2\eta r^4}{\frac{V_{nmo}^2}{K(\varphi)}[t_0^2\frac{V_{nmo}^2}{K(\varphi)} + (1+2\eta)r^2]} \tag{32}$$

where

$$K(\varphi) = 1 - \sigma cos2(\varphi - \omega). \tag{33}$$

The anisotropy parameters in the above expression were estimated by non-linear fitting of the observed travel times to the theoretical predictions for each depth level of the VSP measurements. Inversion was conducted using the fmincon 'interior-point' algorithm in MATLAB (Optimisation Toolbox). This algorithm implements minimisation of the constrained nonlinear multivariable function.

The known input data for inversion are observed travel times, offset and shot-receiver azimuth corresponding to each pair of seismic source and receiver. All five other parameters - namely zero-offset travel time, NMO velocity, velocity ellipticity, azimuth of fast velocity direction and anellipticity - were inverted for. The initial values of the zero-offset travel time and NMO velocity were taken from the isotropic analysis, while magnitude and azimuth of anisotropy were taken from geological

information and previous studies (Berard et al. 2008; Pevzner et al. 2010). The constraints (the lower and upper bounds of the inversion searching range) used in this study for each parameter are specified in Table 5-2.

Table 5-2 Constraints utilised in the inversion process for the whole range of depths.

	Lower bound	**Upper bound**
T0	0 ms	800 ms
NMO velocity	1500 m/s	2500 m/s
Azimuthal ellipticity	0	0.1
Fast velocity azimuth	90 degree	180 degree
Polar anellipticity	0	0.5

5.4.2 Inverted parameters

Figure 5-13 shows the inverted parameters. The green lines represent results from geophone data from the CRC-1 well. The analysis for the bottom part of the well was based on Stage 1 3D VSP survey that had a different acquisition pattern. The blue dot at 775 m is an estimate from a single geophone in the CRC-3 well. Red lines represent the result from the DAS 3D VSP in the CRC-3 well. A dashed area between the measurements within an interval between 400 m and 600 m is due to interference of the P-wave first arrival with a series of strong reflections at this level, as here the first arrivals could not be picked accurately.

The results from the geophone and DAS data are consistent with each other. At depths of 760 to 895 m, the estimates in the CRC-1 and CRC-3 wells are close. In both wells, the NMO velocity is monotonically increasing with depth. The magnitude of the azimuthal anisotropy increases significantly with depth: it is relatively weak in the shallow section (above 600 m) and steeply increases below.

Polar (vertical-plane) anellipticity remains almost constant at 0.1. The azimuth of the fast direction varies with depth by about 10 degrees, from 150º azimuth in a shallow section to 140º azimuth at a depth of 1400 m.

Figure 5-14 represents results from Stage 3 multi-well 3D VSP data acquired with DAS in five wells plotted on a same plot. Due to interference of the P-wave first arrival with a series of strong reflections at the level between 420 m and 550 m

(between dashed lines), first arrivals could not be picked accurately. Thus, this area does not show reliable estimates.

Results obtained for different wells show quite similar trends. However, some variations of parameters between the wells take place which most probably indicates lateral variation in velocity and anisotropy fields. Figure 5-15 represents the same inverted values in 3D view.

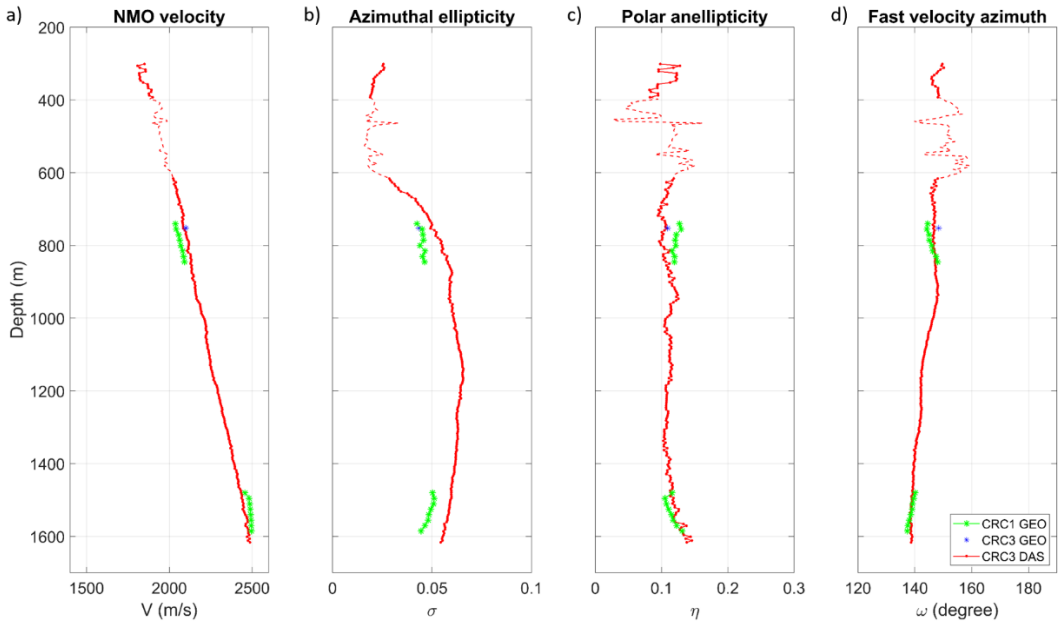

Figure 5-13 Inverted anisotropy parameters from DAS and geophone 3D VSP data. a – NMO velocity; b – azimuthal ellipticity; c – polar anellipticity; d – fast velocity azimuth. Red curves show the parameters obtained from DAS data from the CRC-3 well; the blue dot shows a single geophone from the CRC-3 well; green curves show the results from geophone data from the CRC-1 well (the analysis for the bottom part of the well was based on a previous 3D VSP survey that had a different acquisition pattern). The dashed area represents unreliable results due to the inability to track first arrivals at far offsets at these levels.

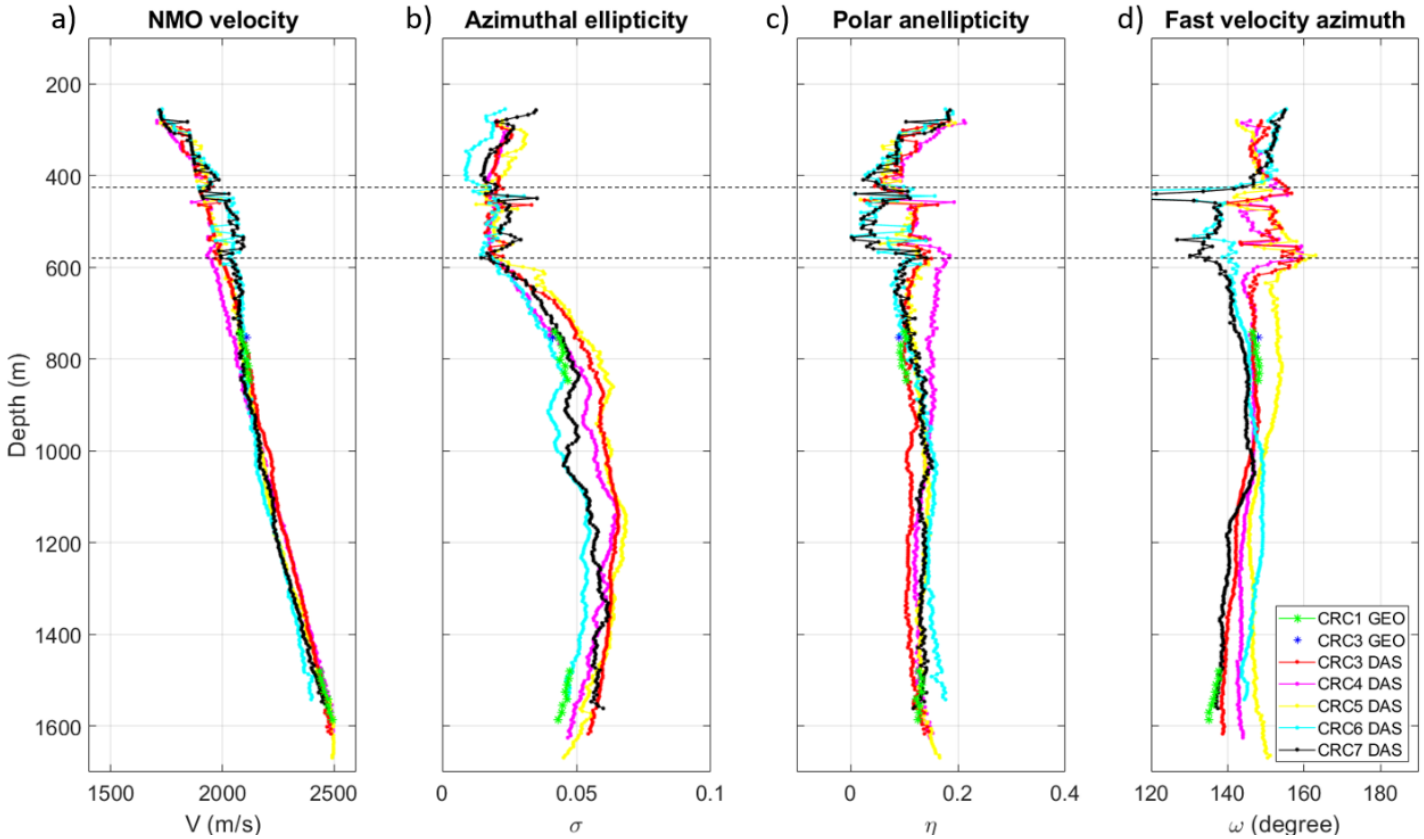

Figure 5-14 Inverted anisotropy parameters from five wells covered with 3D DAS VSP measurements and two wells with 3D VSP geophone measurements. a – NMO velocity; b – azimuthal ellipticity; c – polar anellipticity; d – fast velocity azimuth. Interval between two dashed lines provides unreliable results due to the inability to track first arrivals at these levels.

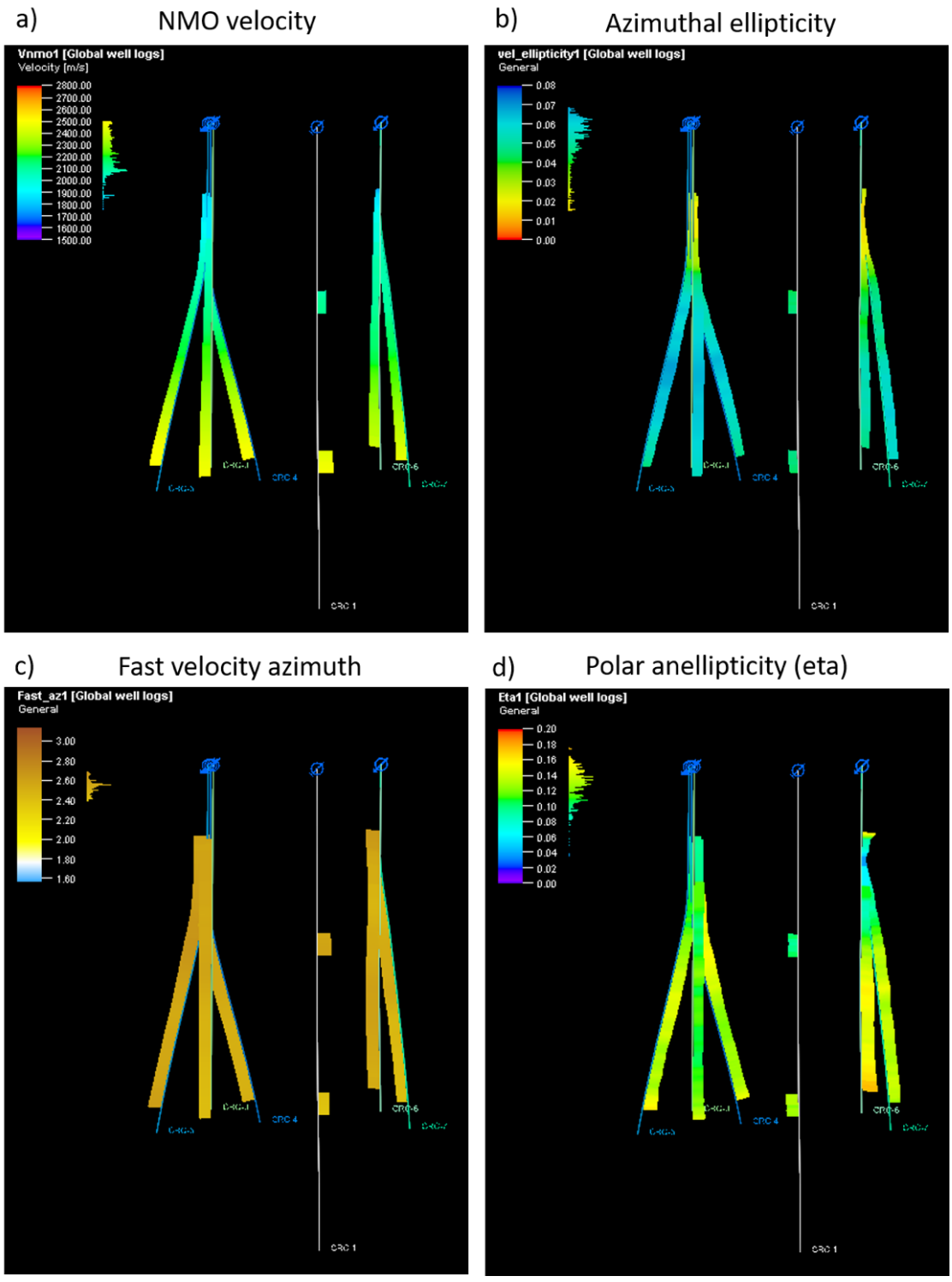

Figure 5-15 Inverted anisotropy parameters (Figure 5-14) from five wells covered with 3D DAS VSP measurements and two wells with 3D VSP geophone measurements represented in 3D. a – NMO velocity, b – azimuthal ellipticity, c – fast velocity azimuth, d – polar anellipticity.

5.4.3 Interpretation of effective anisotropy parameters

The results show that anellipticity in the vertical plane η is almost constant among the wells and along the well (Figure 5-13 and Figure 5-14); however, azimuthal variation of velocity is depth dependent. There is almost no azimuthal variation in travel times for the shallow part of the study area (above 600 m) and significant variations of velocities with azimuth below this level. This abrupt increase is correlated to the change of lithology at this depth – it corresponds precisely to the top of Wangerrip formation sandstones (Figure 3-2). The sharp increase of anisotropy at this interface may be related to a change in the geomechanical properties of rocks. Indeed, most rocks above Wangerrip are marls, which are rather plastic and thus have probably absorbed the anisotropic stress over geologic time. On the other hand, Wangerrip and deeper formations are much sandier and stiffer. Sandstones usually show the largest magnitudes of stress-induced azimuthal anisotropy as measured by cross-dipole shear logs (Pevzner, Gurevich, and Urosevic 2011; Sayers 2010). The variation in the magnitude of anisotropy with depth obtained from P-wave travel times in CRC-3 is qualitatively consistent with previous estimates of anisotropy from shear sonic and VSP data in CRC-1 (Pevzner, Gurevich, and Urosevic 2011).

Significant differences in azimuthal ellipticity in the bottom section between the CRC-1 and CRC-3 wells (Figure 5-13) most probably indicate lateral velocity variation, which could be caused by a number of faults affecting the Sherbrook supersequence (Figure 3-2).

Figure 5-16 shows an inline and a crossline surface seismic sections with interpreted major faults crossing the study area (shown as orange and purple surfaces). Figure 5-16a includes the CRC-3, CRC-4 and CRC-5 well paths. The orange fault crosses all three wells at different depths between 600 m and 800 m. This feature explains the presence of differences in resulted anisotropy parameters acquired from these wells (Figure 5-14). Figure 5-16b shows the CRC-6 and CRC-7 well paths. While the CRC-7 well has two faults in close proximity to the well, CRC-6 well sits away from these faults. Thus, the resulted parameters of fast velocity azimuth and velocity ellipticity provide significant differences in the wells CRC-6 and CRC-7 (Figure 5-14).

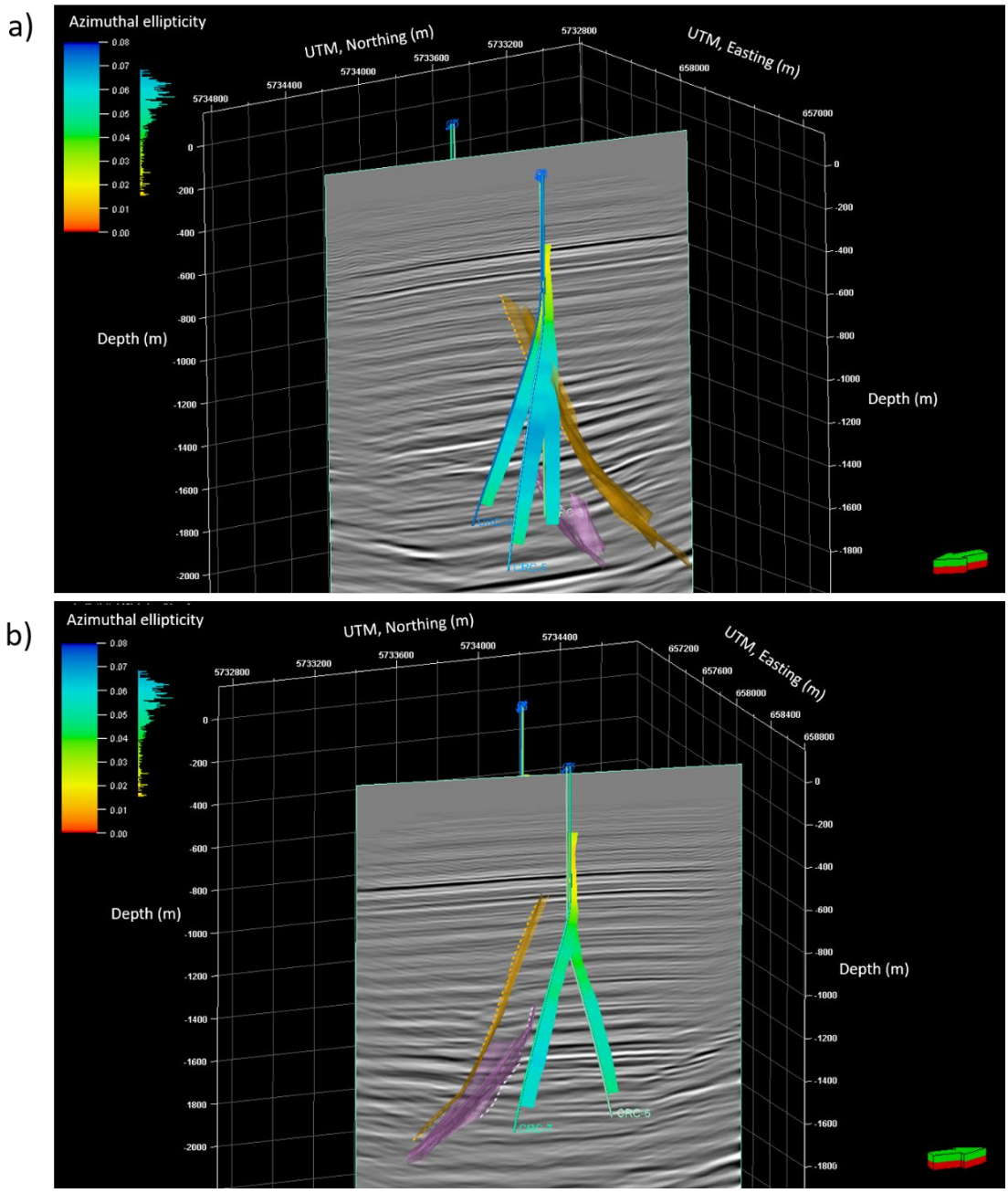

Figure 5-16 Surface seismic section, location of main seismic faults (orange and purple surfaces) interpreted from the surface seismic data, and the deviated well paths overlapped with the azimuthal ellipticity attribute. a – XL 170 and wells CRC-3, CRC-4 and CRC-5, b – XL 270 and wells CRC-6 and CRC-7.

South-eastern Australia exhibits a prevailing NW-SE pattern of the maximum horizontal stress (Sandiford, Wallace, and Coblentz 2004; Rajabi et al. 2017). Berard et al. (2008) calculated that maximum horizontal stress direction within the depth range 500–2100 m at the Otway site is about 141^0 from the north (clockwise). In addition, according to the SHINE application (http://shine.rm.ingv.it/index.phtml) that

estimates the maximum horizontal stress orientation of the present-day stress field for any point on the Earth's surface, the resulted maximum horizontal stress direction in the study area is 142^0 based to the World Stress Map Database Release 2016 (Heidbach et al. 2016). According to Figure 5-4, Figure 5-13 and Figure 5-14, the azimuthal variation of velocity coincides with the stress field in the study area (Figure 5-17).

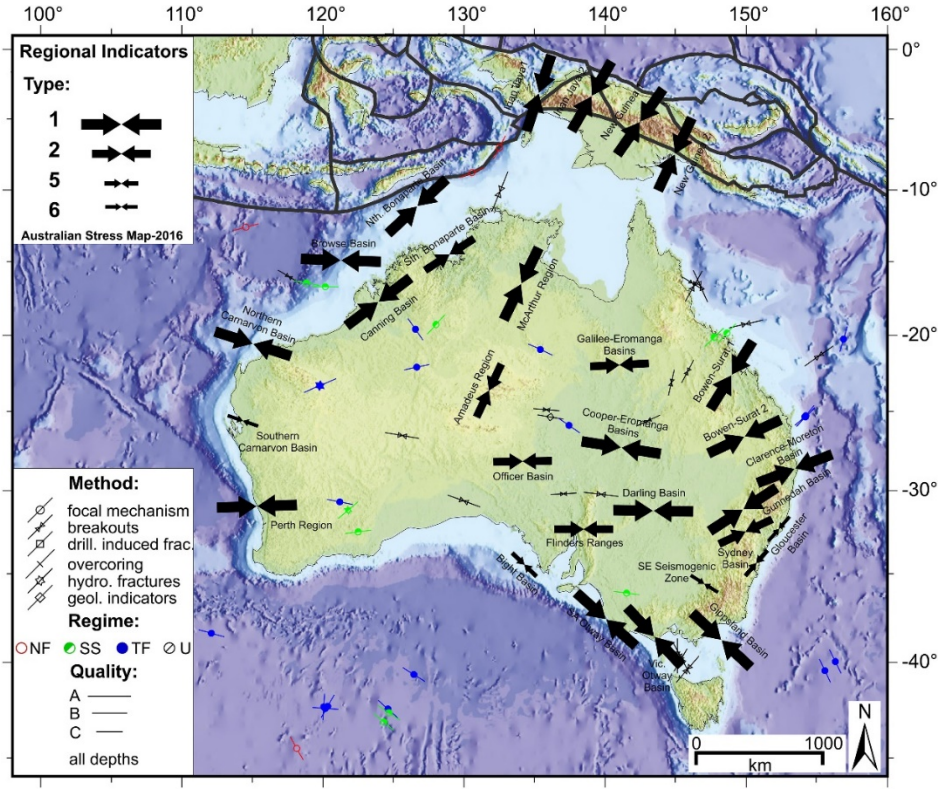

Figure 5-17 Australian stress map – 2016. Black arrows show the mean orientation of maximum horizontal stress across the Australian continent. Victorian Otway Basin in southeast of Australia corresponds to the location of the study area. Reproduced from Rajabi et al. (2017).

5.4.4 Estimation of uncertainties

Analysis of the misfit

In order to estimate the reliability of the obtained anisotropy parameters I computed the difference between the observed P-wave direct travel times and those computed with equation (32) using inverted anisotropy parameters. I also compare these results to other approaches, such as the isotropic NMO-equation, the NMO-equation for VTI media (30), and Corrigan et al. (1996) equation (29), which includes only azimuthal anisotropy. Figure 5-18 shows such time-difference plots versus offset

for different data sets: the geophone data in the CRC-1 well at depths 775 m (a) and 1500 m (b), and DAS data in the CRC-3 well at depths 775 m (c) and 1110 m (d). The results demonstrate significant improvement in fitting of the data when using the combined approximation compared to other approaches. However, as can be seen from Figure 5-18a, the long-offset geophone data was not fitted perfectly at far offsets. This is because we did not use the full range of offsets available for geophone data, we used only the same limited range that we used for DAS data in order to have a fair comparison between geophone and DAS estimates.

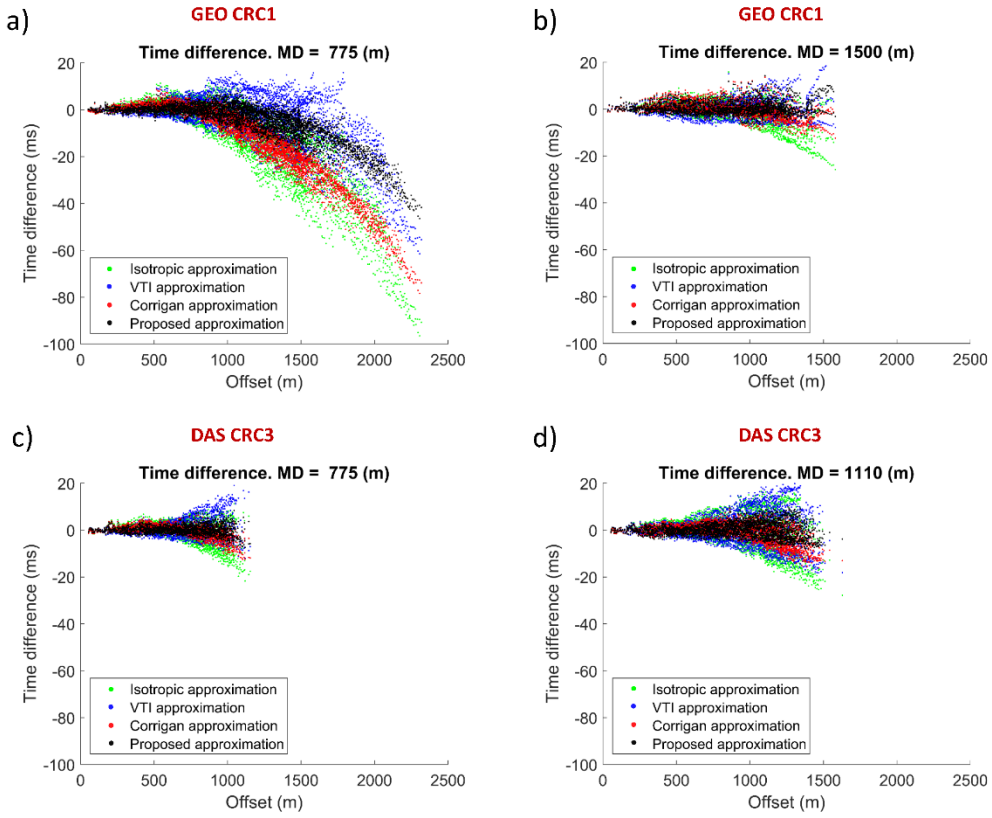

Figure 5-18 Time-difference between observed P-wave direct travel times and those calculated using different approaches: green – isotropic NMO-equation, blue – VTI NMO-equation, red – NMO-equation including azimuthal anisotropy only (Corrigan et al. (1996) approximation); and black – proposed approximation that includes both polar and azimuthal anisotropy. a – geophone data from CRC-1 at a 775 m depth; b – geophone data from CRC-1 at a 1500 m depth; c – DAS data from CRC-3 at a 775 m depth; d – DAS data from CRC-3 at a 1110 m depth.

Uncertainty with depth

Figure 5-19, Figure 5-20 and Figure 5-21 show distribution with offset and depth of RMS time difference between the observed and modelled travel times for DAS data in CRC-3 using isotropic, VTI and proposed approximations, respectively. The RMS travel-time misfit is computed within 25 m binned data along the offset domain for each depth level. The plots on the right provide the mean RMS travel-time misfit between observed and calculated travel times at each depth level. The figure demonstrates that the overall fit of the proposed approximation (32) that takes into account both polar and azimuthal variations of velocities is much better compare to VTI (30) and isotropic approximations and proofs the necessity to take into account both polar and azimuthal anisotropy.

Analysis of the colormap demonstrates that near offset and shallow depth areas give RMS time difference values around 0 ms, while the RMS travel-time misfit estimated for the deepest levels at far offsets provides a worse result of up to 4 ms value. This demonstrates that the quality of the far offset fit with proposed equation (32) at depths below 1000 m is inferior to those at shallower depths, which may indicate the presence of lateral variations or other factors leading to more complex travel-time approximation. Same trend is observed for isotropic and VTI fit, however, the RMS misfit value is much higher.

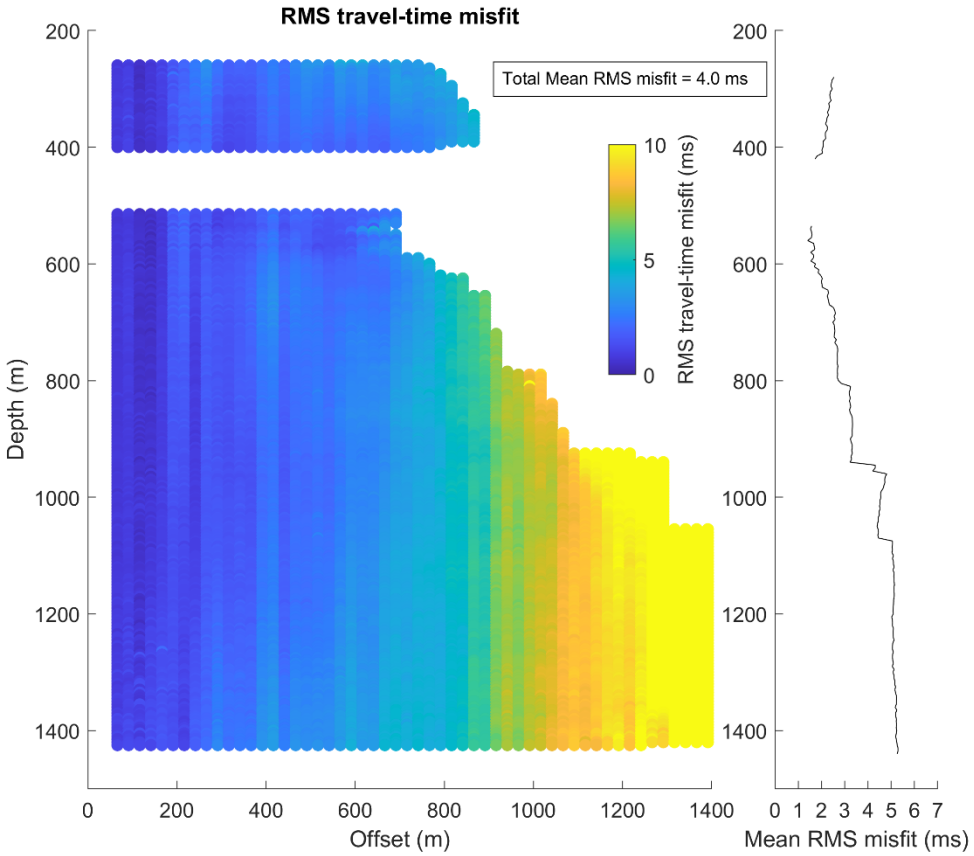

Figure 5-19. RMS time difference between observed travel times and those calculated using isotropic approximation from DAS data in CRC-3. Graphs on the right represent mean RMS travel-time misfit at each depth. Total mean RMS travel-time misfit is indicated in the box.

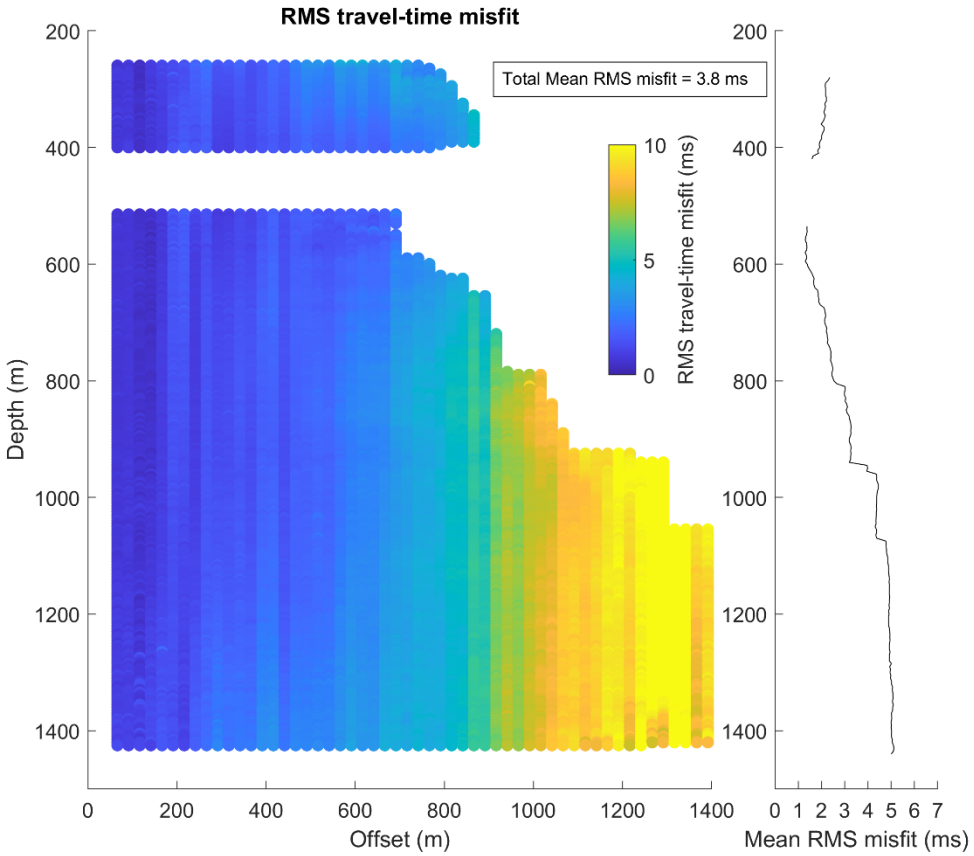

Figure 5-20 RMS time difference between observed travel times and those calculated using VTI approximation (30) from DAS data in CRC-3. Graphs on the right represent mean RMS travel-time misfit at each depth. Total mean RMS travel-time misfit is indicated in the box.

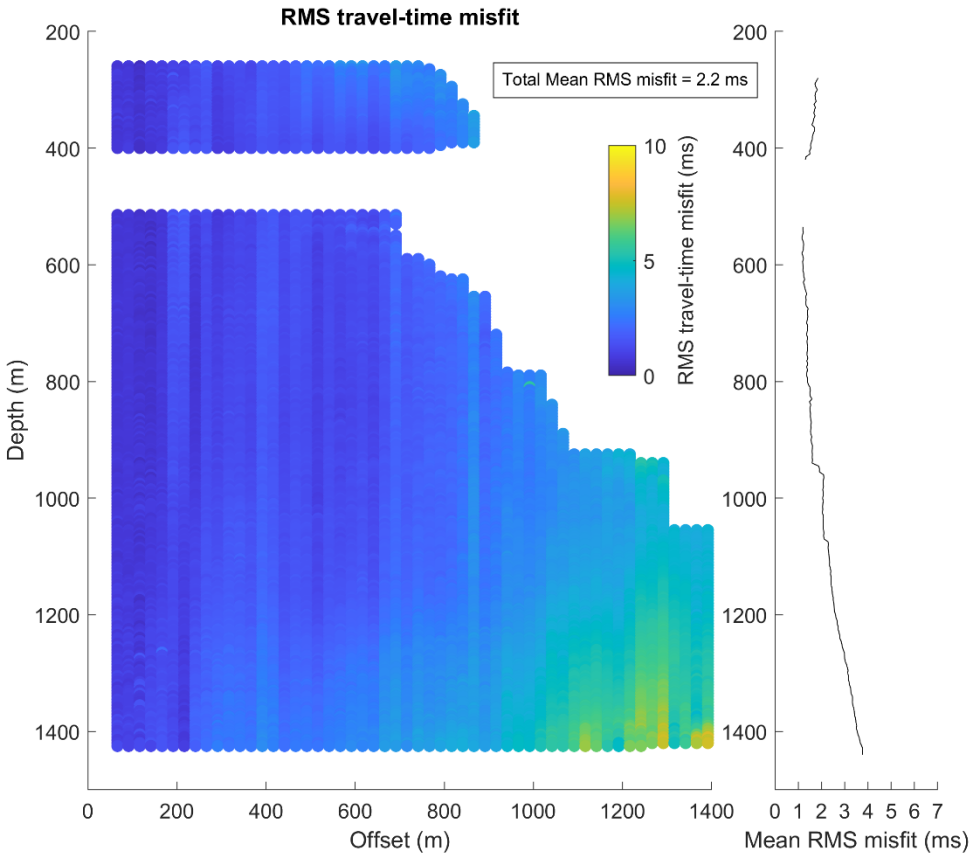

Figure 5-21 RMS time difference between observed travel times and those calculated using proposed equation (32) from DAS data in CRC-3. Graphs on the right represent mean RMS travel-time misfit at each depth. Total mean RMS travel-time misfit is indicated in the box.

The total value of the mean RMS travel-time difference is 2.2 ms utilising proposed equation (32), 3.8 ms utilising VTI approximation and 4.0 ms for isotropic case. Thus, 2.2 ms can be considered as an uncertainty of the resulted anisotropy parameter estimation using proposed equation.

Trade-offs amongst various parameters

The inversion algorithm utilises 5 variables. This makes it necessary to evaluate the trade-offs between the pairs of parameters in order to estimate the reliability of obtained results. To this end, I permanently fix the two most reliable parameters – fast velocity azimuth (which was computed in Berard et al. (2008) and can be easily extracted from Figure 5-4) and zero-offset travel time. Trade-offs between the remaining three parameters – NMO velocity, polar anellipticity and azimuthal anellipticity are evaluated in pairs (computed for a regular grid within the

constraints specified in Table 5-2) with one of the parameters fixed. As a measure of the trade-off, I compute the objective function of the misfit between observed (t_{obs}) and computed for each cell of the regular grid (t_{calc}) travel time using the following equation:

$$Misfit = \sqrt{\frac{\sum(t_{obs} - t_{calc})^2}{N}} \tag{34}$$

where N is a number of observations.

An example of misfit plotted for depth level 760 m from the CRC-3 well DAS data is shown as a contour plot in Figure 5-22. The first two plots indicate no trade-offs between the following pairs: polar anellipticity vs azimuthal ellipticity, and azimuthal ellipticity vs NMO velocity. On the other hand, there might be a slight trade-off between NMO velocity and polar anellipticity. The first black contour represents the 2.2 ms value of misfit, which can be considered as an uncertainty of the resulting anisotropy parameters equal to the mean RMS time difference and is higher than the estimated maximum picking error of 0.5 ms. Trade-off images at this depth are representative for all depths.

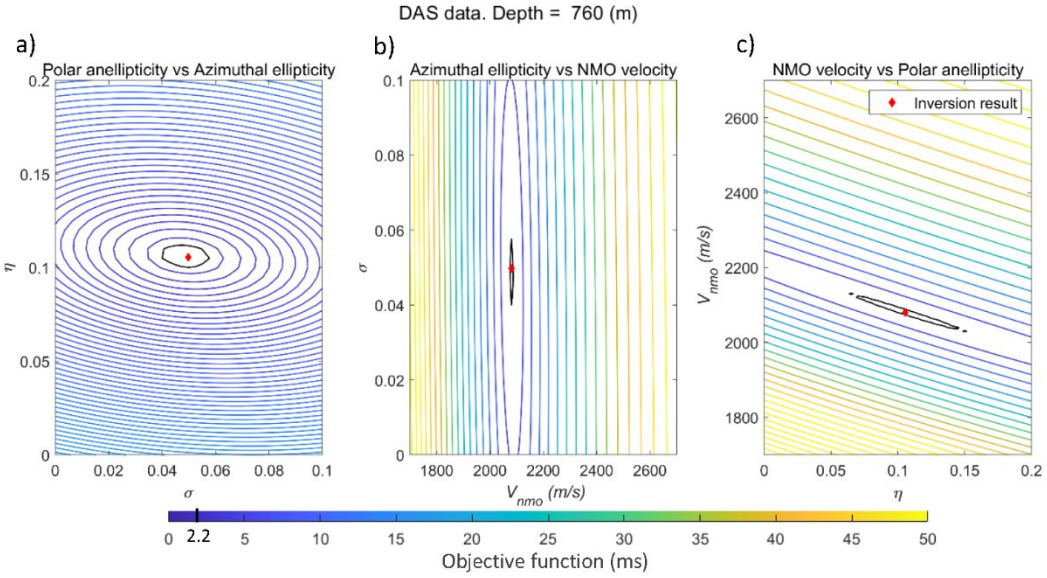

Figure 5-22 Objective function of the misfit computed for DAS data at 760 m depth between pairs of parameters used in inversion (NMO velocity, polar anellipticity and azimuthal velocity ellipticity) with fixed fast-velocity azimuth and t0. The first black contour represents the 2.2 ms value of misfit. The red rhombus indicates the result of the inversion.

Dependence on starting model

In order to estimate the dependence of the inversion results on the staring model I conducted two tests, giving lower and upper constrains (see Table 5-2) as the initial inversion models. In both cases the inversion gave the same anisotropy parameters as those shown in Figure 5-9 and Figure 5-13 obtained with a 'more reasonable' initial model. Thus, we can conclude that the inversion process found a global minimum.

5.5 Conclusions

I have analysed direct-wave arrival times from 3D VSP geophone and DAS data. The results show significant variation of direct P-wave arrival time from isotropy. The analysis demonstrates the presence of both azimuthal and polar anisotropy; hence, the simplest model for the medium is orthorhombic.

A few approaches to anisotropy estimation were examined: Local and effective approximation of the media. Local and effective approaches of anisotropy estimation are completely different. They include different anisotropic parameter set and ways of approximation of the media. However, there are certain trends in the resulted anisotropic estimates that can be analysed for consistency between the methods. Especially, the measure of azimuthal variation of velocity. In the case of local orthorhombic equation azimuthal variations resulted in splitting of the horizontal velocities in fast and slow directions below 600 m depth. It coincides to the presence of azimuthal variations as sharp increase of the effective azimuthal ellipticity parameter. In both cases, almost no azimuthal variation was observed above this level.

Analysis and comparison of 3D VSP data obtained from DAS and geophones provides information on the applicability of each of these methods for the purpose of anisotropy estimation from 3D VSP survey, along with their advantages and limitations (see Table 5-3).

Table 5-3 Comparison of Geophone and DAS 3D VSP for the purpose of anisotropy estimation. Tick indicates which method is superior according to the measures shown.

	Geophones	DAS
Signal-to-noise ratio	✓	
Depth resolution		✓
Depth coverage		✓
Sensitivity	✓	
3C	✓	
Cost (for deep wells)		✓
Speed of acquisition		✓

The main advantage of geophone data is that it shows P-wave direct arrivals for the whole range of offsets and with substantial signal-to-noise ratio. The main limitation of geophones is their inability to obtain 3D VSP data for the entire depth of the well due to the prohibitively high cost and duration of such surveys. The main advantage of the use of DAS for 3D VSP is the possibility to estimate anisotropy parameters for the entire depth range due to the relatively low cost of the DAS cable. However, the directivity of the DAS receiver precludes first break picking at far offsets. Nonetheless, the remaining range of offsets/angles is sufficient for the estimation of effective anisotropy parameters with an accuracy useful for subsurface imaging from surface seismic data.

Chapter 6.
Conclusions and further work

The Otway Site has become one of the most studied areas in the world due to the number of different seismic (and other geophysical) surveys conducted there to monitor CO_2 injection using seismic methods. The main objective of this thesis is to look at the different surface and downhole seismic datasets separately and find the ways to integrate the analysis of different datasets in order to get more value out of data with potential to optimise future monitoring concept and also to learn something new about the geological setting of the Otway site. Most of the findings of this study can be also applicable to other CCS projects that use seismic monitoring.

In this Chapter I summarise the work done in this thesis and the lessons learned. First, I conclude what has been observed from the Stage 2C surface seismic with buried receiver array and how surface seismic source effort can be mitigated. Second, I conclude findings from 3D/4D VSP surveys and the role of VSP in building of the anisotropic velocity model suitable for both VSP and surface seismic data imaging. Finally, in the "further work" section I suggest what else can be done to expand current studies based on the results of this thesis, and what else can be done in general.

6.1 Conclusions

6.1.1 Surface seismic. Stage 2C

Time-lapse surface seismic

Stage 2C of the CO2CRC Otway Project has demonstrated that the Otway site is a mature geosequestration research facility for a variety of CCS monitoring technologies. The principal monitoring technology consists of surface seismic datasets, including one baseline survey, three post-injection monitor surveys (acquired after the injection of 5, 10 and 15 kt of the supercritical CO_2, respectively), and two subsequent monitor surveys completed one and two years after the end of injection.

The use of a permanently buried seismic receiver array during Stage 2C brought many benefits to the monitoring program. Substantial improvement of the S/N ratio is one of the significant advantages of the buried geophones. An important result of the static permanent array is excellent repeatability of the acquired data, which is critical for monitoring purposes. Another advantage of the constant receiver geometry is a significant reduction in seismic data processing turnaround time. By utilising an established data processing flow, an updated plume image can be obtained within several days after the fieldwork campaign is completed. For CCS projects it is important to have processed results (plume images) almost in real time to be able to decide on further steps of the project development. Furthermore, deployment of the receiver array underground eliminates the need to use communication cables on the surface and hence drastically reduces disruption to farming activities in the area and helps maintain trusting relationships with the local community.

The high quality of the acquired seismic data together with the developed data processing strategy allows reliable surveillance of the plume evolution between the surveys. The time-lapse response provides an excellent detectability of the changes in plume shape and its lateral spreading. Analysis of the obtained images shows the absence of the unwanted migration of the plume away from the primary containment. Most of the lateral changes of plume evolution occurred between BL and M4 survey, which indicates plume stabilisation. In summary, the results show that the implemented monitoring approach is an effective and robust controlling strategy for carbon dioxide storage projects.

The processed results were used for quantitative interpretation (QI) in Glubokovskikh et al. (2019) in order to estimate temporal plume thickness. Inverted parameters of the CO_2 plume agree with other independent measurements, including repeat pulsed-neutron logging and full-waveform-inversion of offset vertical seismic profiles.

Some issues with the electronic components of the buried lines complicated the M4 data acquisition. Specifically, due to some moisture penetration into electronic components of the array, transmission errors occurred from time to time, making the spread unstable. This resulted in a few days of delay during the monitor 4 acquisition. Twenty-one percent of the digitising units were replaced before the monitor 5 survey in order to rectify the problem and the seismic spread was fully functional again during the subsequent acquisition campaign. However, by the beginning of the next data

acquisition for the Stage 3 baseline survey, the buried receiver array had systematic errors again that significantly complicated simultaneous data acquisition with multi-well 3D DAS VSP. As a result, only a small fraction of the 3D surface seismic data was acquired and Stage 3 proceeded relying only on borehole methods.

Appraisal of different monitoring approaches was conducted during the Stage 2C and the results of these experiments contributed to the Stage 3 design. The main focus of Stage 3 is on-demand remote seismic data acquisition and onsite processing of acquired data. Apart from active 4D seismic with buried receiver array, other datasets acquired during Stage 2C include active 4D VSP with geophones and DAS, passive surface seismic with buried surface receivers and DAS VSP, surface and borehole seismic with SOVs, and also utilisation of trenched DAS cables as surface receivers.

Stage 2C 4D VSP with DAS and geophones demonstrated promising results to image the subsurface, including the changes related to the injection. Permanent DAS receiver arrays enabled the acquisition of data for the entire well depth and did not significantly compete for the space in the well with other equipment. Thus, the main components of the Stage 3 became active multi-well 4D DAS VSP and multi-well DAS VSP with SOVs. The main idea behind the utilisation of SOVs is to provide the opportunity to acquire data constantly on a day-to-day basis compared to the time-spaced 3D seismic surveys. However, the coverage of a few SOVs is not comparable to a full 3D seismic survey. Thus, 4D DAS VSP is the main technique used to image 4D anomaly in the Stage 3.

Source decimation study

One of the options to optimise the seismic campaign is to analyse possible geometry layouts required for monitoring purposes. To this end, we investigated the relationships between the source density and quality of the TL image using the baseline and one monitor survey (M3). Understanding the optimal source effort required to image TL changes in the subsurface is important to minimise the time, cost and environmental footprint of the 4D seismic campaign. This study provided important results because it actually showed that we can significantly reduce the number of sources, but still obtain high-quality images.

The similar study was later conducted by Correa et al. (2018) showing similar results obtained from 3D VSP data acquired during the Stage 2C. Both these studies were very important for the Stage 3 BL acquisition campaign as it was not possible to complete the original planned acquisition campaign due to COVID-19. The decision to amend the acquisition plan was supposed to be quick and these preliminary studies helped to get the decision as quick as possible and proceed with the project (Jenkins et al. 2021).

As a recommendation for other 4D projects, after acquiring the first monitoring survey we found it very useful to analyse the effect of source reduction and its effect on the time-lapse response in order to optimise future surveys (reduce cost, improve efficiency). As was shown in our experience, spending time on the analysis of source effort beforehand can help make dynamic decisions in case of emergency during following fieldworks.

6.1.2 3D VSP. Stages 1, 2C and 3

4D VSP has a lot in common with monitoring using the permanently deployed surface geophone array. It reduces the impact on landowners and greatly reduces variability of the receiver conditions. However, there are significant differences:

- Geophone VSP tools usually have small number of receivers (AlNasser et al. 2017);
- 3D VSP provides smaller illumination zone compared to the surface seismic;
- Each image point is formed by a combination of ray paths that changes systematically away from the well, which complicates imaging and QI.

Understanding the differences between 4D VSP and surface seismic and results of the processing of 4D VSP data had been done by AlNasser et al. (2017) based on Stage 2C data. Here we focused on the extra information we can extract from VSP to support imaging. The main goal was to validate the velocity model and build an anisotropic model of the study area.

VSP is known to be a great tool to constrain velocities and study seismic anisotropy. Estimation of seismic anisotropy is very important because anisotropy is known to be significant at the Otway site. Imaging of the small 3D objects (like plume) can benefit greatly from a good velocity model, which would include anisotropy.

A significant number of 3D VSP datasets allowed us to study the distribution of direct P-wave travel times with depth and offset. This study demonstrated that both geophone and DAS data can be a good source of information for anisotropy estimation from 3D VSP surveys. The travel-time analysis shows significant variation of the arrival times from an isotropic case. The analysis demonstrates the presence of both azimuthal and polar anisotropy; hence, the simplest model for the medium is orthorhombic.

Limited broadside sensitivity of DAS cable limits the range of offsets/angles where the travel times of the direct P-waves can be reliably picked. However, visible range was sufficient to track the elliptical behaviour of travel times and calculate anisotropy parameters using DAS. Moreover, utilisation of the engineered fibre in the Stage 3 allowed improvements in the quality of the DAS data in terms of S/N ratio when compared to standard fibre data. Finally, multi-well DAS provided an opportunity to estimate velocity and anisotropy fields in five wells. Using this feature it was possible to constrain the anisotropic velocity model in 3D.

Overall, I examined a few approaches of anisotropy estimation in this study. First, I estimated local anisotropy parameters utilising slowness methods. The reason for using the slowness method selection was because DAS measurement do not include polarisations. The slowness method was performed in two steps:

1) By approximation of the orthorhombic medium by two VTI media (in 30-degree azimuthal sections along two perpendicular directions, namely fast and slow) using the Miller and Spencer approach;
2) by the application of one orthorhombic approximation to fit the whole travel time field using the Alkhalifah's approach.

First step demonstrated quite significant variation of the anisotropy parameters in fast and slow directions and provided stable results. The second step also provided stable results but included too many different variables. Moreover, the absence of both these algorithms in commercial software, which normally deals only with one VTI media, forced us to find another approximation that would be more suitable for imaging and also simpler for interpretation.

The final anisotropy estimation approach was based on orthorhombic approximation that described the whole travel time field as an effective approximation of the media. To achieve this we combined two existing approximations, one for VTI media to account for polar anisotropy, and another one that includes only azimuthal

anisotropy. The provided approximation perfectly described the travel-time field at different depths positions. This approach was applied to all the 3D VSP data available including multi-well 3D VSP with DAS acquired for a baseline Stage 3 survey. The opportunity to get anisotropy parameters in five wells allowed us to analyse the variability of the anisotropy parameters in the subsurface and build detailed anisotropic velocity model.

Analysis reveals that polar anisotropy is almost constant with depth, while azimuthal anisotropy changes significantly with depth from being negligible in the shallow part to a sharp increase below a 600 m depth. Estimated azimuth of fast direction is about 141^0, which is consistent with the measurements of the regional stress field of the study area. This fact shows that azimuthal anisotropy at Otway site is stress-induced. Parameters estimated in different wells are consistent with each other. However, there are slight lateral variations in resulted parameters, which most probably indicates variations in velocity and anisotropy fields between the wells.

6.2 Future work

This thesis covers many aspects of both VSP and surface seismic data acquisition, processing and analysis. Nevertheless, there are several things that can be done to extract more value out of data.

We demonstrated that the plume has slowed down after the M3 survey. To prove stabilisation, further analysis might be implemented. Without repeat field observations, we have to rely on long term fluid flow simulations. In order to improve the reliability of the predictions, a number of actions can be taken, including reprocessing the existing data and deriving the relevant information from the future field surveys conducted on site. This information can be used to update the geological model or give some indications of the ongoing plume development.

After injection, the plume might be dissolved in the formation, thus, further analysis of the plume over time might show the dissolution process. Thus, dissolution monitoring is another aspect that can be studied using both surface seismic and VSP time-lapse methods.

Anisotropic imaging using the velocity model obtained in this thesis for both surface seismic and VSP data can be tested and compared to the isotropic PSTM of the surface seismic data and isotropic imaging of 3D VSP data. Moreover, the obtained

anisotropic velocity model can be used for other purposes, for example, in the estimation of travel times of different events (such as the location of microseismic events, etc).

The obtained anisotropic velocity model can be further validated and updated using other data sources. In particular, the perforation shots data that were recorded on DAS during the Stage 3 drilling campaign of the new wells (Pevzner et al. 2020) can add more details to the velocity model due to significant presence of sub-horizontal rays.

So far, all the imaging of the field 4D surface seismic data at Otway site was done in the time domain. Pre-stack depth migration (PSDM), especially consisting of anisotropic parameters (anisotropic PSDM), may provide better understanding of the subsurface, which could potentially make the positioning of the plume more accurate.

CO_2 injection may cause a change of the anisotropy field due to the pressure change in the formation created by the injection. The current study analyses only the baseline survey of the Stage 3. The following monitoring surveys acquired for the Stage 3 may allow for an opportunity to estimate post-injection anisotropy.

Amplitude analysis of the wavefield is another aspect that can be studied and then integrated from the VSP data into surface seismic data. This can be achieved through the estimation of amplitude attenuation using first arrivals of direct waves of VSP data. As VSP data have shorter ray paths, this leads to a smaller attenuation of high-frequency components. Thus, VSP data can compensate for the amplitude loss of surface seismic data.

Bibliography

Abedi, M.M., M. Rashidi Fard, and M.A. Riahi. 2019. "Estimation of in situ anisotropy parameters from two perpendicular walkaway VSP lines in South Pars field." *Journal of Geophysics and Engineering* 16 (5):926-938. doi: https://doi.org/10.1093/jge/gxz056.

Aki, K., and P. Richards. 2002. *Quantitative Seismology*. Vol. 1.

Al-Jabri, Y., and M. Urosevic. 2010. "Assessing the repeatability of reflection seismic data in the presence of complex near-surface conditions CO2CRC Otway Project, Victoria, Australia." *Exploration Geophysics* 41 (1):24-30. doi: Doi 10.1071/Eg09010.

Alkhalifah, T. 2003. "An acoustic wave equation for orthorhombic anisotropy." *Geophysics* 68. doi: https://doi.org/10.1190/1.1598109.

Alkhalifah, T., and I. Tsvankin. 1995. "Velocity analysis for transversely isotropic media." *GEOPHYSICS* 60 (5):1550-1566. doi: https://doi.org/10.1190/1.1443888.

AlNasser, H., R. Pevzner, K. Tertyshnikov, D. Popik, and M. Urosevic. 2017. "Application of 4D VSP for Monitoring Of Small-Scale Supercritical CO2 Injection: Stage 2C of CO2CRC Otway Project Case Study." Fourth EAGE Workshop on Borehole Geophysics, Abu Dhabi, UAE.

Asgharzadeh, M., A. Bóna, R. Pevzner, M. Urosevic, and Gurevich. B. 2013. "Reliability of the slowness and slowness-polarization methods for anisotropy estimation in VTI media from 3C walkaway VSP data." *GEOPHYSICS* 78 (5):WC93-WC102. doi: https://doi.org/10.1190/geo2012-0409.1.

Bakku, S. 2015. "Fracture characterization from seismic measurements in a borehole." Ph.D. thesis, Massachusetts Institute of Technology.

Bakulin, A., V. Grechka, and I. Tsvankin. 2000. "Estimation of fracture parameters from reflection seismic data—Part I: HTI model due to a single fracture set." *GEOPHYSICS* 65 (6):1788-1802. doi: https://doi.org/10.1190/1.1444863.

Berard, T., B. Sinha, P. van Ruth, T. Dance, Z. John, and C. Tan. 2008. "Stress Estimation at the Otway CO2 Storage Site, Australia." SPE Asia Pacific Oil and Gas Conference and Exhibition, Perth, Australia.

Bona, A., T. Dean, J. Correa, R. Pevzner, K. Tertyshnikov, and L. Van Zaanen. 2017. "Amplitude and Phase Response of DAS Receivers." 2017 (1):1-5. doi: https://doi.org/10.3997/2214-4609.201701200.

Bostick, F. X. 2000. "Field experimental results of three-component fiber-optic seismic sensors." In *SEG Technical Program Expanded Abstracts 2000*, 21-24.

Caspari, E., R. Pevzner, B. Gurevich, T. Dance, J. Ennis-King, Y. Cinar, and M. Lebedev. 2015. "Feasibility of CO2 plume detection using 4D seismic: CO2CRC Otway Project case study — Part 1: Rock-physics modeling." *GEOPHYSICS* 80 (4):B95-B104. doi: https://doi.org/10.1190/geo2014-0459.1.

Castagna, J., and M. Backus. 1993. *Offset-Dependent Reflectivity–Theory and Practice of AVO Analysis*. Vol. 8: Society of Exploration Geophysicists.

Chadwick, R. A., D. Noy, R. Arts, and O. Eiken. 2009. "Latest time-lapse seismic data from Sleipner yield new insights into CO2 plume development." *Energy Procedia* 1 (1):2103-2110. doi: 10.1016/j.egypro.2009.01.274.

CO2CRC. "The Cooperative Research Centre for Greenhouse Gas Technologies." http://www.co2crc.com.au/.

Cook, P.J. (Ed.). 2014. *Geologically Storing Carbon: Learning from the Otway Project Experience*. Melbourne: CSIRO Publishing.

Correa, J., B.M. Freifeld, M. Robertson, R. Pevzner, A. Bona, and D. Popik. 2017. "Distributed Acoustic Sensing Applied to 4D Seismic: Preliminary Results From the CO2CRC Otway Site Field Trials." 2017 (1):1-5. doi: https://doi.org/10.3997/2214-4609.201700811.

Correa, J., R. Pevzner, S. Popik, K. Tertyshnikov, A. Bona, and B. M. Freifeld. 2018. "Application of 3D VSP acquired with DAS and 3C geophones for site characterization and monitoring program design: preliminary results from Stage 3 of the CO2CRC Otway project." 88th SEG Annual meeting, Anaheim, California, USA.

Correa, Julia, Roman Isaenkov, Sinem Yavuz, Alexey Yurikov, Konstantin Tertyshnikov, Todd Wood, Barry M. Freifeld, and Roman Pevzner. 2021. "DAS/SOV: Rotary seismic sources with fiber-optic sensing facilitates autonomous permanent reservoir monitoring." *GEOPHYSICS*:1-42. doi: https://doi.org/10.1190/geo2020-0612.1.

Corrigan, D., R. Withers, J. Darnall, and T. Skopinski. 1996. "Fracture mapping from azimuthal velocity analysis using 3D surface seismic data." 66th SEG Annual Meeting, Denver, Colorado, USA.

Cox, B., P. Wills, D. Kiyashchenko, J. Mestayer, J. Lopez, S. Bourne, R. Lupton, G. Solano, N. Henderson, and D. Hill. 2012. "Distributed acoustic sensing for geophysical measurement, monitoring and verification." *CSEG recorder* 37 (2):7-13.

Daley, T. M., B.M. Freifeld, J. Ajo-Franklin, S. Dou, R. Pevzner, V. Shulakova, S. Kashikar, D.E. Miller, J. Goetz, L. Henninges, and S. Lueth. 2013. "Field testing of fiber-optic distributed acoustic sensing (DAS) for subsurface seismic monitoring." *The Leading Edge* 32 (6):699-706. doi: https://doi.org/10.1190/tle32060699.1.

Daley, T. M., L.R. Myer, J. E. Peterson, E. L. Majer, and G. M. Hoversten. 2008. "Time-lapse crosswell seismic and VSP monitoring of injected CO2 in a brine aquifer." *Environmental Geology* 54 (8):1657-1665. doi: https://doi.org/10.1007/s00254-007-0943-z.

Dance, T., and L. Paterson. 2016. "Observations of carbon dioxide saturation distribution and residual trapping using core analysis and repeat pulsed-neutron logging at the CO2CRC Otway site." *International Journal of Greenhouse Gas Control* 47:210-220. doi: https://doi.org/10.1016/j.ijggc.2016.01.042.

Dance, T., L. Spencer, and Josh-Q. Xu. 2009. "Geological characterisation of the Otway project pilot site: What a difference a well makes." *Energy Procedia* 1 (1):2871-2878. doi: https://doi.org/10.1016/j.egypro.2009.02.061.

Dean, T., T. Cuny, and A.H. Hartog. 2017. "The effect of gauge length on axially incident P-waves measured using fibre optic distributed vibration sensing." *Geophysical Prospecting* 65 (1):184-193. doi: https://doi.org/10.1111/1365-2478.12419.

Dewangan, P., and V. Grechka. 2003. "Inversion of multicomponent, multiazimuth, walkaway VSP data for the stiffness tensor." *GEOPHYSICS* 68 (3):1022-1031. doi: https://doi.org/10.1190/1.1581073.

Eiken, O., P. S. Ringrose, C. Hermanrud, B. Nazarian, T. Torp, and L. Høier. 2011. "Lessons learned from 14 years of CCS operations: Sleipner, In Salah and Snøhvit." *Energy Procedia* 4:5541-5548. doi: https://doi.org/10.1016/j.egypro.2011.02.541.

Einstein, A. 1916. "Die Grundlage der allgemeinen Relativitätstheorie." *Annalen der Physik* 354 (7):769-822. doi: https://doi.org/10.1002/andp.19163540702.

Finley, R. 2014. "An overview of the Illinois Basin – Decatur Project." *Greenhouse Gases: Science and Technology* 4. doi: https://doi.org/10.1002/ghg.1433.

Flett, M., J. Brantjes, R. Gurton, J. McKenna, T. Tankersley, and M. Trupp. 2009. "Subsurface development of CO2 disposal for the Gorgon Project." *Energy Procedia* 1 (1):3031-3038. doi: https://doi.org/10.1016/j.egypro.2009.02.081.

Furre, AK., O. Eiken, H. Alnes, J.N. Vevatne, and A.F. Kiær. 2017. "20 Years of Monitoring CO2-injection at Sleipner." *Energy Procedia* 114:3916-3926. doi: https://doi.org/10.1016/j.egypro.2017.03.1523.

Gaiser, J.E. 1990. "Transversely isotropic phase velocity analysis from slowness estimates." *Journal of Geophysical Research: Solid Earth* 95 (B7):11241-11254. doi: https://doi.org/10.1029/JB095iB07p11241.

Galperin, E. 1985. *Vertical Seismic Profiling and Its Exploration Potential*: Springer Netherlands.

Gavin, L.J., and D. Lumley. 2016. "Stress-induced seismic azimuthal anisotropy in the upper crust across the North West Shelf, Australia." *Journal of Geophysical Research: Solid Earth* 121 (2):1023-1039. doi: https://doi.org/10.1002/2015JB012568.

Global CCS Institute. 2020. GLOBAL STATUS OF CCS 2020. CO2RE database - Facilities Report.

Glubokovskikh, S., R. Pevzner, T. Dance, E. Caspari, D. Popik, V. Shulakova, and B. Gurevich. 2016. "Seismic monitoring of CO2 geosequestration: CO2CRC Otway case study using full 4D FDTD approach." *International Journal of Greenhouse Gas Control* 49:201-216. doi: https://doi.org/10.1016/j.ijggc.2016.02.022.

Glubokovskikh, S., R. Pevzner, J. Gunning, T. Dance, V. Shulakova, D. Popik, S. Popik, M. Bagheri, and B. Gurevich. 2019. "How well can time-lapse seismic characterize a small CO2 leakage into a saline aquifer: CO2CRC Otway 2C experiment (Victoria, Australia)." *International Journal of Greenhouse Gas Control*. doi: https://doi.org/10.1016/j.ijggc.2019.102854.

Glubokovskikh, S., R. Pevzner, E. Sidenko, K. Tertyshnikov, B. Gurevich, S. Shatalin, A. Slunyaev, and E. Pelinovsky. 2021. "Downhole distributed acoustic sensing reveals the wave field structure of the coastal microseisms." doi: https://doi.org/10.31223/X5W30H10.31223/X5W30H.

Godoi, JMA., and PHL. dos Santos Matai. 2021. "Enhanced oil recovery with carbon dioxide geosequestration: first steps at Pre-salt in Brazil." *Journal of Petroleum Exploration and Production*. doi: 10.1007/s13202-021-01102-8https://doi.org/10.1007/s13202-021-01102-8.

Grechka, V., P. Jorgensen, and J.L. Lopez. 2006. "Anisotropy Estimation From Marine 3D VSP Data." Offshore Technology Conference.

Grechka, V., and A. Mateeva. 2007. "Inversion of P-wave VSP data for local anisotropy: Theory and case study." *GEOPHYSICS* 72 (4):D69-D79. doi: https://doi.org/10.1190/1.2742970.

Grechka, V., A. Pech, I. Tsvankin, and B. Han. 2001. "Velocity analysis for tilted transversely isotropic media: A physical modeling example." *GEOPHYSICS* 66 (3):904-910. doi: https://doi.org/10.1190/1.1444980.

Grechka, V., S. Theophanis, and I. Tsvankin. 1999. "Joint inversion of P- and PS-waves in orthorhombic media: Theory and a physical modeling study." *GEOPHYSICS* 64 (1):146-161. doi: https://doi.org/10.1190/1.1444512.

Grechka, V., and I. Tsvankin. 1998. "Feasibility of nonhyperbolic moveout inversion in transversely isotropic media." *GEOPHYSICS* 63 (3):957-969. doi: https://doi.org/10.1190/1.1444407.

Grechka, V., and I. Tsvankin. 1999. "3-D moveout velocity analysis and parameter estimation for orthorhombic media." *GEOPHYSICS* 64 (3):820-837. doi: https://doi.org/10.1190/1.1444593.

Grechka, V., I. Tsvankin, A. Bakulin, Hansen J.O., and C. Signer. 2002. "Joint inversion of PP and PS reflection data for VTI media: A North Sea case study." *GEOPHYSICS* 67 (5):1382-1395. doi: https://doi.org/10.1190/1.1512784.

Gurevich, B., M. Pervukhina, and D. Makarynska. 2011. "An analytic model for the stress-induced anisotropy of dry rocks." *GEOPHYSICS* 76 (3):WA125-WA133. doi: https://doi.org/10.1190/1.3567950.

Hance, T., T. Jiang, G. Zhan, E. Kjos, R. Geetan, S. Soulas, and I. Thomas. 2016. "Learnings from Distributed Acoustic Sensing Data Processing for Seismic Applications - A Case Study from the North Sea." 2016 (1):1-5. doi: https://doi.org/10.3997/2214-4609.201601601.

Hansen, O., D. Gilding, B. Nazarian, B. Osdal, P. S. Ringrose, J. Kristoffersen, O. Eiken, and H. Hansen. 2013. "Snøhvit: The History of Injecting and Storing 1 Mt CO2 in the Fluvial Tubåen Fm." *Energy Procedia* 37:3565-3573. doi: https://doi.org/10.1016/j.egypro.2013.06.249.

Hartog, A. 2017. *An Introduction to Distributed Optical Fibre Sensors*: CRC Press.

Heidbach, O., M. Rajabi, K. Reiter, M. Ziegler, and WSM Team. 2016. World Stress Map Database Release 2016. V. 1.1. GFZ Data Services.

Helbig, K. 1994. *Foundations of Anisotropy for Exploration Seismics*: Elsevier Science Serials.

Hitchon, B. 2012. "Best practices for validating CO2 geological storage: Observations and guidance from the IEA GHG Weyburn-Midale CO2 Monitoring Project." *Geoscience Publishing, Sherwood Park*.

Horne, S., and S. Leaney. 2000. "Short note: Polarization and slowness component inversion for TI anisotropy." *Geophysical Prospecting* 48 (4):779-788. doi: https://doi.org/10.1046/j.1365-2478.2000.00205.x.

Hovorka, S., T. Meckel, and R. Treviño. 2013. "Monitoring a large-volume injection at Cranfield, Mississippi—Project design and recommendations." *International Journal of Greenhouse Gas Control* 18:345-360. doi: https://doi.org/10.1016/j.ijggc.2013.03.021.

Hovorka, S.D., S.M. Benson, C. Doughty, B. M. Freifeld, S. Sakurai, T. M. Daley, Y.K. Kharaka, M.H. Holtz, R.C. Trautz, H.S. Nance, L.R. Myer, and K.G. Knauss. 2006. "Measuring permanence of CO2 storage in saline formations: the Frio experiment." *Environmental Geosciences* 13 (2):105-121. doi: https://doi.org/10.1306/eg.11210505011.

Huang, F., P. Bergmann, C. Juhlin, M. Ivandic, S. Lüth, A. Ivanova, T. Kempka, J. Henninges, D. Sopher, and F. Zhang. 2018. "The first post-injection seismic monitor survey at the Ketzin pilot CO2 storage site: results from time-lapse analysis." *Geophysical Prospecting* 66 (1):62-84. doi: https://doi.org/10.1111/1365-2478.12497.

Isaenkov, R., R. Pevzner, S. Glubokovskikh, S. Yavuz, A. Yurikov, K. Tertyshnikov, B. Gurevich, J. Correa, T. Wood, B. M. Freifeld, M. Mondanos, S. Nikolov, and P. Barraclough. 2021. "An automated system for continuous monitoring of CO2 geosequestration using multi-well offset VSP with permanent seismic sources and receivers: Stage 3 of the CO2CRC Otway Project." *International Journal of Greenhouse Gas Control* 108:103317. doi: https://doi.org/10.1016/j.ijggc.2021.103317.

Ivandic, M., C. Juhlin, S. Lüth, P. Bergmann, A. Kashubin, D. Sopher, A. Ivanova, G. Baumann, and J. Henninges. 2015. "Geophysical monitoring at the Ketzin pilot site for CO 2 storage: New insights into the plume evolution." *International Journal of*

Greenhouse Gas Control 32:90-105. doi: https://doi.org/10.1016/j.ijggc.2014.10.015.

Ivanova, A., A. Kashubin, N. Juhojuntti, J. Kummerow, J. Henninges, C. Juhlin, S. Lüth, and M. Ivandic. 2012. "Monitoring and volumetric estimation of injected CO2 using 4D seismic, petrophysical data, core measurements and well logging: a case study at Ketzin, Germany." *Geophysical Prospecting* 60 (5):957-973. doi: https://doi.org/10.1111/j.1365-2478.2012.01045.x.

Jenkins, C. R., P. Barraclough, M. Bagheri, J. Correa, T. Dance, J. Ennis-King, B. M. Freifeld, S. Glubokovskikh, C. Green, J. Gunning, B. Gurevich, R. Isaenkov, S. Jackson, R. Pevzner, L. Ricard, K. Tertyshnikov, A. Wilkins, T. Wood, S. Yavuz, and A. Yurikov. 2021. "Drilling an Array of Monitoring Wells for a CCS Experiment: Lessons From Otway Stage 3." *SSRN Electronic Journal*. doi: https://dx.doi.org/10.2139/ssrn.3814479.

Jenkins, C. R., A. Chadwick, and S. Hovorka. 2015. "The state of the art in monitoring and verification—Ten years on." *International Journal of Greenhouse Gas Control* 40:312-349. doi: https://doi.org/10.1016/j.ijggc.2015.05.009.

Jenkins, C. R., P. J. Cook, J. Ennis-King, J. Undershultz, C. Boreham, T. Dance, P. de Caritat, D. M. Etheridge, B. M. Freifeld, A. Hortle, D. Kirste, L. Paterson, R. Pevzner, U. Schacht, S. Sharma, L. Stalker, and M. Urosevic. 2012. "Safe storage and effective monitoring of CO2 in depleted gas fields." *Proceedings of the National Academy of Sciences of the United States of America* 109 (2):E35-41. doi: https://doi.org/10.1073/pnas.1107255108.

Jenkins, C. R., S. Marshall, T. Dance, J. Ennis-King, S. Glubokovskikh, B. Gurevich, T. La Force, L. Paterson, R. Pevzner, E. Tenthorey, and M. Watson. 2017. "Validating Subsurface Monitoring as an Alternative Option to Surface M&V - The CO2CRC's Otway Stage 3 Injection." *Energy Procedia* 114:3374-3384. doi: https://doi.org/10.1016/j.egypro.2017.03.1469.

Jílek, P., B. Hornby, and A. Ray. 2003. "Inversion of 3D VSP P-wave Data For Local Anisotropy: a Case Study." 2003 SEG Annual Meeting.

Johnston, D. 2013. *Practical Applications of Time-lapse Seismic Data*, *Distinguished Instructor Series*: Society of Exploration Geophysicists. doi:10.1190/1.9781560803126.

Johnston, J., and N. Christensen. 1995. "Seismic anisotropy of shales." *Journal of Geophysical Research: Solid Earth* 100 (B4):5991-6003. doi: https://doi.org/10.1029/95JB00031.

Kikuta, K., S. Hongo, D. Tanase, and T. Ohsumi. 2005. "Field test of CO2 injection in Nagaoka, Japan." In *Greenhouse Gas Control Technologies 7*, edited by E. S. Rubin, D. W. Keith, C. F. Gilboy, M. Wilson, T. Morris, J. Gale and K. Thambimuthu, 1367-1372. Oxford: Elsevier Science Ltd.

Kirste, D., R. Haese, C. Boreham, and U. Schacht. 2014. "Evolution of formation water chemistry and geochemical modelling of the CO2CRC Otway Site residual gas saturation test." *Energy Procedia* 63:2894-2902. doi: https://doi.org/10.1016/j.egypro.2014.11.312.

Krassay, A. A., D. L. Cathro, and D. J. Ryan. 2004. *A regional tectonostratigraphic framework for the Otway Basin*: Eastern Australasian Basins Symposium II, Petroleum Exploration Society of Australia.

Kuvshinov, B. 2016. "Interaction of helically wound fibre-optic cables with plane seismic waves." *Geophysical Prospecting* 64 (3):671-688. doi: https://doi.org/10.1111/1365-2478.12303.

Landro, M., and K. Bjørlykke. 2010. "4D Seismic." In, 427-444.

Leaney, W.S. 2008. "Polar anisotropy from walkway VSPs." *The Leading Edge* 27 (10):1242-1250. doi: https://doi.org/10.1190/1.2996535.

Lumley, D. 2001. "Time-lapse seismic reservoir monitoring." *GEOPHYSICS* 66 (1):50-53. doi: https://doi.org/10.1190/1.1444921.

Lumley, D. 2010. "4D Seismic Monitoring of CO2 Sequestration." *Geophysics* 29. doi: https://doi.org/10.1190/1.3304817.

Lüth, S., P. Bergmann, C. Cosma, N. Enescu, R. Giese, J. Götz, A. Ivanova, C. Juhlin, A. Kashubin, C. Yang, and F. Zhang. 2011. "Time-lapse seismic surface and down-hole measurements for monitoring CO2 storage in the CO2SINK project (Ketzin, Germany)." *Energy Procedia* 4:3435-3442. doi: https://doi.org/10.1016/j.egypro.2011.02.268.

Martens, S., T. Kempka, A. Liebscher, S. Lüth, F. Möller, A. Myrttinen, B. Norden, C. Schmidt-Hattenberger, M. Zimmer, M. Kühn, and Group The Ketzin. 2012. "Europe's longest-operating on-shore CO2 storage site at Ketzin, Germany: a progress report after three years of injection." *Environmental Earth Sciences* 67 (2):323-334. doi: https://doi.org/10.1007/s12665-012-1672-5.

Mateeva, A., J. Lopez, D. Chalenski, M. Tatanova, P. Zwartjes, Z. Yang, S. Bakku, K. de Vos, and H. Potters. 2017. "4D DAS VSP as a tool for frequent seismic monitoring in deep water." *The Leading Edge* 36 (12):995-1000. doi: 10.1190/tle36120995.1.

Mateeva, A., J. Lopez, H. Potters, J. Mestayer, B. Cox, D. Kiyashchenko, P. Wills, S. Grandi, K. Hornman, B. Kuvshinov, W. Berlang, Z. Yang, and R. Detomo. 2014. "Distributed acoustic sensing for reservoir monitoring with vertical seismic profiling." *Geophysical Prospecting* 62 (4):679-692. doi: https://doi.org/10.1111/1365-2478.12116.

Mavko, G., T. Mukerji, and N. Godfrey. 1995. "Predicting stress-induced velocity anisotropy in rocks." *GEOPHYSICS* 60 (4):1081-1087. doi: https://doi.org/10.1190/1.1443836.

Mestayer, J., S. Grandi Karam, B. Cox, P. Wills, A. Mateeva, J. Lopez, D. Hill, and A. Lewis. 2012. "Distributed Acoustic Sensing for Geophysical Monitoring." doi: https://doi.org/10.3997/2214-4609.20148800.

Miller, D.E., and C. Spencer. 1994. "An exact inversion for anisotropic moduli from phase slowness data." *Journal of Geophysical Research: Solid Earth* 99 (B11):21651-21657. doi: https://doi.org/10.1029/94JB01848.

Naldrett, G. 2021. "A new era of borehole measurements for permanent reservoir monitoring." *First Break* 39 (2):77-81. doi: https://doi.org/10.3997/1365-2397.fb2021014.

Naldrett, G., C. Cerrahoglu, and V. Mahue. 2018. "Production Monitoring Using Next-Generation Distributed Sensing Systems." *Petrophysics - The SPWLA Journal of Formation Evaluation and Reservoir Description* 59 (04):496-510. doi: https://doi.org/10.30632/PJV59V4-2018a5.

O'Brien, J., F. Kilbride, and F. Lim. 2004. "Time-lapse VSP reservoir monitoring." *The Leading Edge* 23 (11):1178-1184. doi: https://doi.org/10.1190/1.1825943.

Onajite, E. 2014. "Chapter 3 - Understanding Seismic Exploration." In *Seismic Data Analysis Techniques in Hydrocarbon Exploration*, edited by Enwenode Onajite, 33-62. Oxford: Elsevier.

Parker, T., S. Shatalin, and M. Farhadiroushan. 2014. "Distributed Acoustic Sensing – a new tool for seismic applications." *First Break* 32 (2). doi: https://doi.org/10.3997/1365-2397.2013034.

Pevzner, R., A. Bona, B. Gurevich, I. Yavuz, A. Shaiban, and M. Urosevic. 2010. "Seismic anisotropy estimation from VSP data: CO2CRC Otway project case study." 80th SEG Annual Meeting, Denver, Colorado, USA.

Pevzner, R., B. Gurevich, and M. Urosevic. 2011. "Estimation of azimuthal anisotropy from VSP data using multicomponent S-wave velocity analysis." *GEOPHYSICS* 76 (5):D1-D9. doi: https://doi.org/10.1190/geo2010-0290.1.

Pevzner, R., R. Isaenkov, S. Yavuz, A. Yurikov, K. Tertyshnikov, P. Shashkin, B. Gurevich, J. Correa, S. Glubokovskikh, T. Wood, B. M. Freifeld, and P. Barraclough. 2021. "Seismic monitoring of a small CO2 injection using a multi-well DAS array: Operations and initial results of Stage 3 of the CO2CRC Otway project." *International Journal of Greenhouse Gas Control* 110:103437. doi: https://doi.org/10.1016/j.ijggc.2021.103437.

Pevzner, R., V. Shulakova, A. Kepic, and M. Urosevic. 2011. "Repeatability analysis of land time-lapse seismic data: CO2CRC Otway pilot project case study." *Geophysical Prospecting* 59 (1):66-77. doi: https://doi.org/10.1111/j.1365-2478.2010.00907.x.

Pevzner, R., K. Tertyshnikov, V. Shulakova, M. Urosevic, A. Kepic, B. Gurevich, and R. Singh. 2015. "Design and deployment of a buried geophone array for CO2geosequestration monitoring: CO2CRC Otway Project, Stage 2C." SEG Technical Program Expanded Abstracts 2015.

Pevzner, R., K. Tertyshnikov, E. Sidenko, and L. Ricard. 2020. "Monitoring Drilling and Completion Operations Using Distributed Acoustic Sensing: CO2CRC Stage 3 Project Case Study." 2020 (1):1-5. doi: https://doi.org/10.3997/2214-4609.202030004.

Pevzner, R., M. Urosevic, D. Popik, V. Shulakova, K. Tertyshnikov, E. Caspari, J. Correa, T. Dance, A. Kepic, S. Glubokovskikh, S. Ziramov, B. Gurevich, R. Singh, M. Raab, M. Watson, T. M. Daley, M. Robertson, and B. M. Freifeld. 2017. "4D surface seismic tracks small supercritical CO 2 injection into the subsurface: CO2CRC Otway Project." *International Journal of Greenhouse Gas Control* 63:150-157. doi: https://doi.org/10.1016/j.ijggc.2017.05.008.

Popik, D., V. Shulakova, K. Tertyshnikov, S. Ziramov, M. Urosevic, and R. Pevzner. 2018. "Time-lapse surface seismic processing for Stage 2C of CO2CRC Otway Project." AEGC Extended Abstracts, Sydney, Australia.

Popik, S., R. Pevzner, and A. Bona. 2020. "P-Wave Anisotropy Estimation from 3D VSP Data Acquired with Geophones and DAS at Otway Site." 82nd EAGE Annual Conference & Exhibition, Amsterdam, The Netherlands.

Popik, S., R. Pevzner, A. Bona, K. Tertyshnikov, S. Glubokovskikh, and B. Gurevich. 2020. "P-wave Anisotropy Parameters Estimation from Multi-well 3D VSP using DAS: Stage 3 of the CO2CRC Otway Project." EAGE Workshop on Fiber Optic Sensing for Energy Applications in Asia Pacific.

Popik, S., R. Pevzner, A. Bona, K. Tertyshnikov, S. Glubokovskikh, and B. Gurevich. 2021. "Estimation of P-wave anisotropy parameters from 3D vertical seismic profile with distributed acoustic sensors and geophones for seismic imaging in the CO2CRC Otway Project." *Geophysical Prospecting*. doi: https://doi.org/10.1111/1365-2478.13080.

Popik, S., R. Pevzner, K. Tertyshnikov, D. Popik, M. Urosevic, V. Shulakova, S. Glubokovskikh, and B. Gurevich. 2020. "4D surface seismic monitoring the evolution of a small CO2 plume during and after injection: CO2CRC Otway Project study." *Exploration Geophysics*:1-11. doi: https://doi.org/10.1080/08123985.2020.1735934.

Popik, S., D. Popik, and R. Pevzner. 2019. "Effect of Density of Seismic Sources on the Quality of the 4D Seismic Data." 81st EAGE Conference and Exhibition 2019, London, UK.

Rajabi, M., M. Tingay, O. Heidbach, R. Hillis, and S. Reynolds. 2017. "The present-day stress field of Australia." *Earth-Science Reviews* 168:165-189. doi: https://doi.org/10.1016/j.earscirev.2017.04.003.

Richter, P., T. Parker, C. Woerpel, W. Wu, R. Rufino, and M. Farhadiroushan. 2019. "High-resolution distributed acoustic sensor using engineered fiber for hydraulic fracture monitoring and optimization in unconventional completions." In *SEG Technical Program Expanded Abstracts 2019*, 4874-4878. Society of Exploration Geophysicists.

Ringrose, P. S. 2018. "The CCS hub in Norway: some insights from 22 years of saline aquifer storage." *Energy Procedia* 146:166-172. doi: https://doi.org/10.1016/j.egypro.2018.07.021.

Ringrose, P. S. 2020. *How to Store CO2 Underground: Insights from early-mover CCS Projects*: Springer International Publishing.

Ringrose, P. S., A. S. Mathieson, I. W. Wright, F. Selama, O. Hansen, R. Bissell, N. Saoula, and J. Midgley. 2013. "The In Salah CO2 Storage Project: Lessons Learned and Knowledge

Transfer." *Energy Procedia* 37:6226-6236. doi: https://doi.org/10.1016/j.egypro.2013.06.551.

Rock, L., S. O'Brien, S. Tessarolo, J. Duer, V.O. Bacci, B. Hirst, D. Randell, M. Helmy, J. Blackmore, C. Duong, A. Halladay, N. Smith, T. Dixit, S. Kassam, and M. Yaychuk. 2017. "The Quest CCS Project: 1st Year Review Post Start of Injection." *Energy Procedia* 114:5320-5328. doi: https://doi.org/10.1016/j.egypro.2017.03.1654.

Sandiford, M., M. Wallace, and D. Coblentz. 2004. "Origin of the in situ stress field in south-eastern Australia." *Basin Research* 16 (3):325-338. doi: https://doi.org/10.1111/j.1365-2117.2004.00235.x.

Sayers, C.M. 2002. "Stress-dependent elastic anisotropy of sandstones." *Geophysical Prospecting* 50 (1):85-95. doi: https://doi.org/10.1046/j.1365-2478.2002.00289.x.

Sayers, C.M. 2005. "Seismic anisotropy of shales." *Geophysical Prospecting* 53 (5):667-676. doi: https://doi.org/10.1111/j.1365-2478.2005.00495.x.

Sayers, C.M. 2010. *Geophysics Under Stress: Geomechanical Applications of Seismic and Borehole Acoustic Waves*: Society of Exploration Geophysicists.

Sharma, S., P. J. Cook, C. R. Jenkins, T. Steeper, M. Lees, and N. Ranasinghe. 2011. "The CO2CRC Otway Project: Leveraging experience and exploiting new opportunities at Australia's first CCS project site." *Energy Procedia* 4:5447-5454. doi: https://doi.org/10.1016/j.egypro.2011.02.530.

Shulakova, V., R. Pevzner, J.C. Dupuis, M. Urosevic, K. Tertyshnikov, D. Lumley, and B. Gurevich. 2015. "Burying receivers for improved time-lapse seismic repeatability: CO2CRC Otway field experiment." *Geophysical Prospecting* 63 (1):55-69. doi: https://doi.org/10.1111/1365-2478.12174.

Tertyshnikov, K., H. AlNasser, R. Pevzner, M. Urosevic, and A. Greenwood. 2018. "3D VSP for Monitoring of the Injection of Small Quantities of CO2 – CO2CRC Otway Case Study." 80th EAGE Conference and Exhibition 2018, Copenhagen, Denmark.

Tertyshnikov, K., A. Egorov, R. Pevzner, and A. Bóna. 2017. "Offset VSP for the Reservoir Monitoring." Fourth EAGE Workshop on Borehole Geophysics, Abu Dhabi, UAE.

Thomsen, L. 1986. "Weak elastic anisotropy." *Geophysics* 51 (10):1954-1966. doi: 10.1190/1.1442051.

Thomsen, L. 2002. *Understanding Seismic Anisotropy in Exploration and Exploitation*: Society of Exploration Geophysicists.

Tsvankin, I. 1997. "Anisotropic parameters and P-wave velocity for orthorhombic media." *Geophysics* 62 (4):1292-1309. doi: https://doi.org/10.1190/1.1444231.

Tsvankin, I. 2001. *Seismic Signatures and Analysis of Reflection Data in Anisotropic Media*: Elsevier Science.

Tsvankin, I. 2012. *Seismic Signatures and Analysis of Reflection Data in Anisotropic Media, Third Edition*: Society of Exploration Geophysicists.

Tsvankin, I., J. Gaiser, V. Grechka, M. Van der Baan, and L. Thomsen. 2010. "Seismic anisotropy in exploration and reservoir characterization: An overview." *GEOPHYSICS* 75 (5):75A15-75A29. doi: https://doi.org/10.1190/1.3481775.

Tsvankin, I., and L. Thomsen. 1994. "Nonhyperbolic reflection moveout in anisotropic media." *GEOPHYSICS* 59 (8):1290-1304. doi: https://doi.org/10.1190/1.1443686.

Urosevic, M., R. Pevzner, A. Kepic, P. Wisman, V. Shulakova, and S. Sharma. 2010. "Time-lapse seismic monitoring of CO2 injection into a depleted gas reservoir—Naylor Field, Australia." *The Leading Edge* 29 (2):164-169. doi: https://doi.org/10.1190/1.3304819.

Valishin, O. 2018. "Shifts in Seismic Technology." *Oilfield Technology* 11 (11).

Van der Baan, M., and J.M. Kendall. 2002. "Estimating anisotropy parameters and traveltimes in the τ-p domain." *GEOPHYSICS* 67 (4):1076-1086. doi: https://doi.org/10.1190/1.1500368.

White, D. J. 2011. "Geophysical monitoring of the Weyburn CO2 flood: Results during 10 years of injection." *Energy Procedia* 4:3628-3635. doi: https://doi.org/10.1016/j.egypro.2011.02.293.

Worth, K., D. J. White, R. Chalaturnyk, J. Sorensen, C. Hawkes, B. Rostron, J. Johnson, and A. Young. 2014. "Aquistore Project Measurement, Monitoring, and Verification: From Concept to CO2 Injection." *Energy Procedia* 63:3202-3208. doi: https://doi.org/10.1016/j.egypro.2014.11.345.

Yavuz, S., B. M. Freifeld, R. Pevzner, K. Tertyshnikov, A. Dzunic, S. Ziramov, V. Shulakova, M. Robertson, T. M. Daley, A. Kepic, M. Urosevic, and B. Gurevich. 2016. "Subsurface

Imaging Using Buried DAS and Geophone Arrays - Preliminary Results from CO2CRC Otway Project." 78th EAGE Conference and Exhibition 2016, Vienna, Austria.

Yurikov, A., K. Tertyshnikov, R. Isaenkov, E. Sidenko, S. Glubokovskikh, P. Barraclough, P. Shashkin, and R. Pevzner. 2021. "Multi-well 3D DAS VSP imaging with engineered fibres: CO2CRC Otway Project case study." *GEOPHYSICS*:1-34. doi: https://doi.org/10.1190/geo2020-0670.1.

Zhang, H. 2015. "Chapter 6 - Reverse-Time Migration: Principles, Practical Issues, and Recent Developments." In *Seismic Exploration of Hydrocarbons in Heterogeneous Reservoirs*, edited by Jing Ba, Qizhen Du, José M. Carcione, Houzhu Zhang and Tobias M. Müller, 205-251. Elsevier.

Zheng, X., and I. Pšenčík. 2002. "Local Determination of Weak Anisotropy Parameters from qP-wave Slowness and Particle Motion Measurements." *Pure and Applied Geophysics* 159 (7):1881-1905. doi: https://doi.org/10.1007/s00024-002-8713-z.

Appendix A: Attribution of Authorship

1. Paper “Popik, S., R. Pevzner, K. Tertyshnikov, D. Popik, M. Urosevic, V. Shulakova, S. Glubokovskikh, and B. Gurevich. 2020. "4D surface seismic monitoring the evolution of a small CO2 plume during and after injection: CO2CRC Otway Project study." *Exploration Geophysics 51 (5), 570-580*.”

Authors	**Conception and design**	**Acquisition of data**	**Data processing**	**Data analysis**	**Paper writing**	**Paper review**
Sofya Popik		x	x	x	x	
I acknowledge that these represent my contribution to the above research output Signed:						
Roman Pevzner	x	x		x		x
I acknowledge that these represent my contribution to the above research output Signed:						
Konstantin Tertyshnikov	x	x				x
I acknowledge that these represent my contribution to the above research output Signed:						
Dmitry Popik		x	x			
I acknowledge that these represent my contribution to the above research output Signed:						
Milovan Urosevic	x	x				
I acknowledge that these represent my contribution to the above research output Signed:						
Valeriya Shulakova		x	x			
I acknowledge that these represent my contribution to the above research output Signed:						
Stanislav Glubokovskikh				x		
I acknowledge that these represent my contribution to the above research output Signed:						
Boris Gurevich	x					x
I acknowledge that these represent my contribution to the above research output Signed:						

2. Paper “Popik, S., R. Pevzner, A. Bona, K. Tertyshnikov, S. Glubokovskikh, and B. Gurevich. 2021. "Estimation of P-wave anisotropy parameters from 3D vertical seismic profile with distributed acoustic sensors and geophones for seismic imaging in the CO2CRC Otway Project." *Geophysical Prospecting 69 (4), 842-855*.”

Authors	Conception and design	Acquisition of data	Data processing	Data analysis	Paper writing	Paper review
Sofya Popik	x	x	x	x	x	
I acknowledge that these represent my contribution to the above research output Signed:						
Roman Pevzner	x	x		x		x
I acknowledge that these represent my contribution to the above research output Signed:						
Andrej Bona	x			x		x
I acknowledge that these represent my contribution to the above research output Signed:						
Konstantin Tertyshnikov		x				
I acknowledge that these represent my contribution to the above research output Signed:						
Stanislav Glubokovskikh				x		
I acknowledge that these represent my contribution to the above research output Signed:						
Boris Gurevich				x		x
I acknowledge that these represent my contribution to the above research output Signed:						

Appendix B: Copyright consent

This thesis utilises previously published material under the following papers:

1) Popik, S., R. Pevzner, K. Tertyshnikov, D. Popik, M. Urosevic, V. Shulakova, S. Glubokovskikh, and B. Gurevich. 2020. "4D surface seismic monitoring the evolution of a small CO2 plume during and after injection: CO2CRC Otway Project study." *Exploration Geophysics* 51 (5), 570-580.

2) Popik, S., R. Pevzner, A. Bona, K. Tertyshnikov, S. Glubokovskikh, and B. Gurevich. 2021. "Estimation of P-wave anisotropy parameters from 3D vertical seismic profile with distributed acoustic sensors and geophones for seismic imaging in the CO2CRC Otway Project." *Geophysical Prospecting* 69 (4), 842-855.

License Details

This Agreement between Curtin University -- Sofya Popik ("You") and John Wiley and Sons ("John Wiley and Sons") consists of your license details and the terms and conditions provided by John Wiley and Sons and Copyright Clearance Center.

Print Copy

License Number	5141211492499
License date	Sep 03, 2021
Licensed Content Publisher	John Wiley and Sons
Licensed Content Publication	Geophysical Prospecting
Licensed Content Title	Estimation of P-wave anisotropy parameters from 3D vertical seismic profile with distributed acoustic sensors and geophones for seismic imaging in the CO2CRC Otway Project
Licensed Content Author	Boris Gurevich, Stanislav Glubokovskikh, Konstantin Tertyshnikov, et al
Licensed Content Date	Apr 9, 2021
Licensed Content Volume	69
Licensed Content Issue	4
Licensed Content Pages	14
Type of Use	Dissertation/Thesis
Requestor type	Author of this Wiley article
Format	Print and electronic
Portion	Full article
Will you be translating?	No
Title	Integration of Borehole and Surface Seismic Monitoring Techniques in CO2 Geosequestration Projects
Institution name	Curtin University
Expected presentation date	Jan 2022
Order reference number	1008
Requestor Location	Curtin University ARRC/CSIRO Building, H Block, Level 4 26 Dick Perry Avenue Kensington Perth, WA 6151 Australia Attn: Curtin University
Publisher Tax ID	EU826007151
Total	**0.00 AUD**

This thesis utilises previously published material under the following conference abstracts:

1) Popik, S., R. Pevzner, and A. Bona. 2020. "P-Wave Anisotropy Estimation from 3D VSP Data Acquired with Geophones and DAS at Otway Site." 82nd EAGE Annual Conference & Exhibition, Amsterdam, The Netherlands.
2) Popik, S., R. Pevzner, A. Bona, K. Tertyshnikov, S. Glubokovskikh, and B. Gurevich. 2020. "P-wave Anisotropy Parameters Estimation from Multi-well 3D VSP using DAS: Stage 3 of the CO2CRC Otway Project." EAGE Workshop on Fiber Optic Sensing for Energy Applications in Asia Pacific.
3) Popik, S., D. Popik, and R. Pevzner. 2019. "Effect of Density of Seismic Sources on the Quality of the 4D Seismic Data." 81st EAGE Conference and Exhibition 2019, London, UK.

To this date (September 2021), as per the EAGE copyrights and use of the EAGE materials, authors have the following rights to use abstract materials:

“EAGE is the only party that is entitled to use the abstract until six (6) months after the event that the abstract was submitted for. After this period, you are free to use the original version (but not a version as amended and published by EAGE with the

lay-out and logo of EAGE or any images that may have been added) for other purposes."

For more details on EAGE policies and permissions, please refer to https://eage.org/media/copyrights-and-use-of-eage-materials/.

Appendix C: Detailed surface seismic data processing flow charts

"Express processing" approach

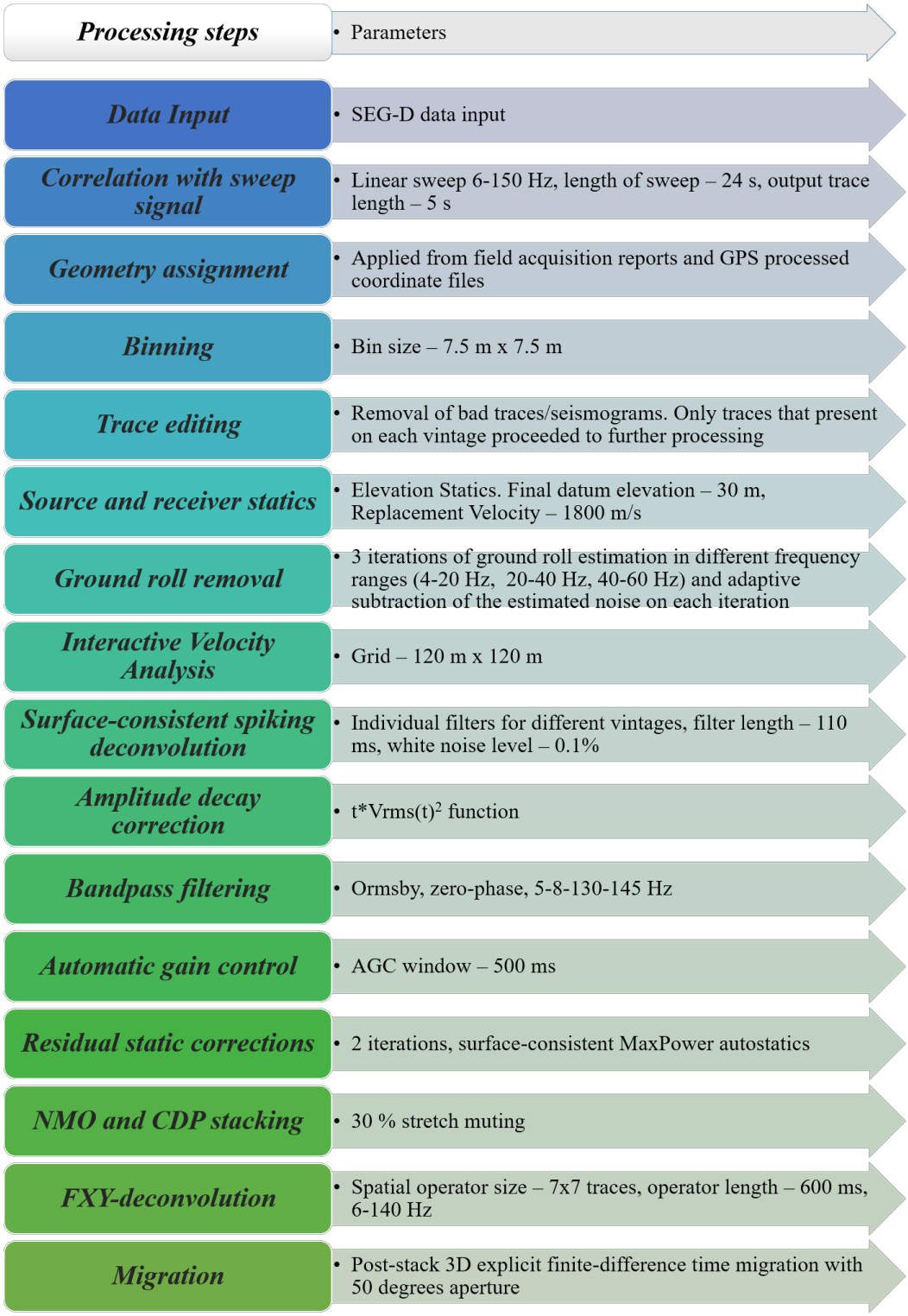

Pre-stack migration approach

Processing steps	• Parameters
Data Input	• SEG-D data input
Correlation with sweep signal	• Linear sweep 6-150 Hz, length of sweep – 24 s, output trace length – 5 s
Geometry assignment	• Applied from field acquisition reports and GPS processed coordinate files
Binning	• Bin size – 7.5 m x 7.5 m
Trace editing	• Removal of bad traces/seismograms. Only traces that present on each vintage proceeded to further processing
Source and receiver statics	• Elevation Statics. Final datum elevation – 30 m, Replacement Velocity – 1800 m/s
Ground roll removal	• 3 iterations of ground roll estimation in different frequency ranges (4-20 Hz, 20-40 Hz, 40-60 Hz) and adaptive subtraction of the estimated noise on each iteration
Interactive Velocity Analysis	• Grid – 120 m x 120 m
Surface-consistent spiking deconvolution	• Individual filters for different vintages, filter length – 110 ms, white noise level – 0.1%
Bandpass filtering	• Ormsby, zero-phase, 5-8-130-145 Hz
Residual static corrections	• 2 iterations, surface-consistent MaxPower autostatics
Migration	• Prestack Kirchhoff Time Migration (two-sided aperture of 1400 m at the target interval of 1200 ms)
Automatic gain control	• AGC window – 500 ms
FK-filtering	• Suppress dipping artefacts on migrated gathers (Fan filter: Spatial operator size – 15 traces; operator length – 600 ms)
CMP sorting and stacking	• Power for stack normalization – 0.5
FK-filtering	• Suppress dipping artefacts on stack (Fan filter: Spatial operator size – 30 traces; operator length – 300 ms)
FXY-deconvolution	• Spatial operator size – 7x7 traces, operator length – 600 ms, 6-140 Hz